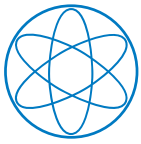

Technische Universität München
Universiteit Gent

The Influence of Radiation, Mechanical, and Plasma-Induced Damage on Deuterium Retention in Tungsten

Mikhail Zibrov

Vollständiger Abdruck der von der Fakultät für Physik der Technischen Universität München zur Erlangung der akademischen Grades eines

Doktors der Naturwissenschaften

genehmigten Dissertation.

Vorsitzende(r): Prof. Dr. Michael Knap

Prüfer der Dissertation:

1. Prof. Dr. Ulrich Stroth
2. Priv.-Doz. Dr. Christoph Hugenschmidt
3. Prof. Dr. Günther Dollinger
4. Prof. Dr. Jean-Marie Noterdaeme
5. Prof. Dr. Kim Verbeken
6. Prof. Dr. Paloma Fernández Sánchez

Die Dissertation wurde am 02.08.2018 bei der Technischen Universität München eingereicht und durch die Fakultät für Physik am 12.11.2018 angenommen.

Technische Universität München

UNIVERSITEIT GENT

Universiteit Gent

The Influence of Radiation, Mechanical, and Plasma-Induced Damage on Deuterium Retention in Tungsten

Mikhail Zibrov

The Influence of Radiation, Mechanical, and Plasma-Induced Damage on Deuterium Retention in Tungsten

Mikhail Zibrov

Promoters: Prof. Dr. U. Stroth, Prof. dr. ir. J.-M. Noterdaeme
Supervisors: Dr. M. Mayer, Dr. T.W. Morgan, Dr. Yu. Gasparyan
Doctoral thesis submitted in order to obtain the academic degrees of
Doktor der Naturwissenschaften (Technical University of Munich) and
Doctor of Engineering Physics (Ghent University)

Chair for Plasma Surface and Divertor Physics (E28)
Head: Prof. Dr. U. Stroth
Department of Physics
Technical University of Munich

Department of Applied Physics
Head: Prof. dr. ir. C. Leys
Faculty of Engineering and Architecture
Ghent University

Academic year 2018–2019

Contents

List of acronyms

at. fr.	Atomic fractions
bcc	Body-centred cubic
BSE	Backscattered electrons
CLSM	Confocal laser scanning microscopy
DBS	Positron annihilation Doppler broadening spectroscopy
DEMO	Demonstration fusion power plant
DFT	Density functional theory
dpa	Displacement per atom
EAM	Embedded-atom method
EDX	Energy-dispersive X-ray spectroscopy
ELM	Edge localized mode
fcc	Face-centred cubic
FWHM	Full width at half maximum
IR	Infrared
ITER	International thermonuclear experimental reactor
MS	Molecular statics
NRA	Nuclear reaction analysis
PAS	Positron annihilation spectroscopy
PALS	Positron annihilation lifetime spectroscopy
PFC	Plasma-facing component
PFM	Plasma-facing material
PKA	Primary knock-on atom
QMS	Quadrupole mass-spectrometer
SEM	Scanning electron microscopy
TDS	Thermal desorption spectroscopy
TEM	Transmission electron microscopy
UHV	Ultra-high vacuum

Abstract

The hydrogen isotope inventory in tungsten is governed by the presence of lattice defects acting as trapping sites. Apart from the defects introduced during manufacturing (dislocations, grain boundaries, impurities, etc.), in fusion reactors with a burning deuterium–tritium plasma, bombardment with 14 MeV neutrons will create a high concentration of radiation defects (vacancies, vacancy clusters, dislocation loops, etc.) through the entire thickness of the tungsten armour. This will significantly increase the trap density for hydrogen isotopes. Furthermore, high incident fluxes of hydrogen isotopes can induce the formation of subsurface defects (blister-like structures) in tungsten. Although the general trends have been elucidated previously, there is still a lack of understanding how each defect type contributes to the total hydrogen retention. This thesis aims to shed light on this issue by examining samples having one dominant and well-characterized defect type.

The role of plasma-induced defects was studied by exposing polycrystalline tungsten to divertor-relevant fluxes (3–5$\times 10^{23}$ D/m^{2}s) of low-energy (40 eV/D) deuterium ions to very high fluences of up to 1.2×10^{28} D/m^2. Deuterium retention in the samples was examined using nuclear reaction analysis (NRA) and thermal desorption spectroscopy (TDS); surface modifications were studied using scanning electron microscopy (SEM). Plasma exposure at 380 K lead to a massive formation of surface modifications appearing either as dome-shaped blisters or stepped, flat-topped, and irregularly shaped protrusions. Their average size and density barely changed with fluence. Underneath these structures cavities were found, which were formed only by intergranular cracks in the case of blisters and both by inter- and transgranular cracks in the case of protrusions. The deuterium depth distributions and total deuterium inventories also exhibited only weak fluence dependence. The majority of deuterium was trapped in a subsurface region with enhanced deuterium concentration (a few times 10^{-3} at. fr.); its thickness coincided with the depth up to where the cracks corresponding to blisters and protrusions were located. It can be concluded that blisters and protrusions introduce additional trapping sites for deuterium with concentrations higher than the concentration of intrinsic defects in the material. Therefore, the trapping in these defects governs the deuterium retention in the investigated fluence range and their features depend on the ion flux.

To prepare samples containing mainly vacancies, recrystallized tungsten was irradiated by 10 keV deuterium ions to a low damage level of 7.8×10^{-3} dpa. All experimental steps were carried out *in situ* without exposing the sample to air allowing to minimise the presence of impurities on the surface that can cause reduction of the deuterium recombination rate. Using a procedure comprising post-damaging annealing of the sample at 550 K and subsequent low-energy and low-flux deuterium implantation allowed to obtain a TDS spectrum with a prominent peak corresponding to deuterium release from vacancies. This experimental sequence was repeated several times with different TDS heating rates in the range of 0.15–4 K/s. The sum of the deuterium binding energy with vacancies and the activation energy for deuterium diffusion in tungsten of $E_b + E_D = 1.56 \pm 0.06$ eV was determined from the slope of the Arrhenius-like plot $\ln\left(\beta/T_m^2\right)$ versus $1/T_m$, where β is the heating rate and T_m is the position of the TDS peak corresponding to vacancies. This method allowed to determine $E_b + E_D$ with high accuracy and without the need to know the material and trap parameters, which is not possible by the commonly used method based on fitting of simulated TDS spectra to experimental ones.

To investigate the thermal evolution of vacancies, tungsten single crystals were irradiated by 200 keV protons to a low damage level (5.8×10^{-3} dpa) and then annealed at temperatures in the range of 500–1800 K. The resulting defects were characterized by positron annihilation lifetime spectroscopy (PALS). The formation of clusters containing on average 13 vacancies driven by the onset of vacancy mobility was detected after annealing at 700 K. Annealing at 800 K and higher temperatures resulted in the formation of large clusters containing more than 30 vacancies and almost no changes in the defect structure were visible up to an annealing temperature of 1200 K. Annealing at 1300 K and higher temperatures resulted in the decrease of the defect concentration leading to the eventual removal of all introduced defects at 1800 K. This was likely accompanied by further coarsening of vacancy clusters. It was observed that the determined sizes of the clusters were larger than those expected from thermal stability considerations based on calculated values of vacancy binding energies to clusters. The coarsening of clusters, therefore, probably occurred via coalescence of small clusters. The concentration of deuterium trapped in these defects after exposure to a low–flux (10^{20} D/m^{2}s) deuterium plasma at 450 K decreased with increasing annealing temperature mostly following the changes in the defect concentration detected by PALS.

While the full recovery of radiation defects at a low damage level was observed after annealing at 1800 K, increasing the damage level (i.e., the defect concentration) results in a shift of the recovery temperature to higher values. Annealing at 1800 K of a sample damaged to 1.1 dpa by self-ions resulted in the formation of voids that can store D_2 gas with a binding energy close to that for deuterium in vacancies. Damaging by protons was also shown to promote the formation of protrusions under deuterium plasma exposure, in contrast to damaging by self-ions.

To prepare samples dominated by dislocations, tensile deformations of recrystallized tungsten at temperatures of 573 K and 873 K to strains in the range of 3–38 % were carried out. The dislocation density in the grain interior measured by transmission electron microscopy (TEM) increased by more than one order of magnitude after deformation to the highest strain. The deuterium concentrations after the low-flux plasma exposures both at 370 K and 450 K were low (up to a few times 10^{-4} at. fr.) and increased more slowly with strain than the dislocation density. The presence of vacancy- and vacancy cluster-type defects was detected both by PALS and TDS with concentrations increasing more weakly with strain than the dislocation density. These defects were attributed to by-products of the deformation: jogs on dislocations and/or deformation-induced vacancies and vacancy clusters. It can be concluded that the dislocations themselves have only a small binding energy for deuterium and are practically not able to trap it already at 370 K. It was also observed that deformation already to the lowest strains significantly facilitates the formation of blisters and protrusions under deuterium plasma exposure. Based on TEM observations, this was attributed mainly to the formation of dislocation pile-ups near grain boundaries which can act as nucleation sites for blisters and protrusions.

Zusammenfassung

Die Rückhaltung von Wasserstoffisotopen in Wolfram wird durch das Vorhandensein von Kristallgitterdefekten, welche als Bindungsstellen für Wasserstoff fungieren, bestimmt. Abgesehen von bei der Herstellung entstandenen Defekten (Versetzungen, Korngrenzen, Verunreinigungen, etc.) wird es in einem Kernfusionsreaktor, in welchem ein Deuterium-Tritium-Plasma brennt, durch die entstehenden 14-MeV-Neutronen zu einer hohen Konzentration an Strahlenschäden (Leerstellen, Leerstellencluster, Versetzungsringe, etc.) über die gesamte Dicke der Wolframauskleidung kommen. Dies wird die Dichte an potenziellen Bindungsstellen für Wasserstoffisotope signifikant erhöhen. Des weiteren können hohe Teilchenflüsse zur oberflächennahen Defektbildung (Blister) in Wolfram führen. Obwohl diese Prozesse bereits im Groben bekannt sind, existiert weiterhin ein Mangel an Verständnis darüber, wie die einzelnen Defektarten jeweils zum gesamten Wasserstoffrückhalt beitragen. Diese Dissertation zielt daher darauf ab, diese Fragestellung durch die Untersuchung von Proben mit jeweils nur einer dominierenden und gut charakterisierten Defektart zu untersuchen.

Die Rolle plasmainduzierter Defekte wurde untersucht indem polykristallines Wolfram divertor-relevanten Flüssen ($3–5\times10^{23}$ D/m^{2}s) von niederenergetischen (40 eV/D) Deuteriumionen bei Fluenzen von bis zu 1.2×10^{28} D/m^2 ausgesetzt wurde. Die Deuteriumrückhaltung in den Proben wurde durch Kernreaktionsanalyse (NRA) sowie thermische Desorptionsspektroskopie (TDS) untersucht; Oberflächenveränderungen wurden mit Hilfe der Rasterelektronenmikroskopie (SEM) dokumentiert. Plasmaexpositionen bei 380 K führten zu erheblichen Oberflächenveränderungen in Form von kuppelförmigen Blistern oder gestuften, oben abgeflachten und irregulär geformten Erhebungen, deren durchschnittliche Größe und Dichte sich mit erhöhter Fluenz kaum veränderte. Unter diesen Strukturen wurden Hohlräume gefunden, welche im Falle der Blister durch Risse entlang von Korngrenzen, sowie im Falle der Erhebungen durch Risse entlang von Korngrenzen oder Risse innerhalb von Körnern, verursacht wurden. Die Tiefenverteilung des Deuteriums sowie die Gesamtmenge zeigten ebenfalls nur eine schwache Fluenzabhängigkeit. Der Großteil des Deuteriums wurde in einer Region nahe der Oberfläche zurückgehalten welche eine erhöhte Deuteriumkonzentration (in der Größenordnung von 10^{-3} at. fr.) zeigte; ihre

Dicke stimmte mit der Tiefe überein in welcher sich die Hohlräume der Blister fanden. Hieraus kann geschlossen werden, dass Blister und Erhebungen zu zusätzlichen Einfangstellen, an denen sich Deuterium anlagern kann, führen. Die Konzentration dieser Einfangstellen kann die intrinsische Defektkonzentration deutlich übersteigen. Daher dominiert der Einfang an diesen Defekten den Deuteriumrückhalt in den untersuchten Fluenzbereichen. Desweiteren bestimmt der Ionenfluss die Eigenschaften der Oberflächenveränderungen.

Um vorwiegend Leerstellen enthaltende Proben zu erzeugen wurde rekristallisiertes Wolfram mit 10 keV Deuteriumionen bis zu einem niedrigen Schadensniveau von 7.8×10^{-3} dpa geschädigt. Alle Schritte des Experiments wurden *in situ*, ohne die Probe an Luft zu exponieren, ausgeführt um die Verunreinigungskonzentration an der Oberfläche zu minimieren, welche zu einer Reduzierung der Deuteriumsrekombinationsrate führen kann. Es wurde ein Prozedere verwendet, bei dem zuerst post-schädigungs Annealing bei 550 K und dann eine Niederenergie-, Niederflussdeuteriumbeladung durchgeführt wird. Dies erlaubt es, ein TDS-Spektrum zu erhalten, in dem der den Leerstellen zugeordnete Desorptionspeak gut sichtbar ist. Dieses Prozedere wurde mehrmals mit variierten TDS Heizraten (0.15–4 K/s) durchgeführt. Die Summe der Bindungsenergie von Deuterium mit Leerstellen und der Aktivierungsenergie für Deuteriumdiffusion in Wolfram $E_b + E_D = 1.56 \pm 0.06$ eV wurde aus der Steigung des Arrhenius-plots, $\ln\left(\beta/T_m^2\right)$ versus $1/T_m$ (hier bezeichnet β die Heizrate und T_m die Position des auf Leerstellen zurückzuführenden TDS Peaks), bestimmt. Diese Methode erlaubt es $E_b + E_D$ mit großer Genauigkeit zu bestimmen ohne die Parameter des Materials oder der Leerstelle kennen zu müssen. Dies wäre mit der üblicherweise verwendeten Methode, bei der simulierte TDS-Spektren an experimentelle gefittet werden, nicht möglich gewesen.

Um die thermische Evolution von Leerstellen zu untersuchen, wurden Wolframeinkristalle mit 200 keV Protonen bis zu einem noch niedrigen Schadensniveau von 5.8×10^{-3} dpa geschädigt und dann bei Temperaturen von 500 K bis 1800 K geheizt. Die dabei entstandenen Defekte wurden durch Positronenlebendsdauerspektroskopie (PALS) charakterisiert. Die Bildung von Clustern, die im Schnitt 13 Leerstellen enthalten, wurde nach dem Tempern bei 700 K festgestellt. Dies wird mit dem Schwellwert der Leerstellenmobilität gleichgesetzt. Bei Temperaturen von über 800 K und höher bildeten sich aus mehr als 30 Leerstellen bestehende Cluster. Bis 1200 K war fast keine Veränderung in der Defektstruktur sichtbar. Eine Verringerung der Defektkonzentration begann ab 1300 K und endete bei 1800 K mit dem gänzlichen Ausheilen der Defekte. Sie ging wahrscheinlich mit einem weiteren Wachstum der Cluster einher. Die gemessenen Clustergrößen waren größer als vom Gesichtspunkt der, unter Verwendung der Cluster-Leerstellen Bindungsenergie berechneten, thermischen Stabilität aus erwartet worden wäre. Das Clusterwachstum wurde daher vermutlich durch das Verschmelzen von kleinen Clustern getrieben. Die Konzentration von in diesen Defekten gefangenem Deuterium sank mit steigender Temperatur nach einer Exposition in einem Niedrigfluss (10^{20} D/m^{2}s)

Deuteriumplasma bei 450 K. Dies erfolgte ungefähr proportional zur mit PALS bestimmten Veränderung der Defektkonzentration.

Während für ein niedriges Schädigungsniveau das vollständige Ausheilen der Strahlenschäden nach dem Annealen bei 1800 K beobachtet wurde, war bei höheren Schädigungsniveaus (und entsprechend höheren Defektkonzentrationen) eine Verschiebung hin zu höheren Temperaturen zu beobachten. Das Tempern einer mit bis auf 1.1 dpa mit Eigenionen geschädigten Probe führte zur Bildung von Hohlräumen, in welchen D_2-Gas mit einer Bindungsenergie ähnlich der von Deuterium in Leerstellen eingelagert werden kann. Des weiteren zeigte sich, dass das Schädigen mit Protonen auch die Bildung von Erhebungen während der Exposition mit Deuteriumplasma verstärkt. Dies ist gegensätzlich zu den Beobachtungen an mit Eigenionen geschädigten Proben.

Um hauptsächlich Versetzungen enthaltende Proben herzustellen, wurden Zugverformungen an rekristallisiertem Wolfram bei Temperaturen von 573 K und 873 K und Dehnungen von 3–38 % durchgeführt. Die durch Transmissionselektronenmikroskopie (TEM) bestimmte Versetzungsdichte im Korninneren stieg um mehr als eine Größenordnung bei der stärksten durchgeführten Dehnung. Die nach Niederfluss-Plasmaexpositionen bei 370 K bzw. 450 K bestimmte Deuteriumkonzentration für beide Implantationstemperaturen war niedrig (weniger als einige 10^{-4} at. fr.). Sie stieg langsamer im Vergleich zur Dehnung als zur Versetzungsdichte. Die Präsenz von leerstellenartigen Defekten wurde sowohl durch PALS als auch TDS festgestellt. Im Vergleich zur Versetzungsdichte stieg diese schwächer mit zunehmender Dehnung. Die folgenden Defekte wurden Beiprodukten der Deformation zugerechnet: Versetzungssprünge und/oder deformationsinduzierte Leerstellen und Leerstellencluster. Es wird vermutet, dass die Versetzungen selbst nur eine kleine Deuteriumsbindungsenergie besitzen und praktisch schon ab 370 K nicht mehr in der Lage sind Deuterium zu halten. Des weiteren wurde beobachtet, dass schon bei der geringsten angewendeten Dehnung die Bildung von Blistern und Erhebungen bei der Exposition mit einem Deuteriumplasma signifikant erhöht ist. Basierend auf TEM Beobachtungen, wurde dies hauptsächlich der Bildung von Versetzungshäufungen nahe der Korngrenzen zugerechnet, da diese Keime für Blister und Erhebungen sein können.

Samenvatting

De waterstofretentie in wolfraam wordt vooral bepaald door onregelmatigheden in het kristalrooster die als opslagplek fungeren. Naast de defecten die tijdens de productie worden geïntroduceerd (dislocaties, korrelgrenzen, onzuiverheden, etc.), zorgt de intense bestraling met 14 MeV neutronen die vrijkomen bij fusie in een deuterium-tritium plasma voor extra defecten over de gehele dikte van de wolfraam reactorwand (vacatures, vacatureclusters, dislocatie ophopingen, etc.). Deze extra defecten vergroten de waterstofretentie van wolfraam. Verder kunnen hoge waterstoffluxen zorgen voor defecten vlak onder de oppervlakte met een blaarvormige structuur. Hoewel de algemene trends opgehelderd zijn, is er een gebrek aan begrip over hoe individuele defecttypen aan de waterstofretentie bijdragen. Deze thesis probeert hieraan toe te voegen door samples te analyseren met één overheersend, goed gekarakteriseerd defecttype.

De rol van plasma-geinduceerde defecten was onderzocht door polykristallijne samples aan divertor relevante fluxen (3–5$\times 10^{23}$ D/m^{2}s) van lage-energie (40 eV/D) deuterium ionen bloot te stellen met zeer hoge fluenties tot 1.2×10^{28} D/m^2. De deuteriumretentie in de samples werd bestudeerd met kernreactieanalyse (NRA) en thermische desorptie spektrometrie (TDS); oppervlaktemodificaties werden bestudeerd met een rasterelektronenmikroskopie (SEM). Plasmablootstelling bij 380 K zorgde voor een massale vorming van oppervlaktemodificaties die er ofwel uitzagen als koepelvormige blaren ofwel als trapsgewijze, met plateau, onregelmatig gevormde uitsteeksels. De gemiddelde grootte en dichtheid veranderen bijna niet met de fluentie. Onder deze stuctuuren werden holtes gevonden, die werden gevormd door intergranulaire breuken in het geval van blaren, en inter- en transgranulaire breuken in het geval van uitsteeksels. De diepteverdeling en totale hoeveelheid deuteriumretentie hangen ook vrijwel niet af van de fluentie. De meerderheid van het deuterium was opgeslagen in zones onder de oppervlakte met een verhoogde deuteriumconcentratie (een paar maal 10^{-3} at. fr.); de hoogte van deze zones komt overeen met het gebied waar de holtes van de blaarstructuren zich bevinden. Blaren en uitsteeksels zorgen voor additionele opslagplekken voor deuterium, met een hogere concentratie dan de intrinsieke defecten in het materiaal. Hierdoor wordt de deuteriumretentie bepaald door de extrinsieke defecten, de morfologische eigenschappen hangen af van de ionenflux.

Om samples te maken met voornamelijk vacatures, werd gerekristalliseerd wolfraam beschadigd met 10 keV deuterium ionen tot een laag beschadigingsniveau van 7.8×10^{-3} dpa. Alle experimentele stappen werden *in situ* uitgevoerd, zonder het sample bloot te stellen aan de atmosfeer, om zo de concentratie aan onzuiverheden aan de oppervlakte te minimaliseren, die ervoor kunnen zorgen dat de deuterium recombinatiesnelheid vertraagt. Een TDS spectrum met een prominente piek ten gevolge van deuterium afgifte werd gemeten na een temperatuurbehandeling van 550 K met daaropvolgend lage energie en lage flux implantatie. Deze experimentele procedure werd een aantal keren herhaald met verschillende TDS verhittingssnelheden (0.15–4 K/s). De som van de deuterium bindingsenergie met vacatures en de activeringsenergie voor deuterium diffusie in wolfraam van $E_b + E_D = 1.56 \pm 0.06$ eV werd bepaald uit de helling van een Arrhenius plot $\ln\left(\beta/T_m^2\right)$ tegen $1/T_m$, met β de verhittingssnelheid en T_m de positie van de TDS piek van de vacatures. Met deze methode is $E_b + E_D$ nauwkeurig te bepalen zonder de materiaal- en defectparameters te weten, wat niet mogelijk is met de algemeen gebruikte methode waarbij experimentele TDS spectra met gesimuleerde spectra gefit worden.

Om het gedrag van de vacatures bij verschillende temperaturen te bepalen werden wolfraamkristallen beschadigd met 200 keV protonen tot een laag beschadigingsniveau van 5.8×10^{-3} dpa, en vervolgens verhit tot temperaturen in de range 500–1800 K. De resulterende defecten werden gekarakteriseerd met positron annihilatie levensduur spectroscopie (PALS). De formatie van clusters met gemiddeld 13 vacatures, ten gevolge van mobiliteit van vacatures, werd gedetecteerd na een warmtebehandeling bij 700 K. Een warmtebehandeling bij 800 K en hogere temperaturen resulteerde in de formatie van grote clusters van meer dan 30 vacatures, bijna zonder verandering in de defectstructuur tot een temperatuur van 1200 K. Warmtebehandeling bij 1300 K en hoger leidde tot een afname van de defectconcentratie, vanaf 1800 K zijn alle geïntroduceerde defecten weg. Dit ging waarschijnlijk hand in hand met een verruwing van de vacatureclusters. De gemeten clustergroottes waren meer dan verwacht op basis van energetische afschattingen. De clusters groeien waarschijnlijk door de samensmelting van kleine clusters. De deuteriumconcentratie in deze defecten na een lage-flux (10^{20} D/m^{2}s) blootstelling aan een deuteriumplasma bij 450 K nam af met een toenemenende temperatuur tijdens de nabehandeling. De afnemende deuteriumretentie correspondeert met de defectconcentratie gemeten met PALS.

Volledig herstel van een laag stralingsschadeniveau werd gemeten bij warmtebehandeling van 1800 K, een verhoging van het schadeniveau (d.i. de defectconcentratie) zorgt voor een stijging van de hersteltemperatuur. Een wolfraam sample dat tot 1.1 dpa beschadigd is door middel van wolfraamionen kan na een temperatuurbehandeling bij 1800 K D_2 holtes vormen en daarmee gas opslaan met een bindingsenergie die vrijwel gelijk is aan de bindingsenergie van deuterium in vacatures. Beschadiging met protonen zorgt voor de versterkte

formatie van uitsteeksels na deuterium plasma blootstelling, in tegenstelling tot beschadiging met wolfraam ionen.

Om samples met dislocaties te maken, werden trekdeformaties van gerekristalliseerd wolfraam bij temperaturen van 573 K en 873 K uitgevoerd, tot vervormingen in de range van 3–38 %. De dislocatie dichtheid in de kristallieten gemeten met transmissie-electronenmikroskopie (TEM) nam toe met meer dan een ordegrootte na deformatie bij de grootste vervorming. De deuteriumconcentraties na een lage-flux plasmablootstelling bij 370 K en 450 K waren laag (tot een paar keer 10^{-4} at. fr.), en namen langzamer toe met de vervorming dan met de dislocatiedichtheid. De aanwezigheid van vacature- en vacaturecluster-type defecten werd gemeten met PALS en TDS en hadden een concentratie die ook langzamer toenam met de vervorming dan met de dislocatiedichtheid. Deze defecten werden toegeschreven aan bijproducten van de deformatie: bewegingen van dislocations en/of deformatie-geïnduceerde vacatures en vacatureclusters. Er kan worden geconcludeerd dat de dislocaties zelf een kleine bindingsenergie voor deuterium hebben, en al bij 370 K bijna niet in staat zijn om deuterium vast te houden. Zelfs deformatie bij de laagste vervormingsniveaus zorgt voor een toegenomen vorming van blaarstructuren en uitsteeksels onder waterstofplasma blootstelling. Gebaseerd op TEM metingen, werd dit voornamelijk toegeschreven aan de vorming van dislocatie verzamelingen bij korrelgrenzen die als nucleatiekern kunnen fungeren voor blaarstructuren en uitsteeksels.

Chapter 1

Introduction

The fusion of deuterium and tritium nuclei into helium is a promising next-generation source of electricity. The temperatures and densities necessary for a "burning" fusion plasma have already been achieved in present-day magnetic confinement devices. In the world's largest tokamak JET the maximum reached fusion power was around 64 % of the heating power required to sustain the plasma temperature [1]. The international experimental fusion reactor ITER currently being built in the south of France should demonstrate a significant net power production (ten times more fusion power output than the heating power input) in long-pulse operation (400 s). Its successor device, the demonstration fusion power plant (DEMO), and, eventually, future fusion power plants will have to operate with a very long pulse duration (> 2 h) or even with a steady-state burning plasma [2]. Besides many challenges from the plasma physics side, one of the key engineering issues towards the realization of a fusion power plant is the selection of proper plasma-facing and structural materials able to withstand the severe reactor conditions. Since the early fusion experiments, it was recognized that the processes of interaction of the edge plasma with plasma-facing components (PFCs) strongly influences the performance of future fusion reactors [3]. Erosion of PFCs determines their lifetime and the presence of impurities in the core plasma, which cool and dilute it. Deposition of eroded material onto PFCs changes their surface composition, can result in substantial tritium inventory in such layers, and delamination of these layers leads to the formation of dust. Retention and recycling of hydrogen isotopes in PFCs is an issue from the safety and economic points of view (the in-vessel tritium inventory is restricted), influences thermo-mechanical properties of PFCs, and also determines the fuel balance in the reactor and the plasma density control. Another safety issue is the permeation of hydrogen isotopes through PFCs into the cooling system.

The PFCs are subjected to extremely high particle and heat fluxes, which they must withstand over years of operation. In ITER the PFCs will receive high

fluxes (10^{19}–10^{24} particles/m^{2}s) of hydrogen isotopes and impurities (helium, nitrogen, etc.) with energies ranging from several eV to several keV [4–6]. This will result in high steady-state heat loads of up to 10 MW/m^2 near the strike point in the divertor, combined with high transient loads during edge localized modes (ELMs)[1] (a few GW/m^2 for 0.5–1 ms, repetition rates of more than 1 Hz) and even higher ones during off-normal events (unmitigated disruptions and vertical displacement events).

Finally, in fusion reactors with a burning deuterium-tritium plasma, the PFCs and structural components will be subjected to high fluxes of 14 MeV neutrons created by the fusion reactions. These neutrons will introduce radiation defects through their whole thickness and cause material transmutation, resulting in their activation and bulk production of both hydrogen and helium [5, 7]. This will alter the thermo-mechanical properties of the materials (degradation of thermal conductivity, embrittlement, swelling, and irradiation creep), which the PFCs must tolerate without losing their integrity. In addition, radiation defects serve as trapping sites for hydrogen isotopes, thus, their presence can increase the tritium inventory in the materials by orders of magnitude.

Due to its high melting temperature, high sputtering threshold, high thermal conductivity, and relatively low long-term activation after neutron irradiation, tungsten is nowadays considered as the most promising plasma-facing material (PFM). In ITER the divertor will have a full-tungsten armour [6, 8]. In DEMO it is also planned to have tungsten PFCs in the divertor and, in addition, a thin armour layer of tungsten is foreseen on the first wall made of EUROFER steel [2]. Tungsten has been used as a material in several tokamaks (PLT, ORMAK, Doublet II) already in the 1970s, but their performances were limited by high levels of central radiation losses due to the presence of high-Z tungsten in the core plasma [3]. Because of that many fusion machines switched to low-Z carbon-based PFCs. However, carbon cannot be used in a fusion power plant due to its unacceptably high erosion and the strong degradation of its thermo-mechanical properties under neutron irradiation. Moreover, eroded carbon co-deposits with hydrogen isotopes forming hydrocarbon layers which can store significant amounts of tritium. Consequently, tungsten-based PFCs seem to be the only feasible solution at the moment[2].

Several techniques have been already developed in order to reduce tungsten erosion and its transport into the core plasma [9]. The introduction of the divertor and its detached (or partially detached) regimes allows to reduce the electron temperature in the divertor to a few eV, thus, no sputtering of tungsten in the divertor will take place in the inter-ELM phase[3]. In addition, even if sputtering takes place, the gyro-radius of a tungsten atom in the tokamak

1. ELMs are magnetohydrodynamic edge instabilities involving rapid periodic releases of energy and particles from the pedestal region into the scrape-off-layer.
2. The liquid metal (e.g., lithium, tin) PFC concepts, which have some advantages over tungsten PFCs, are still in a very early stage of development.
3. Hydrogen and impurity ions carried by the ELM filaments have sufficiently high energies to cause tungsten sputtering.

magnetic field can be larger than the ionisation length in the high-density edge plasma, which can lead to deposition of the sputtered atom directly after its erosion ("prompt redeposition"). Moreover, central wave heating and "flushing" the pedestal region by frequent ELMs have shown to reduce tungsten transport into the core plasma.

The possibility of a successful operation of a tokamak with a full-tungsten wall was first demonstrated at ASDEX Upgrade in 2007. With the transition of ASDEX Upgrade from a full-carbon to a full-tungsten wall, a reduction of the long-term deuterium retention by more than a factor of five was observed [10]. In addition, performance and confinement similar to operation with carbon PFCs in high-power discharges was demonstrated. In the JET tokamak, a strong decrease of the material erosion and the long-term deuterium retention (factor 10–20) was observed after installation of the ITER-like wall (beryllium first wall and tungsten divertor) with respect to the full-carbon wall [11].

Although significant progress in studying tungsten as a PFM has been achieved in the last decade [5–7], there still exist many open questions. In particular, the influence of radiation damage caused by neutrons on hydrogen isotope retention in tungsten is currently drawing a large attention from the fusion community. Although in ITER the maximum radiation damage level for the tungsten divertor is expected to be only 0.54 dpa by the end of its operation [12], already in DEMO the damage level of about 3 dpa for the tungsten divertor and up to 14.5 dpa for the first wall after one full power year of operation are expected [2, 13]. Even though the general features of hydrogen isotope accumulation in radiation-damaged tungsten have been elucidated, there is still a lack of fundamental understanding of how each type of radiation defects (vacancies, vacancy clusters, dislocation loops, etc.) contributes to the total hydrogen retention and its temperature dependence.

The influence of intrinsic lattice defects on retention is also not fully clarified, in particular, the role of dislocations. Large amounts of dislocations are introduced in tungsten already during the manufacturing process [14]. Furthermore, dislocations can also be formed in tungsten PFCs during transient events (e.g., ELMs) via a plastic deformation caused by high thermal stresses induced by the respective heat loads [5, 8]. Stresses caused by high local concentrations of interstitial hydrogen during a plasma operation can also induce a plastic deformation [15, 16].

Furthermore, it is known that hydrogen retention in non-damaged tungsten is intimately linked with the presence of sub-surface defects (blister-like structures) introduced during a plasma exposure, their number and features depend on particle flux, fluence, and sample temperature [17–19]. The majority of existing experiments were carried out at relatively low particle fluxes (up to 10^{22} particles/m^{2}s) and fluences (below 10^{27} particles/m^2) [20, 21]. Fluences in excess of 10^{30} particles/m^2 will be reached by the end of ITER operation [6] and in DEMO the expected fluences are even higher due to long-pulse (or steady-state) operation for several years.

The aim of the present work is to clarify the role of radiation-induced vacancies and vacancy clusters and of deformation-induced dislocations for deuterium retention in tungsten. To minimise possible ambiguities in interpretations, specially-prepared samples having one dominant and well-defined defect type were investigated. In addition, the impact of defects created by tungsten exposure to divertor-relevant high fluxes of low-energy deuterium ions to very high fluences up to 10^{28} D/m^2 was also examined. A more detailed description of this thesis' objectives and the techniques used can be found in section 3.7.

Chapter 2

Hydrogen in metals

Hydrogen interaction with metals draws attention from scientists for nearly two centuries dating back to 1823 when Döbereiner exposed a platinum sponge to hydrogen in the presence of air, which led to heating up of platinum resulting in the ignition of a hydrogen-air mixture. Such catalytic reactions on metals in the presence of hydrogen are still being actively studied. In the second half of the 19th century the phenomena of hydrogen permeation and accumulation in platinum and palladium were discovered, which was later implemented in palladium filters able to obtain extremely pure hydrogen. At that time the embrittlement of iron and steels due to hydrogen uptake (either from the gas phase or from an electrolyte) was also discovered, which is still being actively investigated. The development of nuclear fusion reactors with magnetic confinement stimulated investigations of the interaction of hydrogen ions and plasmas with metallic PFCs, which allowed discovering some new phenomena, e.g., the formation of blister-like structures, which were not observed in experiments with gaseous or atomic hydrogen. The search for efficient hydrogen storage materials stimulated fundamental studies aiming to reveal the elementary processes involved in hydrogen uptake and release in these materials.

This chapter gives a general overview of the physical mechanisms involved in the interaction of hydrogen (both gas and fast ions/atoms) with metals. First, the basic mechanisms of hydrogen uptake, release, and transport in metals are described. Then the main features of hydrogen interaction with defects in metals are reviewed. Afterwards, the diffusion-trapping model used for the description of these phenomena is presented. Finally, the methods of determination of hydrogen binding energies with defects from thermal desorption measurements are discussed.

2.1 Hydrogen uptake and transport in metals

2.1.1 Surface processes

The potential energy diagram for hydrogen[1] molecules and atoms near the surface of a metal, which was first proposed by Lennard-Jones [22], is shown schematically in Fig. 2.1. The potential energy of two atoms in a H_2 molecule is defined to be zero at infinity, therefore, the potential energy of two isolated atoms is equal to the dissociation energy of the H_2 molecule (4.5 eV). Both molecules and atoms have minima of the potential energy at some distances from the surface corresponding to adsorption sites. The adsorption of molecular hydrogen is usually referred to as physisorption, whereas the adsorption of atomic hydrogen as chemisorption [23]. The minimum of the potential energy for the atom Q_c (named as the heat of chemisorption) is much deeper than that for the molecule Q_p (called the heat of physisorption), and the adsorbed atom is much closer to the surface than the molecule due to chemical interaction. The two potential energy curves cross at the point of dissociation of the molecule, and after the dissociation, two atoms chemisorb individually. The energy required for the dissociation of a H_2 molecule near the surface is referred to as the activation energy for chemisorption E_c and is usually much lower than the energy required for the dissociation of a H_2 molecule in vacuum.

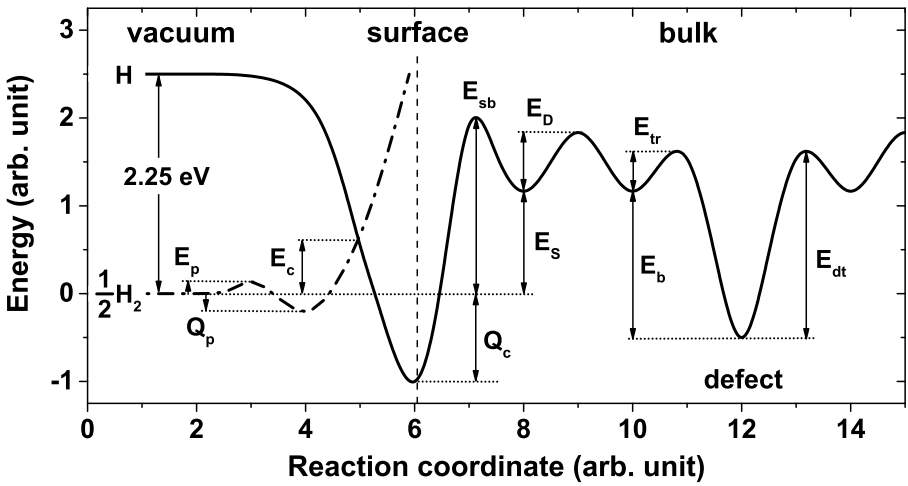

Fig. 2.1: Potential energy diagram for atomic and molecular hydrogen at the surface of a metal and in its bulk, where E_p and E_c are the activation energies for physisorption and chemisorption, respectively, Q_p and Q_c are the heats of physisorption and chemisorption, respectively, E_S is the heat of solution, E_D is the activation energy for diffusion, E_{sb} is the activation energy for absorption, E_{dt} is the detrapping energy, E_b is the binding energy, and E_{tr} is the activation energy for trapping.

1. From now and later on, by using a term "hydrogen" I mean any of its isotopes (protium (H), deuterium (D), tritium (T)) unless otherwise stated.

The penetration of chemisorbed hydrogen into the metal, which is called absorption, requires the additional energy E_{sb}. Hydrogen atoms absorbed in the metal can also go all the way back: enter the chemisorbed state from the absorbed state, recombine into a H_2 molecule, which will be physisorbed at the surface and finally desorbed back into the gas phase.

The kinetic description of the elementary processes of hydrogen adsorption, absorption, molecular dissociation, and recombination was proposed by several authors. A critical review of the existing models by Pisarev and Ogorodnikova [24] showed that the only self-consistent model is that proposed by Pick and Sonnenberg [25]. According to this model, by assuming a local equilibrium between the absorbed hydrogen in the subsurface layer (i.e., the first few atomic layers near the surface) and the chemisorbed hydrogen, and also assuming a low hydrogen surface coverage, the desorption flux J [atoms/(m^{2}s)] of hydrogen atoms in the form of H_2 molecules from the surface can be expressed as:

$$J = 2K_r C^2, \tag{2.1}$$

where C [atoms/m^3] is the subsurface concentration of absorbed hydrogen and K_r [m^4/s] is an effective recombination rate coefficient expressed as:

$$K_r = \frac{s_0}{\sqrt{2\pi m k_B T}} \frac{1}{S_0^2} \exp\left(\frac{2(E_S - E_c)}{k_B T}\right), \tag{2.2}$$

where s_0 is the hydrogen sticking coefficient at low surface coverage for a clean surface, m is the mass of a H_2 molecule, S_0 is the pre-exponential factor in the Sieverts' law (Eq. 2.3), T is the absolute temperature (both metal and gas are in equilibrium and have the same temperature), and k_B is the Boltzmann constant. For clean transition metal surfaces E_c is close to zero and s_0 is close to unity. The presence of various impurities on the surface (e.g., oxygen, carbon) results in the increase of E_c and respective decrease of the effective recombination rate coefficient[2].

In these models, thermal release of hydrogen is taken into account only in the form of molecules due to the high potential energy of a hydrogen atom in vacuum (2.25 eV). It was experimentally observed that deuterium release from tungsten at temperatures below 1200 K is only in molecular form; above 1200 K some of the deuterium is released in atomic form [26].

All the processes listed above are relevant for the case of interaction of molecular hydrogen with metals. If hydrogen atoms with thermal energies are approaching the metal surface, a part of them will be reflected and the rest will directly occupy the chemisorption sites. Hydrogen atoms or ions with kinetic energies above the activation energy for absorption E_{sb}, i.e., typically above a few eV, can directly penetrate into the metal bypassing the intermediate stage

2. Although a real surface has several different adsorption centres, they are often approximated by one type of chemisorption site with effective values of Q_c and E_c. This approach is valid in the case of impurity coverage up to one monolayer. For thicker impurity layers, dissociation and chemisorption on the layer, as well as diffusion through it, must be taken into account.

of chemisorption. After penetration through the surface, fast atoms (ions) lose their energy in the metal through elastic collisions with lattice atoms and through friction with electrons, and finally, come to rest at interstitial positions [27]. Due to that fact, the concentration of solute hydrogen under ion (of fast atom) irradiation usually greatly exceeds that reached in the case of uptake from the gas phase. At even higher energies starting from about 100 eV, ions (atoms) can produce displacement damage in the metal, as will be later discussed in section 3.4.

2.1.2 Bulk processes

At a given pressure p of H_2 gas surrounding the metal at a temperature T, the equilibrium hydrogen bulk concentration C in the metal obeys Sieverts' law:

$$C = S\sqrt{p}, \tag{2.3}$$

where S [atoms/($m^3 Pa^{1/2}$)] is the hydrogen solubility in the metal, which depends solely on the properties of the metal and does not depend on the surface conditions. The solubility has an Arrhenius-like temperature dependence:

$$S = S_0 \exp\left(-\frac{E_S}{k_B T}\right), \tag{2.4}$$

where S_0 is the pre-exponential factor, E_S is the heat of hydrogen solution in the metal, which represents the energy of a hydrogen atom in the bulk relative to that in H_2 gas (Fig. 2.1). For all metals E_S varies from –1 eV to 1 eV [28]. Based on the sign of E_S, metals can be divided into two categories: metals with a positive heat of solution ($E_S > 0$), such as tungsten, molybdenum, iron, in which the absorption of hydrogen is endothermic, and metals with a negative heat of solution ($E_S < 0$), such as titanium, tantalum, vanadium, in which the absorption of hydrogen is exothermic. The metals with a negative heat of solution always exhibit larger concentrations of absorbed hydrogen compared with that in metals with a positive heat of solution. Sieverts' law is valid only for moderate gas pressures when H_2 gas still can be treated as an ideal gas. In addition, the value of E_S is independent of the concentration of solute hydrogen only at low concentrations – at high concentrations the interaction of hydrogen atoms in the lattice becomes non-negligible.

Experiments on ion channelling in hydrogen-loaded metals, as well as atomistic calculations, indicate that in metals with a body-centred cubic lattice (bcc), such as tungsten, solute hydrogen occupies tetrahedral interstitial sites, whereas in metals with a face-centred cubic lattice (fcc), such as nickel, solute hydrogen occupies octahedral sites (Fig. 2.2) [28–30]. Hence, the potential energy landscape for a hydrogen atom in a metal consists of a series of maxima and minima with the minima corresponding to the equilibrium interstitial positions. At medium temperatures, the diffusion of hydrogen atoms in a metal is a sequence of random (when no external forces are present) jumps between neighbouring

interstitial positions. In order to jump to an adjacent site, a hydrogen atom needs to gain an additional energy E_D (Fig. 2.1), which is referred to as the activation energy for hydrogen diffusion. Hydrogen atoms receive this energy due to fluctuations of the thermal oscillations of the lattice, and the higher the temperature of the metal the higher is the probability to receive a sufficient amount of energy. At low temperatures (below 200 K for tungsten [31]) quantum tunnelling effects start playing a role. At sufficiently high temperatures the influence of the potential barriers of interstitial sites becomes small, therefore, hydrogen atoms experience practically free motion [28]. In tungsten such a behaviour has never been observed even at temperatures as high as 2400 K [32].

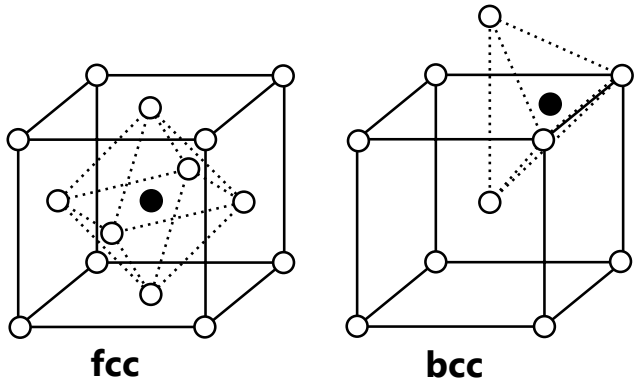

Fig. 2.2: Octahedral and tetrahedral interstitial sites in fcc and bcc lattices, respectively [33]. The hollow circles represent the lattice atoms and the filled circles represent the respective interstitial sites.

In the case of classical diffusion in the intermediate temperature region (which is relevant for fusion applications), the diffusive flux $\mathbf{J}$ [atoms/(m^{2}s)] obeys Fick's first law:

$$\mathbf{J}(\mathbf{r},t) = -D\nabla C(\mathbf{r},t), \tag{2.5}$$

where $C(\mathbf{r},t)$ is the local concentration of solute hydrogen and $D(\mathbf{r},t)$ [m^2/s] is the hydrogen diffusion coefficient in the metal. It also has an Arrhenius-like temperature dependence:

$$D = D_0 \exp\left(-\frac{E_D}{k_B T}\right). \tag{2.6}$$

This law is valid for the case of low hydrogen concentrations, i.e., when hydrogen atoms in the lattice do not interact with each other. For cubic crystals (bcc and fcc) the diffusion coefficient is isotropic, which is not the case for the metals with a hexagonal close-packed (hcp) lattice, e.g., beryllium.

When external forces for a hydrogen atom are present in the lattice, e.g., a temperature gradient, a gradient of mechanical stresses, an electric field, etc., additional terms will appear in Eq. 2.5.

Recalling the continuity equation, the equation describing the evolution of the hydrogen concentration profile with time $C(\mathbf{r}, t)$ will be given by:

$$\frac{\partial C(\mathbf{r}, t)}{\partial t} = -\nabla \cdot \mathbf{J}(\mathbf{r}, t) + S(\mathbf{r}, t), \tag{2.7}$$

where $S(\mathbf{r}, t)$ is the density of volumetric hydrogen sources. This equation is sometimes referred to as the diffusion equation or Fick's second law.

It should be also noted that some other mechanisms of hydrogen transport in metals, apart from lattice diffusion through interstitial sites, exist. The widely discussed mechanisms are: transport by moving dislocations, diffusion along grain boundaries and dislocation cores ("pipe diffusion") [34, 35].

2.2 Hydrogen interaction with defects in metals

All the information given above is valid for single crystals of metals with a perfect lattice. In reality, however, every metallic sample has some lattice imperfections. The most common defect types are illustrated in Fig. 2.3. Some of these defects ("intrinsic"), such as dislocations, impurities, pores, and grain boundaries, are introduced in the material during the manufacturing process. Other types of defects ("radiation defects"), such as vacancies, vacancy clusters, dislocation loops, irradiation-induced voids, bubbles, and blisters, are created during the irradiation of the metal with energetic ions, electrons, or neutrons. Many experimental results, as well as atomistic calculations, lead to the conclusion that lattice defects act as trapping sites for hydrogen [27, 30, 36]. This is mainly attributed to hydrogen attraction to regions of reduced electron density, and the more open the defect the larger is the binding energy E_b. For example, single vacancies are expected to trap hydrogen more strongly than dislocations, but less strongly than vacancy clusters (voids). Near defects the potential energy of a hydrogen atom is lower compared with that in an interstitial site by the value of E_b (Fig. 2.1), consequently, the residence time of a hydrogen atom in such a site will be much larger. The trapping sites are also characterized by the activation energy for trapping E_{tr}, the energy barrier for a hydrogen atom to enter the trapping site, and by the detrapping energy $E_{dt} = E_b + E_{tr}$, the energy barrier for hydrogen escape.

Two kinds of trapping sites exist: saturable and non-saturable. Saturable traps, like vacancies, dislocations, and impurities, can accommodate only a limited number of hydrogen atoms. Voids (or bubbles) containing molecular hydrogen are considered to be unsaturable when the hydrogen pressure in them can grow to such a high level that its volume is increased by punching out self-interstitial dislocation loops; then the pressure decreases and more hydrogen can be stored in it [33]. In addition, in some metals formation of hydrides (i.e., MeH_x compounds where x can exceed one) takes place at sufficiently high concentrations of solute hydrogen exceeding a certain, temperature-dependent limit (usually shown as a phase diagram of a hydrogen-metal system) [28].

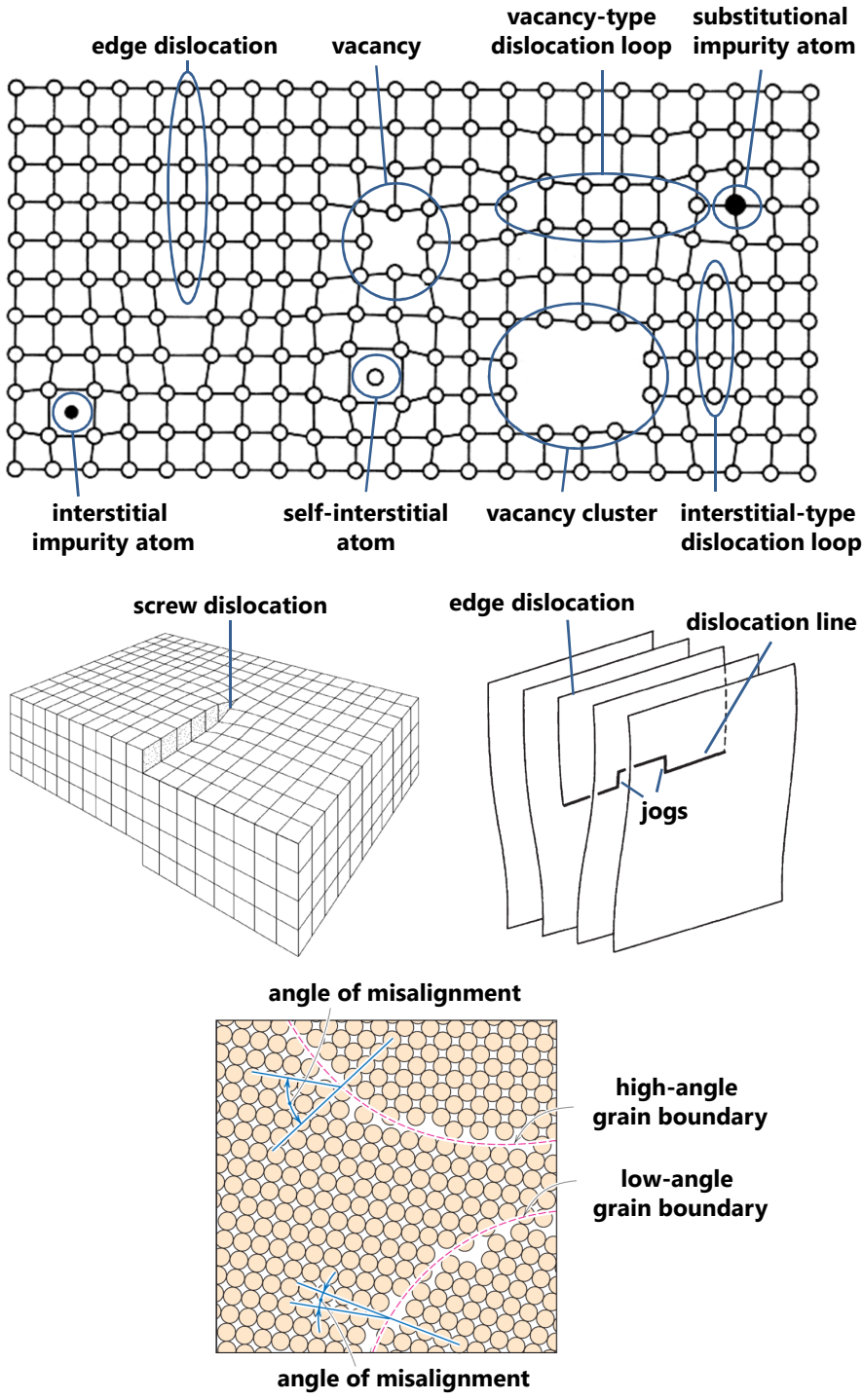

Fig. 2.3: Various types of lattice defects in metals based on [37–39]. The lower plot illustrates low- and high-angle grain boundaries.

2.3 Mathematical description of hydrogen transport and trapping

To describe the dynamics of hydrogen transport and trapping, two states of hydrogen in a metal are treated: 1. the solute hydrogen which occupies interstitial positions in the lattice and travels via thermally activated diffusion; 2. the trapped hydrogen, i.e., the hydrogen atoms located in various kinds of trapping sites [27, 36]. Solute hydrogen can become trapped by entering trapping sites and can be released from them via thermally activated detrapping. Each type of trapping site i is characterised by the concentration profile $N_t^i(\mathbf{r}, t)$ and the values of E_{dt}^i and E_{tr}^i. The governing equations comprise Fick's second law for the diffusion of interstitial atoms (Eq. 2.7) with a source term representing the exchange between the solute and trapped populations, and the equations describing the rates of trapping and detrapping for each kind of trap. The one-dimensional description is sufficient in many cases, but some problems require two- or three-dimensional treatment [40].

In the case of the presence of only saturable traps the governing equations are given by:

$$\frac{\partial C(x,t)}{\partial t} = \frac{\partial}{\partial x}\left(D(x,T(t))\frac{\partial C(x,t)}{\partial x}\right) - \sum_{i=1}^{p}\frac{\partial C_t^i(x,t)}{\partial t} + S(x,t), \tag{2.8}$$

$$\frac{\partial C_t^i(x,t)}{\partial t} = \nu_{tr}^i \exp\left(-\frac{E_{tr}^i}{k_B T}\right) C(x,t)\frac{\left(N_t^i(x,t) - C_t^i(x,t)\right)}{\rho} - \\ -\nu_{dt}^i C_t^i(x,t)\exp\left(-\frac{E_{dt}^i}{k_B T}\right), \tag{2.9}$$

where $C_t^i(x,t)$ is the local concentration of trapped hydrogen in the trap type i, ν_{tr}^i and ν_{dt}^i are the trapping and detrapping attempt frequencies, respectively, $S(x,t)$ is the additional hydrogen source term (e.g., implantation), ρ is the atomic density of the metal, and p is the number of trap types.

The general form of Eqs. 2.8 and 2.9 was first proposed by McNabb and Foster [41]. In most cases, the traps are assumed to be static, i.e., immobile and their transformation (annealing and clustering) at elevated temperatures is neglected. The trapping attempt frequency is usually assumed to be equal to that for a diffusive jump between two adjacent interstitial sites and the activation energy for trapping is assumed to be equal to the activation energy for diffusion: $\nu_{tr}^i = D_0/(z\lambda^2)$, $E_{tr}^i \equiv E_D$, where z is the number of solute sites per host lattice atom, $\lambda = \varkappa a_0$ is the distance between the neighbouring interstitial sites, a_0 is the lattice constant, and $\varkappa$ is a geometrical factor [42]. The detrapping attempt frequency is either assumed to be of the same order of magnitude as the lattice vibration frequency (approximated by the Debye frequency) and is taken to be equal to 10^{13} s^{-1}, or is assumed to be equal to the

trapping attempt frequency. Occasionally it is regarded as a free parameter. The detrapping attempt frequency for a hydrogen atom in a vacancy in tungsten calculated using density functional theory (DFT) is indeed close to 10^{13} s^{-1} [43, 44].

This classical model assumes that one trap can accommodate only one hydrogen atom. However, DFT calculations predict that even simplest types of defects (e.g., single vacancies) can accommodate several hydrogen atoms and the detrapping energy decreases with increasing fill-level of the trap [45]. A model taking this phenomenon into account was recently proposed by Schmid et al. [46]. This model is able to explain hydrogen isotope exchange in metals at low temperatures, which cannot be described in terms of the classical model [47, 48]. Concurrently, in the case of mono-isotopic experiments this model yields practically the same results as the classical model.

The boundary conditions used for solving the set of Eqs. 2.8 and 2.9 vary among different researchers. In the simplest case the effective recombination rate coefficient K_r is assumed to be infinitely high ($K_r \to \infty$), so in order to have a finite desorption flux from the surface (Eq. 2.1), the subsurface concentration of solute hydrogen should be equal to zero: $C(x = 0, L; t) = 0$, where L is the material thickness [49]. The second most frequently used approach is assuming that the diffusive flux from the bulk to the surface is equal to the desorption flux from the surface [25, 50]:

$$2K_r C^2(t) = \pm D \frac{\partial C(t)}{\partial x}\bigg|_{x=0,L} . \tag{2.10}$$

This approach assumes a local equilibrium between the hydrogen concentration on the surface and in the subsurface layer (by using the effective recombination rate coefficient), and that the subsurface concentration immediately establishes accordingly to the diffusive flux to the surface. More rigorous models treat both surface and subsurface concentrations of hydrogen (without assuming local equilibrium between them) [51, 52].

For the set of Eqs. 2.8 and 2.9 with the respective boundary conditions exact (or approximate) analytic solutions can be obtained only for a few simple problems [27, 53], hence, in most cases they have to be solved numerically. For that purpose a number of computer codes have been developed, for instance, TMAP7 [50], TESSIM [54], MHIMS [52], CRDS [40], and others [51, 55, 56].

2.4 Determination of hydrogen binding energies with defects from thermal desorption measurements

For studying hydrogen interaction with defects in metals, thermal desorption spectroscopy (TDS) is often used. A detailed description of the method is given

in section 4.3.2. The mathematical description of hydrogen release during TDS is based on the diffusion-trapping model described above. The most common way to extract the parameters of trapping sites in the material is fitting of simulated TDS spectra to experimental ones [40, 54, 56, 57]. A large uncertainty in the resolution of this inverse problem is given by the fact that the result of a TDS spectrum simulation depends on many input parameters of the model (hydrogen detrapping energy, hydrogen diffusivity in the material, trap concentration profile, initial distribution of trapped hydrogen, recombination rate at the surface). In order to reduce the number of free parameters, experimentally determined or theoretically calculated values of hydrogen diffusivity and recombination rate at the surface are typically used (although there is a large scatter in the reported data on these values, see sections 3.1 and 3.2). Trap profiles are usually deduced based on measured hydrogen concentration profiles in the material. In addition, fitting of a set of TDS spectra using an identical set of input parameters gives more credibility to the model. Nevertheless, some degree of freedom is still left in this approach, thus, the uniqueness of a solution is not guaranteed. It should be stressed that the main ill-defined parameter is the recombination rate at the surface since in most cases the TDS measurements are carried out *ex situ* and the state of the surface is unknown.

In the case of a very fast hydrogen recombination rate at the surface, which means that surface effects affect neither the TDS peak position nor its shape, i.e., only bulk processes (trapping, detrapping, and diffusion) determine the features of TDS spectra, two limiting hydrogen release regimes were identified by Guterl et al. [53]: The detrapping-limited regime and the retrapping-limited regime. In the first case, the concentration of trapping sites N_t (expressed as atomic fractions) is so low ($N_t \ll (\lambda/\Delta)^2$, where Δ is the characteristic location depth of trapped hydrogen) that a hydrogen atom diffuses to the surface without being retrapped by other traps after release from a trap. In the second case, the concentration of traps is high enough ($N_t \gg (\lambda/\Delta)^2$), so that a hydrogen atom released from a trap can be retrapped many times by empty traps before reaching the surface.

In the case of the detrapping-limited regime, the relation between the hydrogen detrapping energy E_{dt} from a defect, the heating rate β during TDS measurements, and the respective peak temperature T_m in a TDS spectrum, is expressed in the following way:

$$\ln\left(\frac{\beta}{T_m^2}\right) = \ln\left(\nu_{dt}\frac{k_B}{E_{dt}}\right) - \frac{E_{dt}}{k_B}\frac{1}{T_m}. \tag{2.11}$$

In the case of the retrapping-limited regime, the equation is the same, but the sum $E_b + E_D$ appears instead of E_{dt}:

$$\ln\left(\frac{\beta}{T_m^2}\right) = \ln\left(\nu_{\text{eff}}\frac{k_B}{E_b + E_D}\right) - \frac{E_b + E_D}{k_B}\frac{1}{T_m}, \tag{2.12}$$

where $\nu_{\text{eff}} = \nu_{dt} D_0/(\nu_{tr}\Delta^2)$ is the effective detrapping attempt frequency, which depends both on the properties of the trapping sites and of the bulk.

Thus, depending on the release regime, either the detrapping energy E_{dt} or the sum $E_b + E_D$ can be directly determined from the slope of the Arrhenius-like plot $\ln\left(\beta/T_m^2\right)$ versus $1/T_m$ in a series of TDS measurements performed using identical samples and different heating rates (the so-called Kissinger method). This approach does not require any prior knowledge, i.e., the trap profile, the initial distribution of trapped hydrogen, and the material properties, and the only requirement is a sufficiently high recombination rate at the surface. In addition, this method allows determining either E_{dt} or $E_b + E_D$ independently of the detrapping attempt frequency ν_{dt}, while this is not possible by fitting numerically simulated TDS spectra to experimental ones where the value of ν_{dt} has to be assumed.

Although all the considerations described above are made for a metal having only one type of trapping site (characterised by the values of E_b and E_{dt}) and each trap can accommodate only one hydrogen atom, the same dependences are valid for every trap type in the metal as long as they do not evolve during the TDS measurements. The same dependences should be also valid in the case of trapping of several hydrogen atoms by each trap since it can be approximated by several distinct trapping sites. From the experimental point of view, in the case of a material with several types of trapping sites, TDS peaks must be well-resolved to determine their positions accurately.

Chapter 3

Hydrogen in tungsten

The investigations of hydrogen interaction with tungsten started at the beginning of the 20th century with pioneering studies by Langmuir. The issues addressed in those investigations were driven by practical points of view, such as the interaction of H_2 gas with hot tungsten filaments, as well as from the fundamental point of view, e.g., hydrogen adsorption and surface reconstruction. Later on, at the beginning of the 1990s, tungsten started to be considered as a candidate material for the divertor of ITER, which gave rise to studies of the interaction of hydrogen ions and plasmas with tungsten. The results of the studies performed before 2002 are summarized by Causey [49], whereas the more recent results are highlighted in the reviews [47, 58–60].

While in the previous chapter the general features of hydrogen interaction with metals were described, this chapter focusses on the properties of the hydrogen-tungsten system. The existing data on hydrogen solubility, diffusivity, recombination rate at the surface, interaction with lattice defects, and retention in tungsten is reviewed. In addition, the creation and thermal evolution of radiation- and hydrogen-induced defects in tungsten are discussed. At the end of the chapter, the objectives of the present thesis are presented.

3.1 Solubility and Diffusivity

There exists only a limited number of experiments to determine the fundamental parameters of hydrogen-tungsten interactions, namely hydrogen solubility and diffusivity, as summarized in reviews [49, 60].

It is generally agreed that the hydrogen solubility in tungsten is extremely low and the most reliable value was reported by Frauenfelder [32]:

$$S(T) = 9 \times 10^{-3} \exp\left(-\frac{1.04\ \text{eV}}{k_B T}\right) \left[\frac{\text{H}}{\text{W} \cdot \text{atm}^{1/2}}\right]. \tag{3.1}$$

The heat of hydrogen solution E_S calculated by DFT (in the range of 0.86–1.04 eV [44, 45]) is close to that measured by Frauenfelder. The DFT calculations also demonstrate that in a perfect tungsten lattice hydrogen prefers to occupy tetrahedral interstitial sites [45], which is backed by ion channelling measurements [29].

The commonly accepted value of the hydrogen diffusivity in tungsten was also obtained by Frauenfelder [32]:

$$D(T) = 4.1 \times 10^{-7} \exp\left(-\frac{0.39\ \text{eV}}{k_B T}\right) \left[\frac{\text{m}^2}{\text{s}}\right]. \tag{3.2}$$

Frauenfelder's data are considered as the most reliable since the measurements were carried out at such high temperatures (1100–2400 K) where hydrogen trapping in lattice defects in tungsten is expected to be negligible. The measurements by other researchers were performed at lower temperatures and were likely affected by trapping effects, therefore, the reported values are lying below the extrapolation of the high temperature data by Frauenfelder (Fig. 3.1). Heinola and Ahlgren [31] suggested that the data in Frauenfelder's experiment at temperatures below 1500 K, when trapping effects still could play a role, should be omitted for the extrapolation to low temperatures. This exclusion decreases the activation energy for hydrogen diffusion E_D derived from Frauenfelder's experiment from 0.39 eV to 0.25 eV (Fig. 3.1), thus bringing it closer to the values obtained by using DFT (around 0.2 eV [44, 45]). DFT calculations indicate that the preferred path for hydrogen diffusion in single crystalline tungsten is via adjacent tetrahedral sites [45].

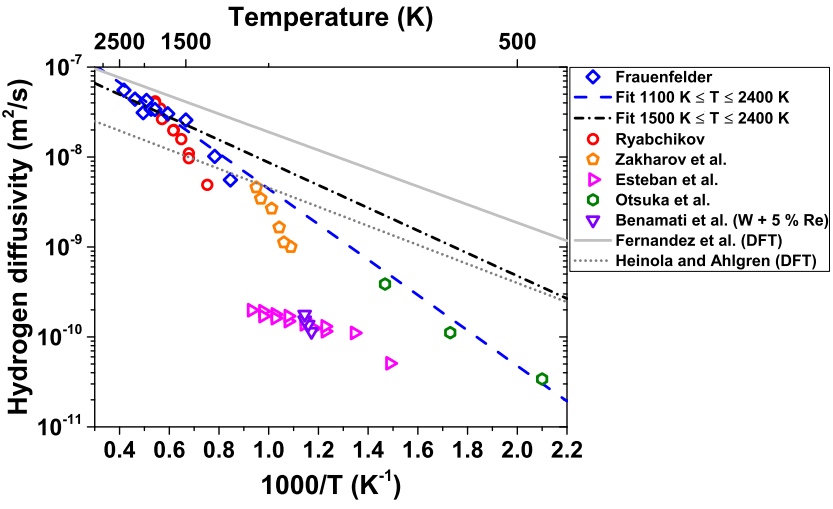

Fig. 3.1: Some of the reported experimental [32, 61–65] and DFT [31, 44] data on the hydrogen diffusivity in tungsten.

3.2 Recombination rate

The existing data on the hydrogen recombination rate at the tungsten surface are also very limited (Fig. 3.2) [49, 59]. The effective recombination rate coefficients determined in ion-driven permeation experiments by Anderl et al. [66] and Gasparyan et al. [67] are many orders of magnitude smaller and have an opposite temperature dependence compared with the predictions based on the Pick and Sonnenberg model [25] for a clean tungsten surface (Eq. 2.2 with $E_c = 0$, $s_0 = 1$, E_S and S_0 taken from Frauenfelder [32]). Gasparyan et al. [67] showed that both their data and the data of Anderl et al. [66] cannot be described in terms of the Pick and Sonnenberg model by the adjustment of the activation energy for chemisorption E_c. This can be due to the fact that in permeation experiments the hydrogen surface coverage Θ is non-negligible [51], while Eq. 2.2 is obtained under the assumption of $\Theta \ll 1$. Causey [49] suggested that the hydrogen recombination rate at the tungsten surface is very high (i.e., never acts as limiting factor) under fusion reactor conditions.

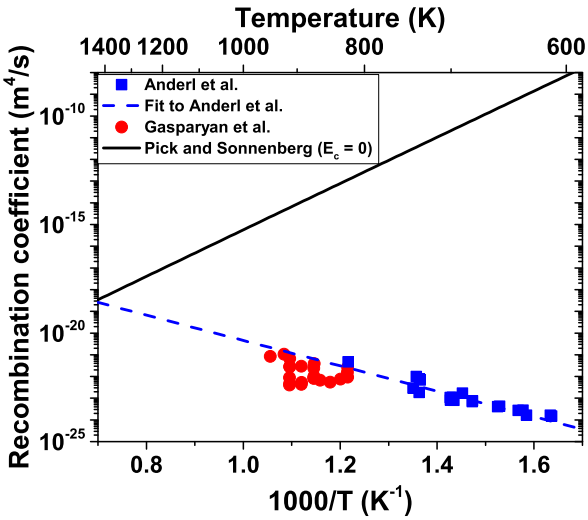

Fig. 3.2: The comparison of experimental [66, 67] and theoretical (for a clean surface) [25] values of the effective hydrogen recombination rate coefficient at the tungsten surface.

3.3 Interaction with lattice defects

Due to the extremely low hydrogen solubility in tungsten, the hydrogen inventory in it is determined by the presence of lattice defects acting as trapping sites. However, revealing the roles of individual defects on the retention is challenging since several defect types are typically present simultaneously in investigated tungsten samples and it also appears that some of the defects have

very close values of binding energies [49, 68]. In some studies, the formation of blister-like structures took place, which also obscures the interpretation of the data. Thus, the proposed explanations are often speculative, resulting in many contradictory statements in the literature. Below the main experimental and theoretical findings on this topic will be briefly reviewed.

3.3.1 Intrinsic defects

There is no agreement regarding the hydrogen binding properties of dislocations in tungsten. Ogorodnikova et al. [56] reported that dislocations and grain boundaries have a quite low detrapping energy of 0.85 eV, which is in line with DFT calculations by Terentyev et al. [34]. However, Manhard [69] attributed traps with the detrapping energy of 1.25 ± 0.11 eV to dislocations. Anderl et al. [66] observed a correlation between the reduction of the concentration of traps with the detrapping energies in the range of 1.34–1.56 eV and the reduction of the dislocation density, although it was admitted that these energies seem to be too high for dislocations. DFT calculations [34] also predict that once the number of trapped hydrogen atoms on a screw dislocation segment exceeds eight, a vacancy on a dislocation line will be formed (which is equivalent to a pair of jogs with a spacing of one interatomic distance), which traps hydrogen with a considerably higher binding energy.

DFT calculations [43, 70] predict that carbon and oxygen substitutional impurity atoms in a tungsten lattice should strongly bind hydrogen (with the detrapping energies of 1.51 eV and 1.45 eV, respectively), while argon, rhenium, and osmium atoms exhibit much smaller detrapping energies.

There exist several types of hydrogen adsorption sites on the tungsten surface having the heats of chemisorption Q_c in the range of 0.3–0.8 eV [71, 72].

3.3.2 Radiation defects

There are only a few experimental studies dedicated to the investigation of hydrogen interaction with vacancies in tungsten. The widely accepted value of the detrapping energy from vacancies reported by Eleveld and van Veen [57] is 1.43 ± 0.02 eV. DFT calculations predict that a vacancy can trap up to 6–14 hydrogen atoms at 0 K with the detrapping energy decreasing with increasing the number of trapped hydrogen atoms, albeit there is a large scatter in the reported values (1.29–1.79 eV for the first trapped atom) [30, 44, 45].

It is generally agreed that vacancy clusters bind hydrogen stronger than vacancies, but the dependence of the detrapping energy on the cluster size is unknown. Inside a large vacancy cluster (or any cavity) hydrogen can be present both in atomic and molecular form. Hydrogen atoms entering the cluster are first trapped on its surface; as the concentration of trapped atoms increases, they can recombine into H_2 molecules and desorb into the cluster volume. For

atomic hydrogen trapped in large[1] vacancy clusters the trapping mechanism is considered to be similar to hydrogen chemisorption on a surface [73]. The detrapping energy is then expressed as $E_{dt} = E_S + E_D + Q_c = (1.73–2.23)$ eV (see Fig. 2.1) using E_S and E_D from [32] and Q_c from [71]. The experimentally determined values of 1.8 eV [72] and 2.05 ± 0.15 eV [67] are in line with these estimates.

From thermodynamic considerations, for the molecular hydrogen inside the cavity the binding energy should be the same as the heat of hydrogen solution E_S (at low gas pressures), and the detrapping energy is expressed as $E_{dt} = E_S + E_D = 1.43$ eV [73].

Self-interstitial atoms are expected to have a very small hydrogen detrapping energy of 0.43 eV [43], while interstitial type dislocation loops are expected to trap hydrogen more strongly. Molecular statics (MS) simulations by Grigorev et al. [74] indicate that dislocation loops with a Burgers vector of $\mathbf{b} = (1/2)\langle 111\rangle$ exhibit a wide range of detrapping energies up to 1.5 eV, whereas for the $\mathbf{b} = \langle 100\rangle$ loops it is up to 2 eV.

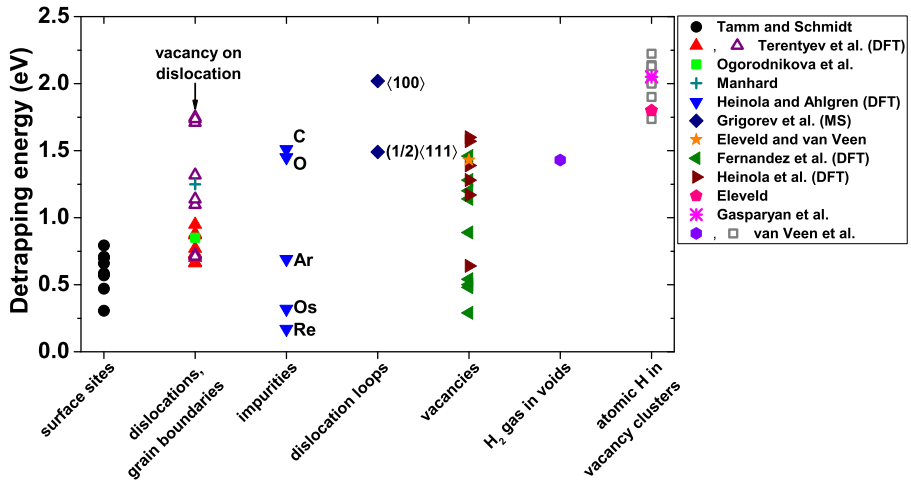

Fig. 3.3: Some of the reported hydrogen detrapping energies from various defects in tungsten derived either from experimental data [56, 57, 67, 69, 71, 72] or from calculations [34, 43, 44, 70, 74]. Detrapping energies of atomic hydrogen from vacancy clusters and of H_2 gas from large vacancy clusters (voids) are estimated as $E_S + E_D + Q_c$ and $E_S + E_D$ [73], respectively, using E_S, E_D, and Q_c from [32, 71]. Note that DFT calculations predict that dislocations and vacancies can trap several hydrogen atoms and the detrapping energy decreases with increasing number of trapped atoms.

Fig. 3.3 summarizes the detrapping energies reported above. Due to the possibility of trapping multiple hydrogen atoms in some defects, they show a broad spectrum of detrapping energies. In addition, some of the defects seem to have very close values of detrapping energies (e.g., vacancies and voids containing

1. The cluster is large enough if its surface properties are close to those of a free metal surface.

H_2 gas), which makes it challenging to resolve the corresponding peaks in TDS spectra. Nevertheless, the general trend mentioned in section 2.2 that the detrapping energy increases with increasing the open volume associated with the defect (i.e., dislocations → vacancies → vacancy clusters) is visible.

3.4 Creation and thermal evolution of radiation defects

Irradiation of metals by high-energy particles (electrons, ions or neutrons) results in the formation of lattice defects ("radiation defects"). The defect creation can be separated into two categories: the primary defects formed directly (within a few tens of ps) after the particle impact via atomic collisions, and the long-time scale (nanoseconds to years) defect evolution induced by thermally activated processes.

After an energetic particle has penetrated through the surface of a metal, it starts slowing down through elastic collisions with lattice atoms and friction with electrons. The maximum kinetic energy $E_{\max}$ that can be transferred in a head-on collision between the incident particle (ion or neutron) and the target atom is expressed by:

$$E_{\max} = E_0 \frac{4mM}{(m+M)^2}, \tag{3.3}$$

where E_0 is the incident particle energy, m and M are the masses of the incident particle and the target atom, respectively. When the incident particle is an MeV electron with $m \ll M$ and $E_0 \ll Mc^2$, the relativistic equivalent of Eq. 3.3 has to be used:

$$E_{\max} = \frac{2E_0}{Mc^2}\left(E_0 + 2m_e c^2\right), \tag{3.4}$$

where c is the speed of light in vacuum. The binding energy of a metal atom in its lattice site is only a few eV, but in order to create a stable displacement (the so-called "Frenkel pair", a vacancy-interstitial pair) it is necessary to move the atom far away from its original site, thus, a relatively large energy transfer above a certain threshold (typically 10–50 eV) is required. Due to the crystal anisotropy, this threshold depends on the knock-on direction and there exist pronounced minima corresponding to specific low-index crystallographic directions [33, 75]. Its average value is called the effective displacement threshold energy E_d. In tungsten the experimentally determined threshold energies are: 42 eV in the ⟨100⟩ direction, 44 eV in the ⟨111⟩ direction, and 70 eV in the ⟨110⟩ direction [76], which yields an effective displacement threshold energy of 55.3 eV [77]. Despite these experimental results, the American Society for Testing and Materials (ASTM) recommends using the effective displacement threshold energy of 90 eV for tungsten [78]. This value has been largely adopted and is used in most of investigations.

At sufficiently high energy transfer, the recoil atom (also referred to as a primary knock-on atom (PKA)) can cause further displacements resulting in the formation of a cascade of successive collisions. In the case of moderate PKA energies, the density of moving atoms within the cascade volume will be low enough so that its different branches will not overlap, i.e., so-called "linear cascades" having a tree-structure shape will be present. This situation holds in the case of irradiation with light projectiles of not very high energies.

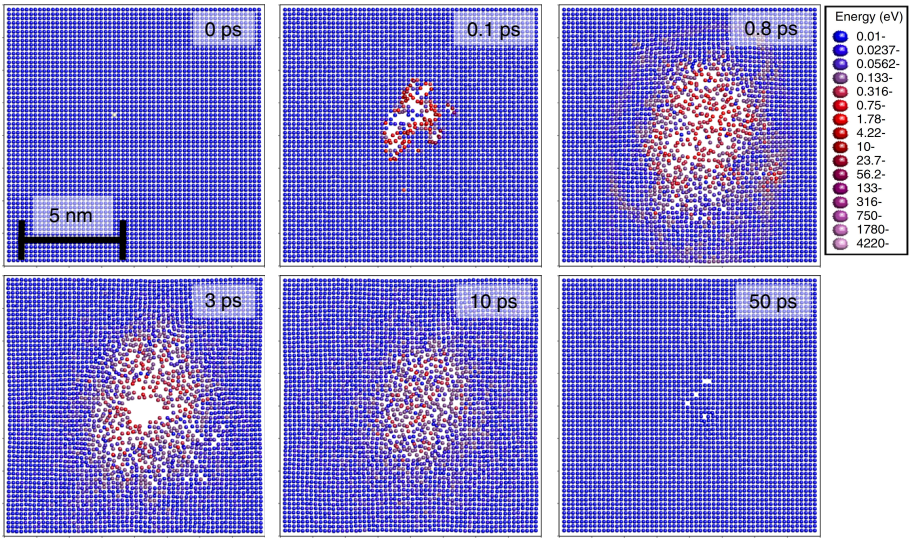

Fig. 3.4: A sequence of time frames illustrating the evolution of a collision cascade in the heat spike regime in gold initiated by a 10 keV PKA at a material temperature of 0 K simulated using molecular dynamics [79]. Each dot shows the position of an atom, and the colours indicate the kinetic energy of each atom given by the scale on the right.

In the case of high PKA energies, which is relevant for irradiation with heavy ions or neutrons, a large number of atoms in a limited region of the material will be displaced in less than 1 ps, as illustrated in Fig. 3.4. Because of that, collisions between moving atoms within the cascade volume will be frequent, therefore, they will eventually get a Maxwell–Boltzmann distribution of kinetic energies. This is called a heat (or thermal) spike which lasts for a few tens of picoseconds and is characterized by the presence of an underdense region in the cascade centre and an overdense region around it. During this phase, the spike gradually grows and cools via energy transfer to the surrounding material. Eventually, the heat spike cools down (quenches) to ambient temperature, which can be regarded as crystallization of the molten material. During this phase, most of the displaced atoms recombine with vacancies, thus, the resulting number of defects is considerably smaller than the initial number of displacements. As this process does not require any thermally activated defect migration (atom motion is driven by the PKA energy), this recombination is called athermal. The resulting damage structure then consists of a few isolated

interstitials and interstitial clusters at the periphery of the heat spike region, some randomly distributed vacancies, and a vacancy cluster in the centre of the heat spike. Formation of defect clusters is inherent for energetic displacement cascades, and it distinguishes neutron and heavy ion irradiation from electron or light ion irradiation, which predominantly produces isolated Frenkel pairs [33, 80]. As an example, Fig. 3.5 illustrates schematically the differences in the damage morphology after 1 MeV particle irradiation of nickel.

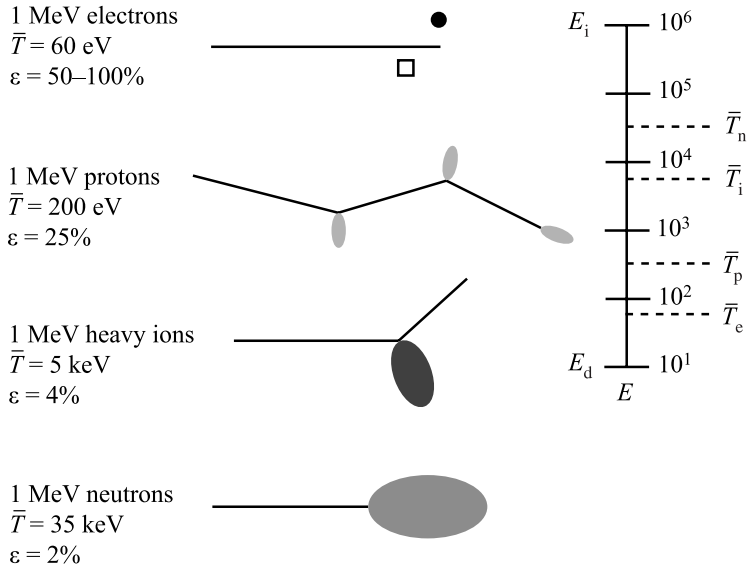

Fig. 3.5: Difference in damage morphology for irradiation of nickel by 1 MeV particles of different types [33]. The average PKA energy $\overline{T}$ and the displacement efficiency ε, defined as the fraction of the produced defects surviving the cascade quench, is provided for each case. The lines schematically illustrate the paths of the incident particles, the ovals show the sizes of the collision cascades, the square represents a vacancy, and the dot denotes an interstitial.

The commonly accepted standard for quantification of the primary radiation damage is the dpa (displacement per atom) expressing the number of displacements from a lattice site per one atom during irradiation [78–80]. The currently used standard proposed by Norgett, Robinson, and Torrens [81] (the so-called NRT-dpa) expresses the number of displacements ν_{NRT} as a function of PKA energy E_{PKA} as:

$$\nu_{\mathrm{NRT}}(E_{\mathrm{PKA}}) = \begin{cases} 0, & E_{dam} < E_d, \\ 1, & E_d \leq E_{dam} < 2E_d/0.8, \\ 0.8E_{dam}/(2E_d), & E_{dam} \geq 2E_d/0.8, \end{cases} \tag{3.5}$$

where E_{dam} is the energy available for damage production, i.e., the PKA energy E_{PKA} corrected for the inelastic energy losses in the cascade computed using the energy partitioning theory of Lindhard. The details of dpa calculations used in the present work are described in appendix A.

This simplified approach ignores the features of cascades in the heat spike regime, i.e., it assumes that defects are produced as Frenkel pairs, neglecting their athermal recombination and clustering. Hence, it is not actually expressing the number of radiation defects remaining in the material. It should be considered only as a radiation exposure parameter, which is useful for comparison of irradiations with different particle types (electrons, ions, neutrons) [79, 80].

Previously the damage production mechanisms in individual cascades were discussed. However, when the radiation fluence (dpa) increases, the defects produced by different cascades will start overlapping, which leads to the formation of more complex defect structures. In addition, the fact that a vacancy-interstitial pair athermally recombines if their separation is less than a few lattice constants results in saturation of the defect concentration at about 10^{-2} atomic fractions (at. fr.) at high damage levels [82, 83].

The picture described above is valid at very low temperatures when both interstitial atoms and vacancies are immobile. At elevated temperatures, the defect migration governs the microstructural evolution of the material [33, 83]. Vacancies and interstitials can migrate by thermally activated diffusion and annihilate at extended sinks (free surfaces, grain boundaries, and dislocations). They can also annihilate by recombining with each other or agglomerate into less mobile (but more stable) extended defects (e.g., vacancy clusters, dislocation loops). Vacancies can also trap impurities (e.g., carbon), which may reduce vacancy mobility and also prevent their annihilation with interstitials.

Five major defect annealing (recovery) stages have been observed in irradiated metals [83, 84]. Stage I corresponds to the onset of self-interstitial mobility. Stage II involves migration and/or dissociation of small interstitial clusters and interstitial-impurity clusters. Stage III corresponds to the onset of vacancy migration. Stage IV is attributed to migration and/or dissociation of vacancy-impurity complexes. Stage V corresponds to dissociation of vacancy clusters.

There is a vast number of studies investigating the recovery of radiation defects in tungsten, as summarized in [84, 85]. The studies of neutron-irradiated tungsten allowed the characteristic temperatures and activation energies of different annealing stages to be identified, but the interpretation of the results is complicated due to the presence of several defect types in the samples (vacancies, vacancy clusters, dislocation loops, and transmutation products). More basic studies investigating the recovery stages of Frenkel pairs have also been carried out, but most of them were performed by measuring the electrical resistivity recovery, which is very sensitive to the presence of defects, but the corresponding changes in the microstructure cannot be directly identified. Studies performed using transmission electron microscopy (TEM) [86] were able to provide information about defect clusters (concentration, sizes), but because of the limit in TEM resolution, clusters smaller than about 1 nm cannot be observed. Defect evolution on the atomic scale was studied using positron annihilation Doppler broadening spectroscopy (DBS) [87, 88] at temperatures ranging from room temperature until full recovery of the defects. These meas-

urements allowed to confirm that recovery stage III corresponds to the onset of vacancy mobility, as well as to detect several substages corresponding to different mean sizes of vacancy clusters, albeit the sizes of clusters could not be determined. These sizes can be extracted from positron annihilation lifetime spectroscopy (PALS) measurements, but the reported measurements [89] were carried out only in a very limited temperature range.

3.5 Hydrogen-induced defects

In addition to the radiation effects described in section 3.4, irradiation of tungsten by hydrogen ions with energies well below the threshold for creating displacement damage (around 1 keV for deuterium ions) can result in the formation of near-surface defects appearing as blister-like structures on the surface. Their type, number density, and sizes are dependent on material temperature, incident ion energy, flux and fluence, the used tungsten grade, and the grain orientation [17, 19, 69, 90–92].

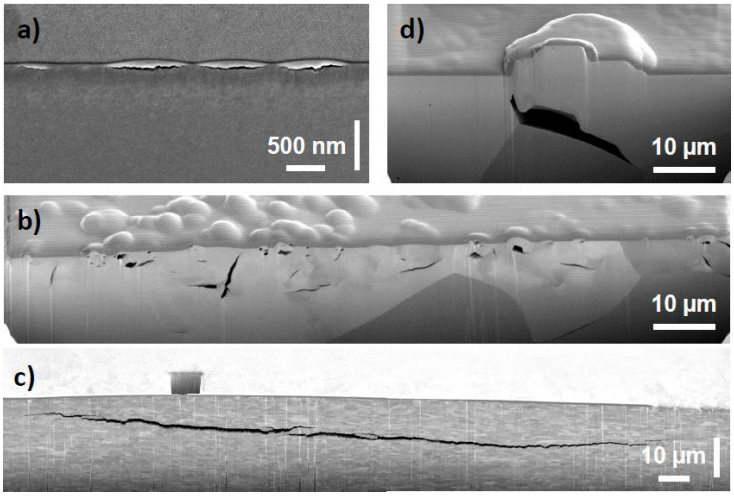

Fig. 3.6: Different kinds of cavities of blister-like structures on tungsten: (a) transgranular cracks parallel to the surface; (b) transgranular cracks aligned to specific crystallographic directions; (c) intergranular cracks; (d) extrusion of the material along the slip system [5].

The observed surface features vary from dome-shaped blisters to stepped plateau-like (or high-dome) and irregularly-shaped three-dimensional structures. All of them will be later referred to as blister-like structures. The shapes and locations of the cavities of the corresponding structures are also different (Fig. 3.6). There are cavities formed by cracks within a single grain (transgranular): (a) running parallel to the surface independent of the grain orientation and (b) running along selected crystallographic directions. There are also cracks formed along grain boundaries (intergranular): (c) running roughly parallel to

the surface and (d) formed by extrusion of the material along gliding planes corresponding to the slip system of tungsten. Except for the case shown in Fig. 3.6(a), the cavities are located far beyond the range of the incident ions. Thus, the high concentration of solute hydrogen during the irradiation is typically suggested to be the driving force for the emergence of blister-like structures. The mechanisms of their further development explaining the differences between various types of structures are not yet clear [5, 58–60].

These surface modifications are typically observed on mirror-polished specimens, while tungsten monoblocks in ITER and future fusion devices will have a technical surface finish (coarse grinded surfaces). Although it was believed for a long time that blistering does not take place on technical surfaces, recently Manhard et al. [93] demonstrated that a rough surface strongly reduces the average blister size and density, but does not lead to their complete suppression.

Recent experiments have also shown that tungsten irradiation with deuterium ions having energies above 100 eV leads to the formation of a 10 nm thick near-surface layer with an extremely high deuterium concentration of around 10^{-1} at. fr. [94]. Furthermore, calculations predict that a high concentration of solute hydrogen facilitates vacancy formation in tungsten [44, 45].

3.6 Fluence dependence of hydrogen retention

There already exists a large body of data on hydrogen isotope retention in tungsten irradiated at different conditions. Fig. 3.7 shows fluence dependences of deuterium retention in polycrystalline tungsten irradiated with ion beams or exposed to plasmas with an incident ion energy in the range of 38–500 eV and at a sample temperature near 500 K. The data is taken from the MIT Report PSFC/RR-10-4 [20] with adding recent results from PISCES-B [21].

As can be seen, the results reported by different researchers show a very large scatter, which can be attributed to differences in experimental conditions (ion energy, flux), differences in the used tungsten grades, etc. The results at high fluences ($> 10^{26}$ D/m^2) are scarce and inconsistent: while in the MIT report it was assumed that deuterium retention tends to saturation at high fluences, the recent results from PISCES-B demonstrate that the retention almost obeys the $\sqrt{\Phi}$ dependence up to 2×10^{28} D/m^2, which is typical for diffusion-limited processes. Note that in some of the experiments included in the MIT report formation of blister-like structures was observed, whereas in the PISCES-B experiments the exposure temperature was higher (643 K), resulting in the absence of these surface modifications. Due to the higher temperature also the total deuterium retention is considerably smaller than for the other data. It was shown by several researchers that the appearance of blister-like structures leads to the introduction of additional trapping sites for hydrogen in the subsurface region of tungsten, which can easily govern the retention [17, 18, 69]. In addition, the presence of blisters with open caps was shown to

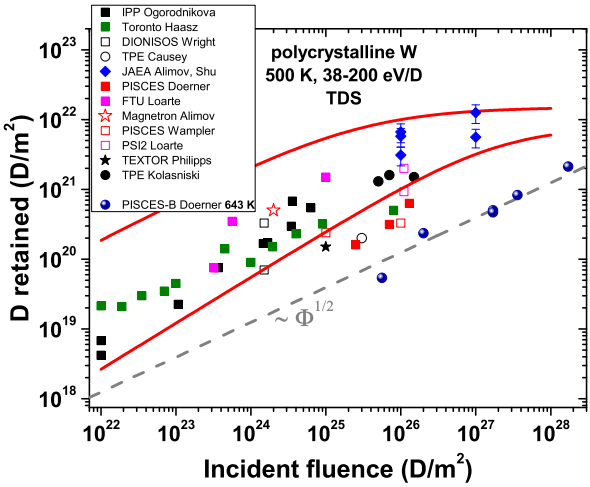

Fig. 3.7: Fluence dependences of deuterium retention in polycrystalline tungsten at a temperature near 500 K and ion energies in the range of 38–500 eV [20]. The solid lines show the bounding limits derived in [20]. Recent results from PISCES-B [21] (note the higher exposure temperature of 643 K) and the square root of fluence scaling of the corresponding data (dashed line) are also added.

enhance the hydrogen reemission rate, resulting in a considerable reduction of the hydrogen transport into the bulk [95]. Hence, extrapolation of the existing data to fluences expected by the end of ITER operation ($\geq 10^{30}$ particles/m^2) is difficult from present understanding.

It should be emphasized that hydrogen retention in tungsten depends on the incident ion flux, not only on the fluence [17, 19]. For example, the temperature dependence of deuterium retention has a flux dependence: at low fluxes the retention decreases monotonically as a function of the exposure temperature, whereas at fluxes above 10^{21} D/m^{2}s it exhibits a maximum [20, 58], and the temperature at which the retention is maximal tends to increase with increasing flux [19]. According to the present understanding, the flux effect on hydrogen retention in metals is a consequence of the interplay between at least the following factors: 1. the solute hydrogen concentration caused by the impinging ion flux, which determines the hydrogen diffusive flux into the bulk and the equilibrium occupancy of trapping sites with hydrogen; 2. the flux dependence of the rate of creation of hydrogen-induced damage in the material; 3. the duration of irradiation needed to accumulate a certain incident fluence, which affects the hydrogen diffusion length in the material.

Note that all the above mentioned results were obtained without taking into account the radiation defects produced by neutrons. The maximum concentration of trapped hydrogen in radiation-damaged tungsten is about 10^{-2} at. fr., which is more than one order of magnitude larger compared with that in pristine tungsten. This maximum trapped hydrogen concentration tends towards saturation at damage levels above 0.23 dpa [96, 97]. With increasing the temperature of

hydrogen loading the trapped hydrogen concentration decreases mainly due to increased thermally activated detrapping. However, at a given temperature and incident ion energy, a higher incident ion flux leads to a higher equilibrium occupancy of trapping sites with hydrogen [98]. Finally, in a fusion reactor environment hydrogen implantation and defect creation by neutron irradiation will take place simultaneously, which can result in synergistic effects, such as stabilization of defects by the presence of hydrogen [94, 99].

The tendencies described above were observed in the case of exposure to a pure hydrogen plasma. In ITER, however, the plasma influx on the divertor targets will contain not only hydrogen isotopes but also impurities (helium, beryllium, nitrogen, etc.), which will strongly affect the appearance of blister-like structures, as well as the hydrogen retention [5, 6].

3.7 Objectives of the present thesis

From the literature data described above, it is evident that a general understanding of hydrogen trapping in tungsten has been already achieved, but that the understanding of hydrogen interactions with different types of lattice defects is still incomplete. A typical problem occurring in many studies is the presence of multiple defect types in the investigated samples, which impedes the identification of the contributions of individual defects.

Therefore, the main objectives of the present work are the following:

- Performing dedicated experiments studying deuterium interaction with single vacancies, vacancy clusters, and dislocations in tungsten by using specially prepared samples having one dominant and well-characterized defect type.
- Investigation of the influence of defects induced by a high-flux deuterium plasma exposure of tungsten to extremely high fluences up to 10^{28} D/m^2.

To achieve these goals, the following approaches have been used: Irradiation by MeV electrons and keV light ions allows introducing predominantly Frenkel pairs, which is the simplest type of radiation defect which provides the basis of more complex defect structures such as vacancy clusters and dislocation loops. While damaging by MeV electrons is the most robust way to introduce exclusively isolated Frenkel pairs, the damaging rates are extremely low, thus, large numbers of samples with reasonable damage levels cannot be produced for systematic studies. Damaging by ions allows increasing the damaging rate by more than one order of magnitude, but small vacancy clusters may be also created and the damaging species are implanted in the target and can be trapped by the created vacancies. The latter can potentially affect the behaviour of vacancies, e.g., reduce their mobility and prevent their annihilation with self-interstitials. In the present work, most of the experiments utilize

damaging by ions (protons and deuterons), in a few experiments damaging by electrons is done for comparison.

The structure of the obtained atomic-scale defects cannot be directly observed in a transmission electron microscope (TEM) but can be studied using positron annihilation lifetime spectroscopy (PALS). Since defects introduced by ion irradiation are located within a few μm beneath the surface, the use of monoenergetic pulsed positron beams of variable energy is required to detect the presence of these defects with a high signal-to-background ratio.

Various densities of dislocations can be introduced in tungsten via plastic deformation to different strains at various temperatures. TEM is a well-established technique for characterization of the properties of introduced dislocations: their type, density, and spatial distribution.

All retention studies in this thesis were performed with deuterium (^{2}H or D) since it is non-radioactive and its natural abundance is very low, allowing to perform background-free measurements. It is expected that all hydrogen isotopes in tungsten at room temperature and above behave similarly, therefore, results obtained in experiments with deuterium should be also valid for tritium[2].

To study the deuterium trapping characteristics of the introduced defects, samples have to be gently loaded with deuterium without introducing additional defects. The temperature of samples during loading should be sufficiently low to avoid defect mobility and significant deuterium detrapping. On the other hand, it should be high enough to promote considerable deuterium diffusion. For these purposes irradiation by low fluxes of low-energy deuterium ions extracted from a low-temperature plasma suits best. However, to unravel the influence of defects introduced by extremely high ion fluxes expected in a divertor of a fusion reactor, the use of linear plasma devices equipped with powerful plasma sources is required.

Concentration profiles of trapped deuterium in the near-surface region, which reflect the total concentration of defects that can be decorated with deuterium under the used exposure conditions, can be measured using nuclear reaction analysis (NRA). Deuterium binding energies with defects can be determined using thermal desorption spectroscopy (TDS). Since deuterium can diffuse beyond the analysis range of NRA, TDS is also useful to determine total deuterium inventories in the samples.

To check for the presence of surface modifications resulting from plasma exposure, such as blister-like structures, both confocal laser scanning microscopy (CLSM) and scanning electron microscopy (SEM) can be used. To examine cavities of blister-like structures, SEM is used in combination with *in situ* focused ion beam cross-sectioning of specimens.

Most of these experimental facilities and analysis techniques are described in the following chapter.

2. The isotope effects due to the mass dependence of the vibrational energy levels of the hydrogen atoms in the lattice are expected to have a negligible impact [28].

Chapter 4

Experimental apparatus and analysis techniques

This chapter describes the experimental techniques used in the present work. First, the devices used for exposure of samples to low- and high-flux deuterium plasmas are described. After that, the facilities used for the introduction of radiation defects by irradiation with ion beams are presented. Then the used analysis techniques for detecting deuterium in samples, namely nuclear reaction analysis and thermal desorption spectroscopy, are discussed in detail. Surface imaging tools (scanning electron microscopy and confocal laser scanning microscopy) are briefly discussed. Finally, positron annihilation lifetime spectroscopy used to detect microscopic open-volume defects in samples is described in detail.

4.1 Deuterium plasma exposure

4.1.1 PlaQ

The exposures of samples to a low-flux deuterium plasma were carried out in the PlaQ plasma device (IPP, Garching, Germany) [100]. A schematic drawing of the setup is shown in Fig. 4.1.

The residual pressure close to 2×10^{-6} Pa in the vacuum chamber is obtained after overnight pumping by a turbomolecular pump in series with a multi-stage roots pump. The plasma is generated in a remote electron-cyclotron resonance (ECR) discharge confined in a stainless steel cage. Microwaves (2.45 GHz) are launched into the vessel through a waveguide terminated by an aluminium oxide window, and the resonant magnetic field of 87.5 mT is created by a single water-cooled magnetic coil. The plasma beam expands through an aperture in the bottom of the cage and reaches the sample holder. A tungsten grid in the aperture shields the holder from the microwaves. Under standard conditions,

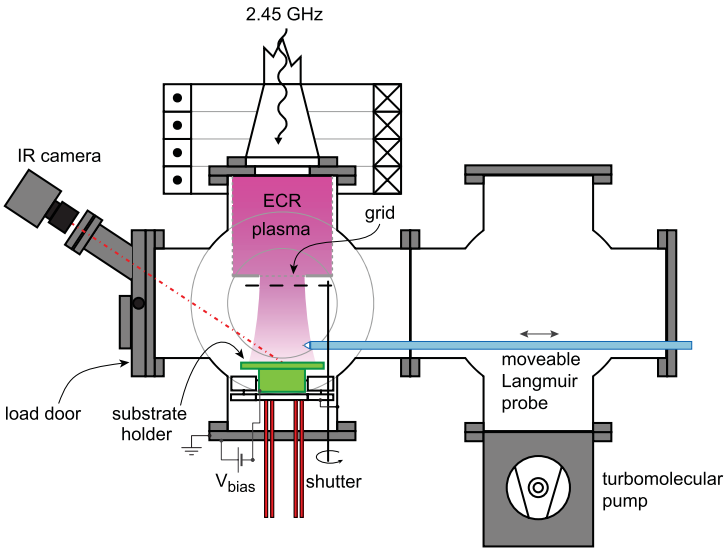

Fig. 4.1: A schematic drawing of the PlaQ plasma device [93].

the discharge operates at a D_2 pressure of 1 Pa and a microwave power around 140 W. The absolute deuterium ion flux impinging on the sample holder was quantified by Manhard et al. [100] using a retarding field analyser and a plasma monitor. Under standard conditions, the flux consists predominantly of D_3^+ ions (94 %) with small contributions of D_2^+ (3 %) and D^+ (3 %) ions. The energy of the impinging ions can be varied by applying a negative bias voltage V_{bias} to the sample holder. Taking into account the plasma potential of −15 V, the mean incident energy per deuteron E for the dominant ion species D_3^+ is then expressed as: $E = (1/3)e|V_{bias}| + 5$ eV/D, where e is the elementary charge. It should be kept in mind that the minority species (D_2^+ and D^+) have a higher incident energy per deuteron. In the present experiments, a bias voltage of −15 V was used, corresponding to a mean incident particle energy of 10 eV/D. This energy is well below the thresholds for sputtering and creating displacement damage, as well as low enough to prevent the formation of a deuterium-rich near-surface layer [94]. The incident ion flux is weakly dependent on the bias and is close to 10^{20} D/m^{2}s. By using the same settings in all experiments it is assumed that the ion flux stays practically constant and is equal to the value reported by Manhard et al. [100]. During the exposure the samples are also bombarded by neutral deuterium atoms with thermal energies, this flux is about 10–100 times higher than the incident ion flux. However, their contributions are neglected and flux refers to the ion flux only.

A metal shutter is used to block the plasma beam from hitting the sample holder. Prior to the exposures, the discharge is operated for 1 h with a closed shutter in order to reach stable plasma conditions and to remove adsorbed impurities from the plasma-wetted surfaces.

Up to 8 samples can be clamped to a tungsten-coated copper target holder by using molybdenum screws. All the specimens on the holder are placed at the same radial distance from the centre ensuring identical exposure conditions. A radial scan of the ion saturation current using a Langmuir probe biased to −50 V located 3 cm above the holder indicated that the ion flux varies nearly linearly across the sample length of 10 mm by about 22 % from the innermost to the outermost edge. The holder temperature is monitored using a K-type thermocouple attached to it from the back side and is feedback-controlled by using an open-circuit thermostat with silicone oil. In addition, an infrared (IR) camera is used to monitor the temperature evolution as well as its lateral homogeneity across the samples during the experiments. The holder is typically pre-heated to the desired temperature for several hours before the plasma exposure. After finishing the plasma exposure, the samples are cooled down in vacuum to room temperature within 30 min.

4.1.2 Pilot-PSI

While PlaQ provides a relatively low ion flux allowing to minimise the production of defects during a plasma exposure (e.g., blister-like structures), it does not allow to study the influence of the defects created by extremely high incident particle fluxes (up to 10^{24} D/m^{2}s) expected in the divertor of ITER nor to achieve ITER-relevant fluences ($> 10^{26}$ D/m^2). In the present work the exposures of samples to a high-flux deuterium plasma were carried out at the linear plasma device Pilot-PSI (DIFFER, The Netherlands) [101]. A schematic drawing of the setup is shown in Fig. 4.2.

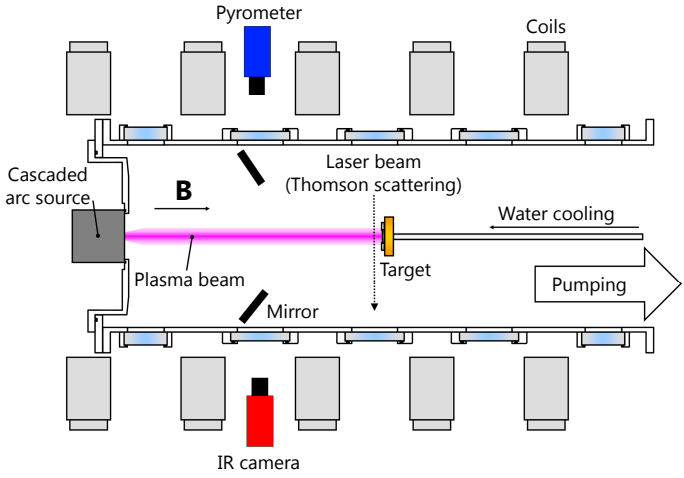

Fig. 4.2: A schematic drawing of the Pilot-PSI linear plasma device.

The base pressure in the vacuum chamber obtained by two mechanical booster pumps in series with a rotary vane pump is about 10^{-1} Pa and increases to

about 1 Pa during plasma operation. The plasma is generated by a cascaded arc source with a discharge current in the range of 150–200 A and a D_2 gas flow in the rage of 1.4–3 slm (1 standard litre per minute is 4.48×10^{20} particles/s). The generated plasma is transported from the source to the target by applying an axial magnetic field in the range of 0.2–1.6 T created by oil-cooled Bitter coils. In the present experiments, the magnetic field strength was 0.2 T, which allowed performing steady-state plasma exposures. In the case of higher magnetic fields, the setup can operate only in a pulsed mode where the duration of the pulse is limited by heating of the coils.

The plasma beam consists predominantly of D^+ ions due to its low temperature and high density [102]. Electron density n_e and temperature T_e profiles of the plasma are measured by Thomson scattering at a distance of about 2 cm from the target [103]. The measurements are typically carried out a few times during the first 30 min of the exposure; at larger times the stray light level noticeably increases[1], thus making the measurements unreliable. Hence, the last measured values are assumed to stay constant until the end of the exposure. The plasma parameters of the beam have approximately a Gaussian radial distribution with a maximum electron density and temperature (at the used experimental conditions) not exceeding 8×10^{19} m^{-3} and 1 eV, respectively. The ion flux on the target Γ is derived from the Bohm criterion [104]:

$$\Gamma = \frac{1}{2} n_e \sqrt{\frac{k_B(T_e + \gamma T_i)}{m}}, \tag{4.1}$$

where T_i is the ion temperature, which is assumed to be equal to the electron temperature T_e [101], m is the mass of a deuterium ion, and the adiabatic index γ is assumed to be 5/3 (corresponding to an adiabatic flow with isotropic pressure). The calculated radial flux distribution has approximately a Gaussian profile with a full width at half maximum (FWHM) in the range of 15–20 mm (Fig. 4.3). The maximum ion flux in the beam centre varies in the range of $3–5\times10^{23}$ D/m^{2}s in different experiments, but does not change significantly within the duration of a single experiment. The flux profile is integrated over the surface of the sample to yield the average incident flux. The difference between the flux (and, correspondingly, the fluence) in the beam centre and the averaged one over the entire exposed area of the specimen is within 30 %. Later in the text, the values of the incident fluence and the surface temperature in the sample centre will be used.

The target is installed perpendicularly to the plasma beam at the beam centre. It is clamped to a water-cooled copper holder using a mask made of TZM alloy with a diameter of the opening area of 8 mm. In order to maximize the thermal contact, a GRAFOIL flexible graphite interlayer is added between the

1. This presumably happens due to heating of the vacuum vessel during the plasma operation leading to thermal expansion of some metallic parts, which can modify the alignment of the laser by changing the mirror setting. As a result, the laser interacts with the collimation apertures leading to the appearance of the stray light.

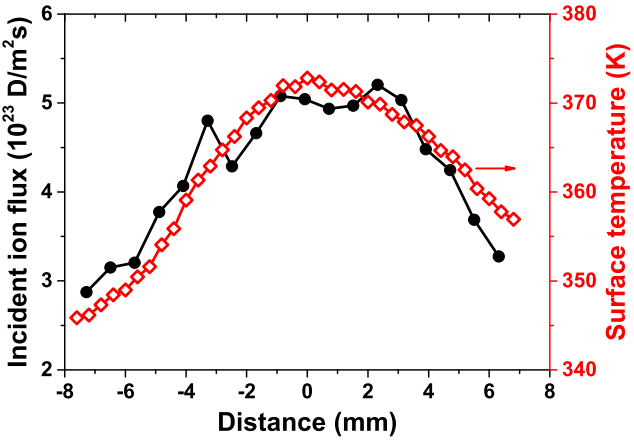

Fig. 4.3: Typical incident ion flux (solid circles) and surface temperature (open diamonds) radial profiles in Pilot-PSI.

sample and the holder. The lateral distribution of the surface temperature of the targets during plasma exposures is determined by IR thermography using a fast camera (FLIR SC7500-MB). The surface temperature is derived from the measured intensity of IR radiation under the following assumptions: 1. all areas of interest have the same known background temperature; 2. the IR background signal does not change during the measurement; 3. the spectral emissivity is independent of the surface temperature. The tungsten spectral emissivity was determined in an independent experiment by matching the surface temperature in the sample centre measured by a multi-wavelength IR pyrometer (FAR associates FMPI) and by the IR camera at temperatures above 800 K. The determined emissivity value of 0.1 was later used for the data evaluation.

The temperature of the sample during plasma exposure is governed by the balance between the heat flux to the target carried by the plasma beam and cooling via thermal conduction. Due to the radial non-uniformity of the plasma beam, the lateral distribution of the surface temperature is also non-homogeneous and follows the ion flux profile (Fig. 4.3). In the present experiments, the exposures were carried out at a surface temperature in the sample centre of about 380 K. The difference in the temperature between the centre of the sample and the edges was typically within 30 K. The variation of the sample temperature between different exposures, as well as the difference between the temperatures at the beginning and at the end of exposures was within 10 K. The target reached an equilibrium temperature within 10 s after switching on magnetic field and bias. After switching off magnetic field and bias, the target cooled down to room temperature also within 10 s.

The target holder can be biased with respect to the vessel walls. In the present experiments, a bias of −40 V was applied to the targets during the plasma exposures. Although the plasma potential was not measured, due to the very low electron temperature of the plasma (≤ 1 eV) the plasma potential should be

only a few eV [104]. Consequently, the mean incident energy of the deuterium ions is close to 40 eV.

4.2 Radiation damage creation

4.2.1 MEDION

The experiments devoted to *in situ* investigations of the deuterium interaction with radiation defects in tungsten were carried out in the MEDION ion-beam facility (MEPhI, Russia) [68]. A scheme of the setup is shown in Fig. 4.4. An ion beam is extracted from a duoplasmatron ion source, passes through an einzel lens, is mass-separated in a 60° deflection magnet, and then directed onto a sample. Different ions (D^+, D_2^+, D_3^+) can be used for performing irradiations, and the maximum acceleration voltage at the exit of the ion source is limited to 10 kV. In order to reduce the spatial beam flux variations, the beam is passed through a 3 mm aperture at the entrance of the target chamber. Typical ion fluxes on the sample are in the range of 3–6 $\times$ 10^{16} D/m^{2}s. The measurement of the ion current on the sample during an irradiation is performed without suppression of secondary electron emission. The secondary emission yield was determined to be around 0.5 (at an ion energy of 3.33 keV/D) in an independent experiment by comparing the measured ion current on a sample and on a Faraday cup with a negatively biased electron-suppressor lid. The measured ion fluences were then corrected by taking into account this value assuming that it was the same in all experiments and is independent of ion energy.

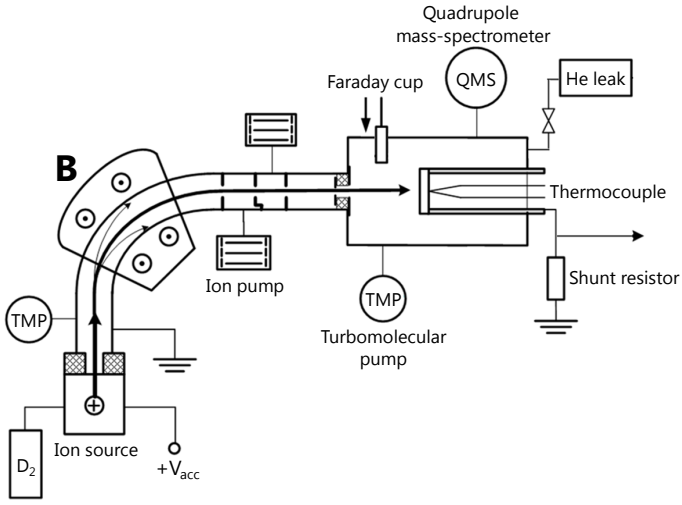

Fig. 4.4: A schematic drawing of the MEDION setup.

The target chamber is separated from the ion source by several differential pumping stages and has a base pressure below 5 $\times$ 10^{-7} Pa (the gauge limit)

after two days of baking obtained by a turbomolecular pump in series with a diaphragm pump. The main background vacuum component is mass 2 (H_2) and the contributions of masses 18 (H_2O) and 28 (CO) are more than one order of magnitude smaller. During ion implantation the pressure increases to about 10^{-6} Pa mainly due to the leaking of D_2 gas from the ion source. A quadrupole mass-spectrometer (QMS) Pfeiffer Prisma QMS 200 operating with a secondary electron multiplier detector is installed in the target chamber allowing *in situ* TDS analyses. The QMS is not located in the line-of-sight of the sample, thus, only the rise of the partial pressures of monitored gases (ten masses) is measured by the QMS during TDS. The QMS signal for mass 4 (D_2 and He) is calibrated by using a helium leak. The relative QMS sensitivities for D_2 and He, as well as for masses 3 (HD) and 4 were determined in an independent experiment using a calibration system described in [105].

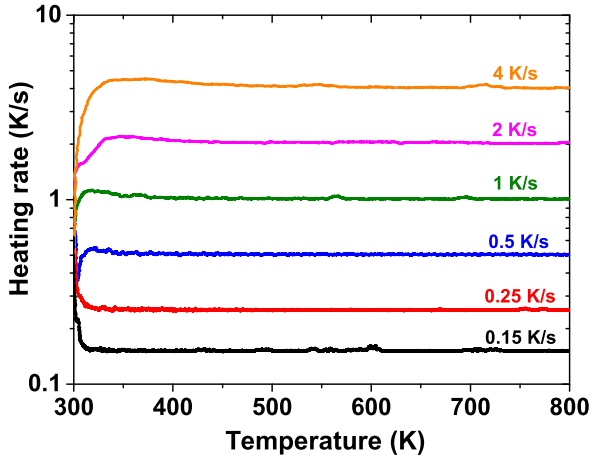

Fig. 4.5: The experimental heating ramps at the MEDION setup.

The sample in the shape of a thin strip (15×50 mm^2) is mounted on two water-cooled electrical feedthroughs and can be resistively heated by direct current up to 1800 K. Only a small central part (3 mm in diameter) of the sample is subjected to irradiation to minimise the influence of the non-uniformity of the temperature over the sample surface during TDS. Irradiations are performed at normal ion incidence, and the sample temperature is close to room temperature. The sample temperature near the beam strike area is measured by a spot-welded tungsten-rhenium thermocouple. The error in the temperature measurement induced by the current passing through the sample is below 1 K at the temperatures of interest (< 900 K). The linearity of the sample heating during TDS is controlled by a loop feedback system based on a proportional-integral-derivative controller. All used heating ramps showed a good linearity (Fig. 4.5): even at the highest heating rate of 4 K/s the heating is nonlinear only up to 400 K, i.e., far from the peaks of interest, as will be shown in

chapter 6. At temperatures above 400 K the deviation of actual heating rates from the programmed ones is within 3 %.

The time interval between irradiation and TDS analysis was fixed to 3 h in the present experiments. This time was sufficient for the signals of all monitored masses to return to their initial values before the irradiation. Diffusion-trapping simulations using the TMAP7 code [50] indicate that this time is also large enough to release a substantial part of solute deuterium from the sample, at least in the case of a clean surface. During the TDS measurements, an increase of the background signals of deuterium-containing molecules is not observed even at high temperatures. Hence, only the baseline levels of the corresponding signals were subtracted from the raw data. Because of the low amount of trapped deuterium in the present experiments and the inevitable noise of the secondary electron multiplier detector of QMS, the measured signals exhibited noise (especially at low heating rates), which complicated the determination of the peak position. Therefore, all the raw data were smoothed using a Savitzky-Golay filter implemented in the OriginPro software, as illustrated in Fig. 4.6, which allowed to eliminate the noise while not affecting the spectrum shape.

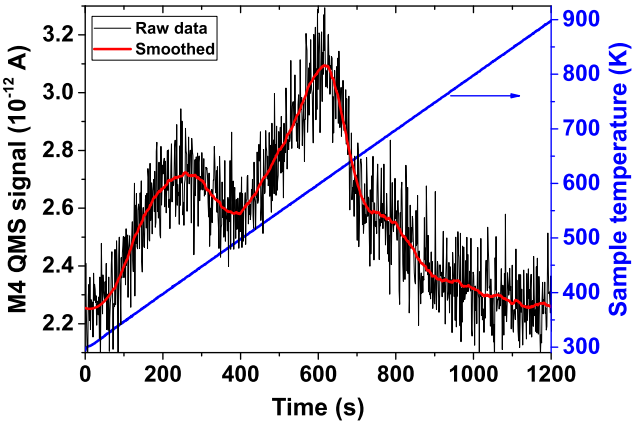

Fig. 4.6: A comparison of the raw QMS signal of mass 4 during the TDS measurement in the MEDION setup with the smoothed one using a Savitzky-Golay filter. The TDS heating rate is 0.5 K/s.

4.2.2 Tandem accelerator

Damaging of samples by protons and tungsten ions was carried out in the implantation chamber connected to the 3 MV tandem accelerator (IPP, Garching) [97]. The residual pressure below 10^{-5} Pa in the vacuum chamber is obtained by a turbomolecular pump in series with a rotary vane pump. The samples are clamped to a water-cooled copper holder by using molybdenum masks with an opening area of 8×8 mm^2 (Fig. 4.7). In order to obtain a laterally homogeneous damaged area, the incident beam (2 mm FWHM) is

scanned over the whole sample surface. The incident ion flux is controlled during damaging by four small-diameter Faraday cups located at the corners of a water-cooled copper diaphragm placed in front of the sample holder. The accuracy of the ion current measurement is better than 10 %. In the present experiments the damaging was carried out at normal ion incidence and ion flux was around 10^{16} particles/m^{2}s. The temperature of the sample holder is measured by an attached K-type thermocouple and is kept close to 290 K during damaging.

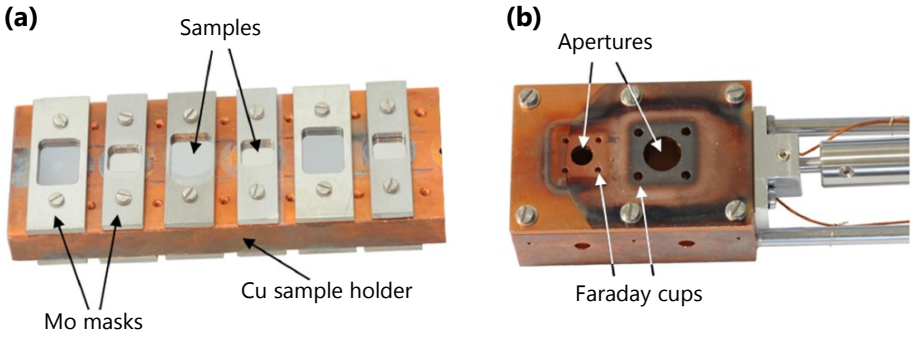

Fig. 4.7: (a) The sample holder for damaging used at the tandem accelerator; (b) apertures together with the corner Faraday cups [97].

4.3 Analysis techniques

4.3.1 Nuclear reaction analysis

Nuclear reaction analysis (NRA) is a method allowing quantitative determination of concentration profiles of light elements in solids [106]. The principle of the method is that a sample containing the element of interest is bombarded with light ions with energies in the MeV range; nuclear reactions between the atoms under investigation and the incident ions occur, and the reaction products are detected; by measuring the energy spectra of the reaction products and knowing the reaction cross-section, the concentration profile of the element of interest can be reconstructed. NRA is a non-destructive technique since only a negligible amount of particles is lost due to transmutations in nuclear reactions. However, the analysing MeV ion beam creates radiation defects in the material, which can be a nuisance in some cases [107].

The most suitable reaction for deuterium depth profiling is D(^{3}He, p)α due to the high energy release of 18.4 MeV, resulting in proton energies in the range 11–14 MeV [108]. This high proton energy well above the incident energy allows to cut off backscattered primary particles by a stopper foil. The cross-section of the reaction has a maximum at about 620 keV with a FWHM of 740 keV. Fig. 4.8 shows the measured differential cross-section at a laboratory scattering

angle of 135° as a function of the energy of the ^{3}He ions. It should be noted that at this scattering angle the reaction has inverse kinematics, i.e., the energy of the protons increases if the energy of the ^{3}He ions decreases [109].

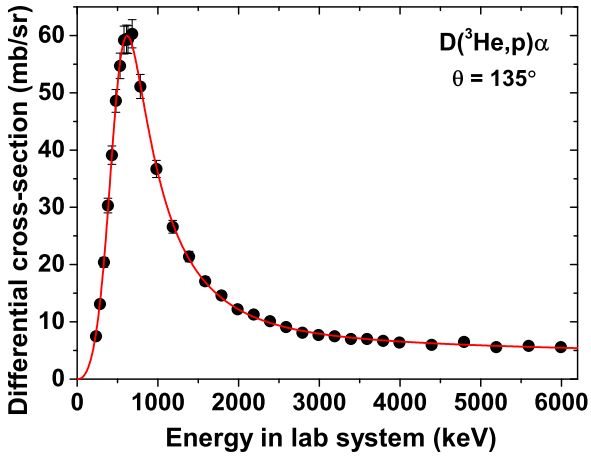

Fig. 4.8: Differential cross-section of the D(^{3}He, p)α reaction at a laboratory scattering angle of 135° from Wielunska et al. [110]. The solid line represents the fit included in the SIMNRA programme.

A proton energy spectrum at a single incident ^{3}He energy contains information about the deuterium depth profile within the range of the ions. However, the depth resolution of the method depends on the ^{3}He ion energy and its optimum value is achieved only close to the end of the ^{3}He range. Hence, a reasonable depth resolution throughout the whole analysed depth can be achieved only by combining measurements at different incident energies [108]. The achievable depth resolution for deuterium in tungsten is mainly determined by multiple small-angle scattering of incident ^{3}He ions and varies from 100 nm near the surface to 1–2 μm at large depths. The high stopping power of tungsten limits the analysable depth to about 7 μm for 4.5 MeV ^{3}He.

All the NRA measurements described in this thesis were carried out *ex situ* in the RKS scattering chamber connected to the 3 MV tandem accelerator (IPP, Garching). Seven different ^{3}He energies varying from 0.5 MeV to 4.5 MeV are used. The energy spectra of protons from the D(^{3}He, p)α reaction are measured using a solid-state detector at a laboratory scattering angle of 135°. The detector is equipped with an aperture with a parabolic slit reducing its solid angle to 77.5 msr, and a 50 μm thick Mylar foil coated with a 50 nm thick gold film is installed in front of the detector to block backscattered ^{3}He ions. The energy calibration of the detector is performed at 2.4 MeV ^{3}He ion energy using the peaks from the D(^{3}He, p)α and ^{12}C(^{3}He, p$_{0,1}$)^{14}N reactions (either from one of the samples or from a thin a:C-D layer on silicon). The accumulated charge of ^{3}He ions for one energy is typically in the range of

10–50 μC (in order to obtain a reasonable counting statistics) resulting in a minimal detectable deuterium concentration of a few times 10^{-6} at. fr.

The deuterium concentration within the near-surface layer in the specimens is determined by means of the D(^{3}He, α)p reaction at ^{3}He energies of 0.5 MeV and 0.69 MeV [111]. The energy spectra of α-particles are measured using a solid-state detector at a laboratory scattering angle of 102°. The detector is equipped with an aperture with a rectangular slit reducing its solid angle to 7.65 msr, and a 3.5 μm thick Mylar foil is installed in front of the detector to block backscattered ^{3}He ions. The energy calibration of the detector is performed using the peaks of α-particles at 0.5 MeV and 0.69 MeV ^{3}He ion energies. Such a shallow detection angle of emitted α-particles together with their high stopping power in tungsten allows achieving a good depth resolution (about 25 nm near the surface).

The measured energy spectra of protons and alphas represent a convolution of the depth distribution of the retained deuterium, the energy dependence of the reaction cross-section, and the energy straggling of incident and emitted particles. Reconstruction of deuterium depth distributions requires simultaneous fitting of simulated spectra to the experimental ones for all incident ^{3}He energies. In the present work, the automatic fitting procedure based on the Bayesian statistics implemented in the NRADC programme [112] is used. The SIMNRA 7 programme [113] is used by NRADC for simulation of the proton and alpha spectra. The cross-section data are taken from Wielunska et al. [110]. Although in reality a deuterium concentration profile is a continuous function, due to the limited depth resolution of NRA only average values of concentration in a layer can be derived. Hence, in NRADC the sample is discretised into layers with a constant deuterium concentration which thicknesses are restricted to be above the achievable depth resolution calculated using the RESOLNRA programme [114]. The NRADC optimises the number (solutions with a large number of layers are marginalized), thicknesses, and deuterium concentrations in the layers by using a Markov-Chain Monte Carlo method. As a result, a depth profile with the maximum likelihood and confidence intervals is produced. The calculations in NRADC are performed with the assumption of low concentration of deuterium in the material, i.e., the stopping power depends only on the target material. In all cases, a good agreement between the experimental data and the simulations was obtained ($\chi^2/n < 1$, where n is the number of channels). As an example, Fig. 4.9 shows measured proton and alpha spectra obtained at various ^{3}He ion energies together with the corresponding fits obtained by NRADC. Fig. 4.10 shows the respective most probable deuterium depth profile. In SIMNRA and NRADC the thicknesses of layers are expressed in units of areal density (10^{15} atoms/cm^2) and can be converted into conventional length units by using the nominal tungsten density of 19.25 g/cm^3, i.e., 10^{15} atoms/cm^2 = 0.159 nm.

The total amount of retained deuterium within the NRA probing range is determined by integrating the concentration profile over the depth. The lateral

resolution of the measurements in the RKS setup is limited by the beam spot size of about 1×1 mm^2.

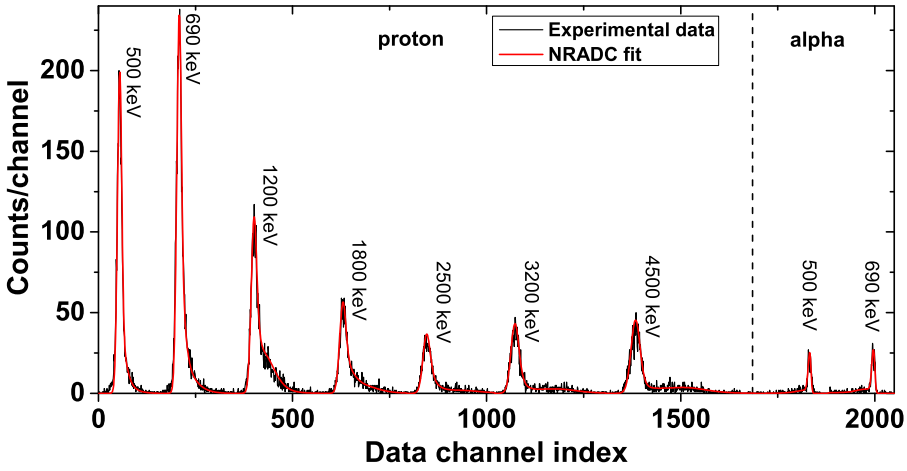

Fig. 4.9: Example of a comparison of experimental proton and alpha spectra at various ^{3}He ion energies with the fitted ones using NRADC. Note the different accumulated charges of ^{3}He ions at various incident energies: 20 μC at 500–2500 keV, 30 μC at 3200 keV, and 40 μC at 4500 keV.

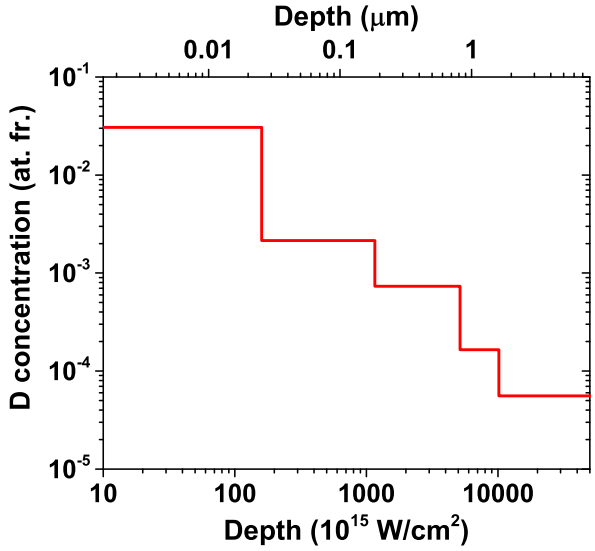

Fig. 4.10: The most probable deuterium depth profile corresponding to the NRA data shown in Fig. 4.9 obtained using NRADC.

4.3.2 Thermal desorption spectroscopy

Thermal desorption spectroscopy (TDS) (sometimes referred to as temperature programmed desorption (TPD)) is a method for studying the behaviour of gaseous species in solids that can provide information on binding energies, the desorption mechanisms, and the number of retained particles [115, 116]. The principle of the method is the following: A sample containing gaseous atoms (adsorbed on the surface and/or retained in the bulk in interstitial and trapping sites) is heated in ultra-high vacuum (UHV). With increasing temperature the probability for the atoms to receive sufficient energy from the lattice in order to escape from their location site increases. After release from a bulk site, the atoms diffuse in the lattice, can be retrapped at empty trapping sites on their way, and, eventually, reach one of the sample surfaces. After reaching the surface they recombine into molecules (in the case of molecular gases) and finally desorb into vacuum. The desorbing particles are registered with a mass-spectrometer. Typically the material is heated to such temperatures such that all retained atoms are released, therefore, TDS is a destructive method. The temperature ramp during TDS can be arbitrary, but for easier analysis linear heating ramps are usually utilised. In that case the sample temperature evolution with time is described as $T(t) = T_0 + \beta t$, where T_0 is the initial sample temperature and $\beta = \mathrm{d}T/\mathrm{d}t$ is the heating rate.

The pressure $p(t)$ in the vacuum vessel surrounding the sample is determined by the flux of the desorbing particles $J(t)$ [particles/(m^{2}s)], the leak rate L [particles/s], and the pumping speed S [litres/s]:

$$KV\frac{\mathrm{d}p(t)}{\mathrm{d}t} = AJ(t) + L - KSp(t), \tag{4.2}$$

where $K = 3.27 \times 10^{19}$ particles/(litres $\cdot$ torr) is a conversion factor for the particle flux units from [litres $\cdot$ torr/s] to [particles/s], V is the volume of the vacuum chamber, and A is the sample area. It is assumed that the released gases are not readsorbed on the sample surface and the vessel walls during the measurements. The leak rate is assumed to be constant during the measurements and determines the background pressure p_0 in the chamber according to $p_0 = L/(KS)$. In most cases, the parameters of the vacuum system (vessel volume and pumping speed) and the heating rate (which influences the flux of desorbing particles) are adjusted in such a way that the pressure rise during TDS is small ($V\mathrm{d}p/\mathrm{d}t \ll Sp$). In this case, the desorbing flux is proportional to the pressure rise in the vessel:

$$J(t) = \frac{KS}{A}(p(t) - p_0). \tag{4.3}$$

This regime is usually referred to as the dynamic mode of TDS measurements. In most cases the mass-spectrometer is not located in the line-of-sight of the sample, thus, only the rise of the partial pressures of monitored gases is measured. For the quantification of the amount of the released gas, a calibration

of the mass-spectrometer signal is required. This can be done with the help of several techniques [105, 117], for example, by using a calibrated gas leak. When high sensitivity is required (i.e., when the amount of retained particles is low), the mass-spectrometer can be placed in line-of-sight to the sample and is differentially pumped, which, in turn, makes the absolute calibration of the mass-spectrometer signals more difficult [72, 118].

The measured desorption flux J versus time (or temperature) often shows several peaks, which typically correspond to the release of retained particles from various binding sites (on the surface and in the bulk), thus, the resulting $J(T)$ curve is often referred to as a "thermal desorption spectrum". However, the interpretation of the types of sites in the material responsible for particular peaks in TDS spectra is not straightforward. Often this is done based on intuitive considerations, thus, many inconsistencies exist in literature. Integration of the TDS spectrum versus time yields the total amount of retained particles in the sample.

Despite the simplicity of the method, quantitative analysis of TDS spectra is often complicated. Typical issues are the following: resolution of molecules with close masses, accurate calibration of the mass-spectrometer and its linearity with pressure, the effects of finite pumping speed, the formation of new molecules on the walls of the vacuum chamber and in the mass-spectrometer, non-uniformity of sample heating, gas release from the surrounding surfaces, etc. In the case of experiments with deuterium, it has to be kept in mind that it can be released not only in the form of D_2 molecules, but also as HD, HDO, D_2O, CD_4, and other long-chain hydrocarbons. Their contribution can sometimes be significant and depends on many factors, including the number of trapped deuterium atoms, sample annealing history, duration of the sample exposure to air prior to TDS measurements, vacuum conditions in the TDS facility, etc. [119, 120]. The quantification of absolute fluxes of such molecules, especially of heavy water (HDO, D_2O), is challenging, resulting in uncertainties in the determination of total amounts of retained particles.

The *ex situ* TDS measurements described in this thesis were carried out in the TESS installation (IPP, Garching) [121]. A scheme of the setup is shown in Fig. 4.11.

The main chamber of the setup is pumped with two turbomolecular pumps connected in series and backed by a dry scroll pump; a background pressure below 10^{-7} Pa is reached after a few days of baking. The samples are loaded into a quartz tube that can be connected to the main chamber through a gate valve. The tube has a side arm where several specimens can be stored. The tube is pumped via a second gate valve through the load lock with a turbomolecular pump and a dry scroll pump to a pressure below 10^{-4} Pa before it is connected to the main chamber. During pumping the measurement position (i.e., the section of the tube which is heated in the following TDS measurements) is annealed at 1323 K for several hours to reduce background contributions from its walls during the measurements. The side arm is located far from the

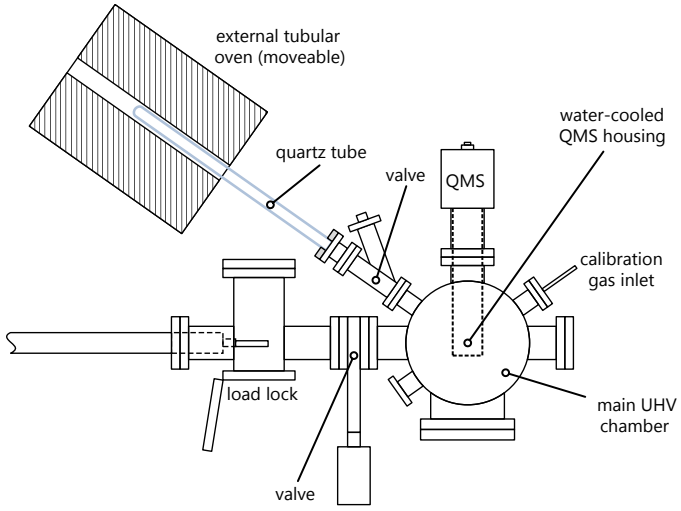

Fig. 4.11: A schematic drawing of the TESS setup [69].

heated area, and, in addition, is cooled by compressed air flow during annealing and TDS measurements. Thus, the temperature of the specimens located in the storage position does not rise noticeably during these procedures. After connecting to the main chamber and a few days of pumping, the background pressure in the tube is about 10^{-6} Pa. For performing the TDS measurement, one specimen is moved to the measurement position with a piece of nickel inside the tube which is manipulated by a magnet outside of the tube. The specimen is then heated by radiation from an external tubular furnace up to a temperature of 1330 K. The release of desorbing species (ten masses) is monitored by a QMS Pfeiffer DMM 422 operating in single ion counting mode. The QMS is located in the main chamber. Prior to performing the measurements, a background run without a sample is performed in order to check the residual background signals. No noticeable increase of the signals of masses 3 (HD), 19 (HDO), and 20 (D_2O) is observed during the background run. The background signal of mass 4 (D_2 and He) increases with increasing oven temperature approximately exponentially to a level of about 70 counts/s (corresponding to a desorption flux around 3×10^{15} D/m^{2}s), which is due to permeation of helium from atmosphere through the quartz tube at high temperatures (Fig. 4.12). Hence, this background was subtracted from the raw mass 4 signal, although in most cases it is considerably lower compared with the deuterium signal. After each experiment, the measurement position is annealed at 1323 K for one hour in order to desorb the species that stuck to the tube walls during the measurement.

During TDS the oven is programmed for a linear temperature ramp of 0.25 K/s and is feedback-controlled with a thermocouple inside. The sample temperature versus the oven temperature is calibrated in independent experiments by a K-type thermocouple spot-welded to the sample. At the beginning of the

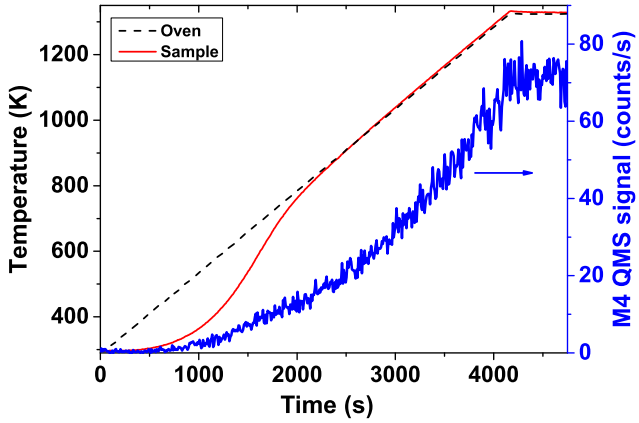

Fig. 4.12: Example of the temperature response of a tungsten sample to a linear oven heating rate (0.25 K/s) in the TESS setup. The increase of the mass 4 signal during a background run without sample is also shown.

temperature ramp, the heating is nonlinear up to about 800 K (Fig. 4.12). The reproducibility of the temperature calibration for different samples of the same type was checked several times and was always within 20 K.

The QMS signal for mass 4 (D_2) is calibrated using a calibrated leak. The relative QMS sensitivities for masses 3 (HD) and 4 are determined by using the procedures described in [117]. In order to roughly estimate the contribution of heavy water, the relative QMS sensitivities of D_2O to D_2 and of HDO to HD are assumed to be the same as that of H_2O to H_2, which are taken from [122]. The total deuterium retention is calculated as the sum of the D_2 and HD contributions. The amount of deuterium released in the form of HDO and D_2O molecules is considered as the upper limit of the error of the total inventory measurement.

4.3.3 Surface imaging

The surface morphology of the samples before and after plasma exposures was investigated in a confocal laser scanning microscope (CLSM) Olympus LEXT OLS4000 and a scanning electron microscope (SEM) FEI HELIOS NanoLab 600 (IPP, Garching). The SEM has a Ga^+ focused ion beam with an energy up to 30 keV which allows *in situ* cross-sectioning and imaging of the specimens. The typically used electron beam energy is 5 keV. The cutting is done under normal Ga^+ incidence; the angle between the Ga^+ beam and the electron beam is 52°, as illustrated schematically in Fig. 4.13. As a result, the cross-sections are imaged at 38° tilt making the vertical scales appear compressed by a factor of 1.27 with respect to the horizontal scales. To minimise the appearance of artefacts during the cross-sectioning, the region of interest is pre-coated *in situ* with a Pt-C layer. In addition, the SEM allows analysing

the elemental composition of a near-surface layer by means of energy-dispersive X-ray spectroscopy (EDX).

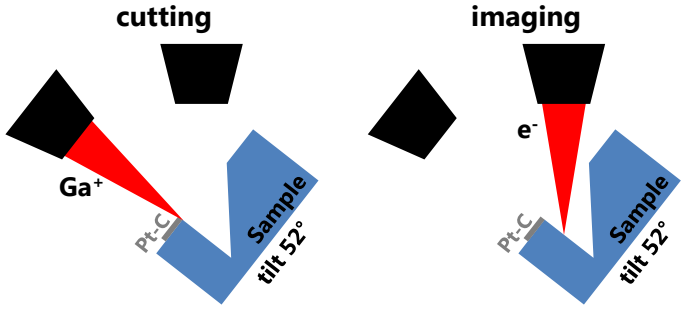

Fig. 4.13: Schematic representation of sample cross-sectioning and imaging at the SEM.

4.3.4 Positron annihilation spectroscopy

Positron annihilation spectroscopy (PAS) is a non-destructive method for detecting the presence of open-volume defects in materials with concentrations down to 10^{-7} at. fr. [123–125]. The principle of the method is the following: When an energetic positron is injected into a metal, it is thermalized within a few picoseconds through inelastic collisions. Then it diffuses in the metal and lives there for a few hundred picoseconds until annihilation with an electron producing two γ-quanta with an energy of about $m_e c^2$ (511 keV) which are emitted into approximately opposite directions. A thermalized positron in the lattice can be represented as a wave packet spreading over many cells. In a defect-free lattice, it can survive in this delocalized state until annihilation, and its mean lifetime is determined by the electron density of the metal. However, since a positron experiences a repulsion from the atomic nuclei, any open-volume defect (vacancy, vacancy cluster or void) appears as a potential energy minimum for the positron, thus, the positron can be trapped there (it forms a localized state). Eventually, the positron will annihilate with an electron of the metal either from the delocalized bulk state or from a localized state at a defect. The reduced electron density at an open-volume defect increases the positron lifetime. The lack of core electrons at a defect results in significant changes in the momentum distribution of the annihilating electrons. Since the positron is thermalized, only the momentum of the annihilating electron causes a deviation θ from the 180° angle between the two 511 keV γ-quanta and creates a Doppler shift in their energy ΔE. Hence, these γ-quanta carry information about the environment of the annihilating positron.

There are two widely used PAS techniques based either on the positron lifetime detection or on the measurement of the γ-ray Doppler broadening, as illustrated schematically in Fig. 4.14.

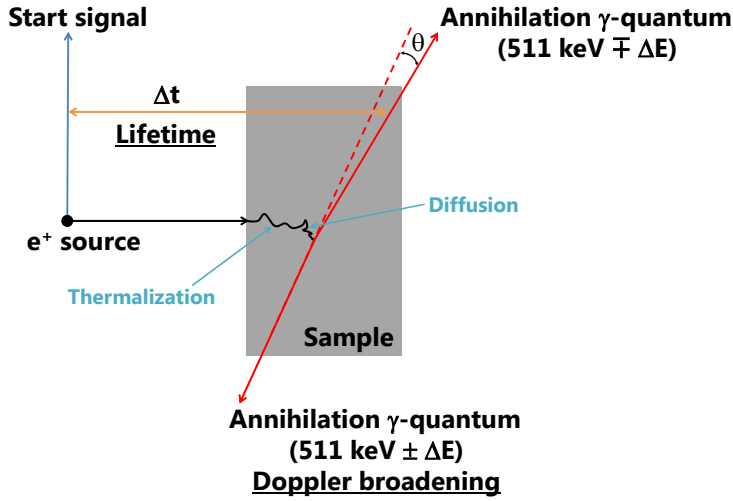

Fig. 4.14: Schematic illustration of positron annihilation showing the basis for the two PAS techniques: positron lifetime and γ-ray Doppler broadening.

In positron annihilation lifetime spectroscopy (PALS) the time interval between the injection of a positron into a sample and its annihilation is measured. Since annihilation is a stochastic process, the positron lifetime has a statistical distribution, which is called the lifetime spectrum $Z(t)$. It can be described by a sum of exponential decays convoluted with an instrumental time resolution function $R(t)$ overlaid on a constant background B:

$$Z(t) = R(t) * \sum_{i=1}^{N+1} \frac{I_i}{\tau_i} \exp\left(-\frac{t}{\tau_i}\right) + B, \tag{4.4}$$

where I_i and τ_i refer to the relative intensity and the positron lifetime in a type $i-1$ defect, respectively, and N is the number of open-volume defect types in the material; I_1 and τ_1 correspond to the annihilation from the delocalized bulk state ($\sum_i I_i = 1$). The average positron lifetime is defined as $\tau_{av} = \sum_i I_i \tau_i$. Since the positron lifetime is related to the local electron density at the annihilation site, the lifetimes τ_i of the components associated to defects reflect the corresponding sizes of open volumes and the species trapped by the defects (e.g., hydrogen atoms). For example, the calculated lifetimes for positrons trapped in vacancy clusters in tungsten by Troev et al. [126] exhibit a strong size dependence for clusters containing up to 30 vacancies and then tend to saturate for larger clusters (Fig. 4.15).

Conventional PALS is performed by using a β^+ radioactive source, such as ^{22}Na. Since the positrons emitted by a radioactive source have a broad energy distribution up to several hundreds of keV, this method allows only the investigation of defects in the bulk[2]. For defect investigations in the subsurface region,

2. For a ^{22}Na source, the maximum positron energy is 0.545 MeV and 99 % of positrons annihilate within the first 62 μm in tungsten.

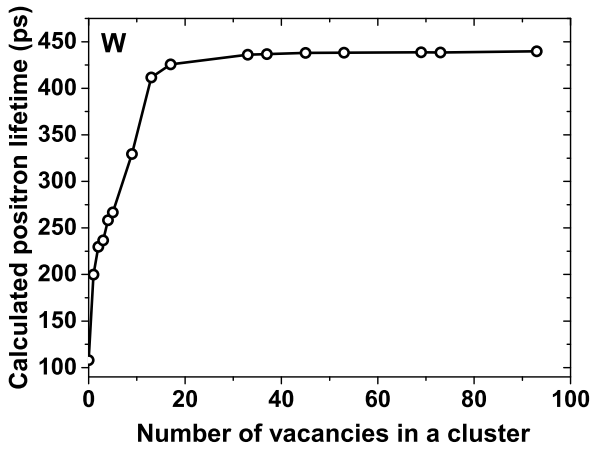

Fig. 4.15: Calculated positron lifetime in tungsten as a function of the number of vacancies in a cluster [126].

pulsed monoenergetic positron beams of variable energy are used. By varying the positron implantation energy E the mean positron projected implantation range R_p can be varied to different depths (up to a few μm), allowing the investigation of defect distributions. The implantation profile $\varphi(x, E)$ can be described by a Makhovian function approximated by the following scaling law:

$$\varphi(x, E) = \frac{\pi x}{2{R_p}^2} \exp\left(-\frac{\pi x^2}{4{R_p}^2}\right), \tag{4.5}$$

where the mean implantation depth is approximated as $R_p = (40/\rho)E^{1.6}$ [nm] and depends only on the positron energy E [keV] and the density of the metal ρ [g/cm^3]. Fig. 4.16 shows positron implantation profiles in tungsten at various incident energies calculated using Eq. 4.5.

For PALS with a monoenergetic positron beam, the lifetime spectrum $Z = Z(E, t)$ is influenced by the positron implantation profile and by the depth distribution of the defects. In addition, for positrons implanted at depths smaller than the typical positron diffusion length (i.e., the average distance that thermalized positrons can travel before annihilation and is around 100 nm for well-annealed crystals [123]) their back diffusion to the surface must be taken into account. This situation is described by the time-dependent diffusion-trapping equations for positrons [127]. The presence of open-volume defects decreases the positron diffusion length. At high defect concentrations, the diffusion length can become much smaller than the mean implantation depth, therefore, positron back diffusion to the surface can be neglected. In addition, if the defect distribution is homogeneous, their concentrations can be directly derived from the measured relative intensities I_i and lifetimes τ_i by using the standard trapping model described in appendix B. This requires the knowledge of the positron trapping coefficients in specific defect types.

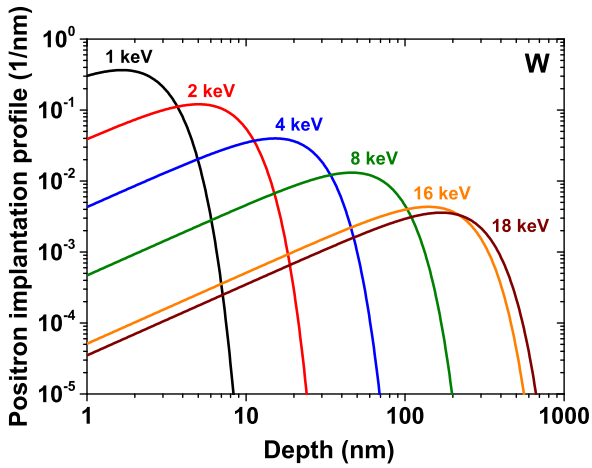

Fig. 4.16: Calculated positron implantation profiles in tungsten at various incident energies.

In the present work the samples were studied with the pulsed low-energy positron beam system (PLEPS) [128, 129] located at the high-intensity positron beam source NEPOMUC (NEutron-induced POsitron source MUniCh) [130] at the research reactor FRM-II in Garching. At NEPOMUC, high-energy γ-quanta are first produced by capture of thermal neutrons in ^{113}Cd. The γ-quanta are converted into electron-positron pairs and further moderated in a set of platinum foils. The primary positron beam is extracted from the source and is guided in a magnetic field. To enhance the beam brightness (i.e., reduce its diameter and divergence), the beam is further remoderated by guiding it on a tungsten (100) single crystal, which has a negative work function for positrons, resulting in the fact that positrons with an energy of a few eV can be reemitted from it.

The scheme of the PLEPS setup is shown in Fig. 4.17. The remoderated positrons first pass a high-pass energy filter, then the pulsed beam (150 ps FWHM, frequency 50 MHz) with high intensity and a low background is formed with the help of a prebuncher, a chopper, and a buncher. Afterwards, the positrons pass through a drift tube (in order to keep the transit time of the pulse from the buncher exit to the target constant for all implantation energies) and are accelerated to the desired energy in the range of 0.1–18 keV. Then the positrons pass a Wien filter used to suppress positrons reflected back from the sample. Finally, positrons pass through a field-free Faraday cage and are implanted into the sample. The annihilation γ-quanta are detected with a photomultiplier coupled to a BaF_2 scintillator mounted behind the sample. The time between the annihilation and the following pulse (provided by an external clock signal) is measured and a lifetime spectrum is collected. It must be mentioned that the beam intensity at NEPOMUC is low enough to fulfil the essential requirement of having only one positron at the time in a sample.

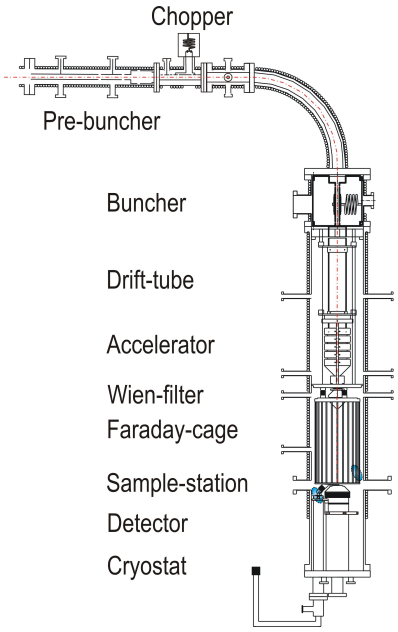

Fig. 4.17: A schematic drawing of the PLEPS setup [129].

In the present experiments, 16 keV and 18 keV positron implantation energies were used corresponding to mean implantation depths of 175 nm and 210 nm, respectively. The total number of events collected in each spectrum is 4×10^6 to ensure a good statistics. The instrument function, which is described by a sum of shifted Gaussian functions, is determined with a p-type SiC reference sample with known bulk and surface lifetimes. The overall (detector and pulsing system) time resolution (FWHM) is 230–250 ps, the count rate is up to 10^4 counts/s, and the beam diameter is smaller than 1 mm.

The lifetime spectra are analysed using the POSWIN programme (a modified version of POSITRONFIT software [131]) developed at Bundeswehr University Munich which utilizes the iterative least-squares fitting of a model function described by Eq. 4.4 to a measured lifetime spectrum. All measured spectra were decomposed with maximum four lifetime components to obtain good variance with $\chi_r^2 = \chi^2/\nu < 1.6$, where $\nu = n - k$ is the number of degrees of freedom, n is the number of data points, and k is the number of free parameters (i.e., lifetimes and relative intensities). As an example, Fig. 4.18 shows a measured spectrum of a tungsten (100) single crystal damaged by 200 keV protons to the fluence of 1×10^{20} p/m^2 at 18 keV positron implantation energy together with the fit and the corresponding lifetime components. The residuals of the fit shown in the lower panel fluctuate around zero, indicating that the data are correctly described by the model. It can be noted that the left wing of the spectrum is determined by the shape of the time resolution function of the system (also shown in the graph).

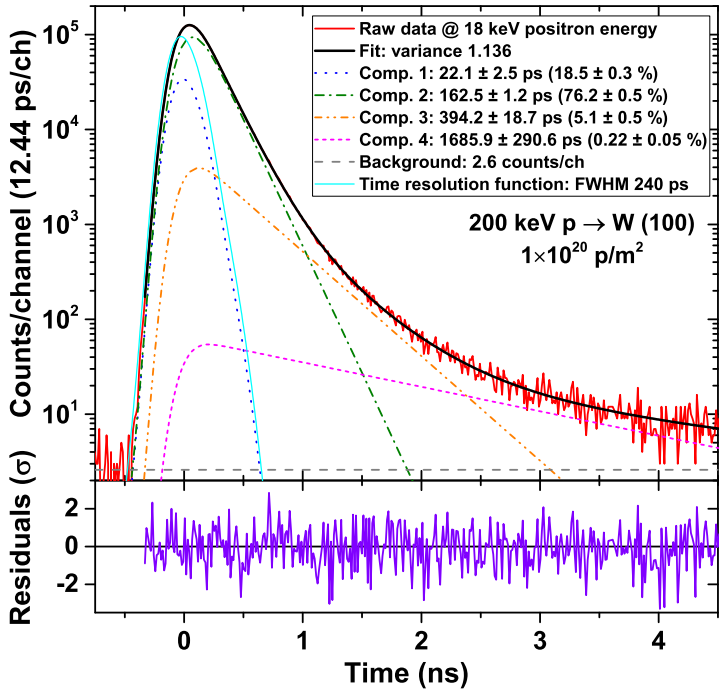

Fig. 4.18: Positron lifetime spectrum of a tungsten (100) single crystal damaged by 200 keV protons to the fluence of 1×10^{20} p/m^2 measured at 18 keV positron implantation energy. Fit of the spectrum, the individual components obtained from the fit, and the instrumental time resolution function are also shown. The lower panel shows the residuals of the fit expressed in units of one standard deviation (σ).

Chapter 5

Deuterium interaction with high-flux plasma-induced defects in tungsten

In ITER the tungsten divertor plates will be subjected to high fluxes (up to 10^{24} H/m^{2}s) of low-energy (up to several tens of eV) hydrogen isotopes, and fluences in excess of 10^{30} H/m^2 will be reached by the end of ITER operation [6]. The stationary surface temperature will strongly vary along the divertor target in the range of 370–1570 K (for the reference deuterium–tritium burning plasma scenario). Such conditions can lead to severe modifications of the tungsten surface, which, in turn, affect the hydrogen isotope retention. The existing data at ITER-relevant fluences ($> 10^{26}$ H/m^2) are scarce and inconsistent (see section 3.6). This chapter[1] presents the results of experiments devoted to investigations of deuterium retention and surface modifications of polycrystalline tungsten after exposure to a low-energy (40 eV/D), high-flux (3–5$\times10^{23}$ D/m^{2}s) deuterium plasma to very high fluences up to 1.2×10^{28} D/m^2.

5.1 Experimental details

Samples made of hot-rolled polycrystalline tungsten discs (20 mm diameter, 1 mm thickness) with a specified purity of 99.97 wt. % produced by Plansee (Austria) were used. The impurity concentrations specified by the supplier are listed in table C.1 in appendix C. The samples were first grinded with a set of

1. The work presented in this chapter is partly already published in the paper: M. Zibrov, M. Balden, T.W. Morgan, M. Mayer, *Deuterium trapping and surface modification of polycrystalline tungsten exposed to a high-flux plasma at high fluences*, Nuclear Fusion **57**, 046004 (2017).

SiC sandpapers with decreasing grit sizes (up to P4000) and then polished to a mirror-like finish with diamond and SiO_2-containing suspensions, as described in [132]. Then they were successively cleaned in an ultrasonic bath with acetone and isopropanol. The samples were annealed at 1173 K in vacuum (around 10^{-3} Pa) for 2 h to release residual hydrogen and relieve stresses produced by manufacturing and polishing. No significant structural modifications in the samples are expected to occur at this temperature, therefore, the samples are considered to be in a stress-relieved state [14]. The tungsten grade used in the present study and the grade extensively studied at IPP in the past [14, 17, 69, 90, 91] were produced by the same method by the same manufacturer and have the same nominal purity; the only difference is that they originate from different manufacturing batches and have different final thicknesses. The two grades have similar microstructures – flattened grains elongated parallel to the surface with a length up to a few μm and a thickness up to 1 μm (perpendicular to the surface).

The samples were exposed to a deuterium plasma in the linear plasma device Pilot-PSI (see section 4.1.2 for the description). Steady-state plasma exposures were carried out to fluences in the range of 5×10^{26}–1.2×10^{28} D/m^2 at a surface temperature in the sample centre of about 380 K. Many experiments at low fluxes were performed at a similar temperature, including those presented in the following chapters, which allows examining the effect of ion flux.

5.2 Surface modifications

Various types of modifications developed on the exposed surfaces (Fig. 5.1). Firstly, dome-shaped structures with nearly elliptic outlines and diameters up to 10 μm are present (e.g., Fig. 5.1(b)). Later in the text, these structures will be referred to as "blisters". These structures are irregularly distributed over the surface and often appear in groups; sometimes they extend over more than one grain. Stepped flat-topped and irregularly-shaped structures with sharp edges and dimensions ranging from 100 nm to several μm are also present (e.g., Fig. 5.1(b), (c)). These structures will be referred to as "protrusions". Compared to blisters, such structures usually appear within a single grain, while their distribution over the surface is also inhomogeneous. Some of the protrusions are present on top of blisters and larger protrusions (Fig. 5.1(b), (e), (h)). The areal density of protrusions is higher compared with the density of blisters, and already at the lowest fluence used (5×10^{26} D/m^2) a noticeable fraction of the surface is covered with protrusions (Fig. 5.1(b)). Despite more than one order of magnitude variation of the fluence, the appearance of blisters and protrusions, namely their number density and average size, barely changes with fluence.

SEM investigations also reveal the presence of a large number of small cracks with lengths up to several hundred nm on the exposed surfaces. The lowest

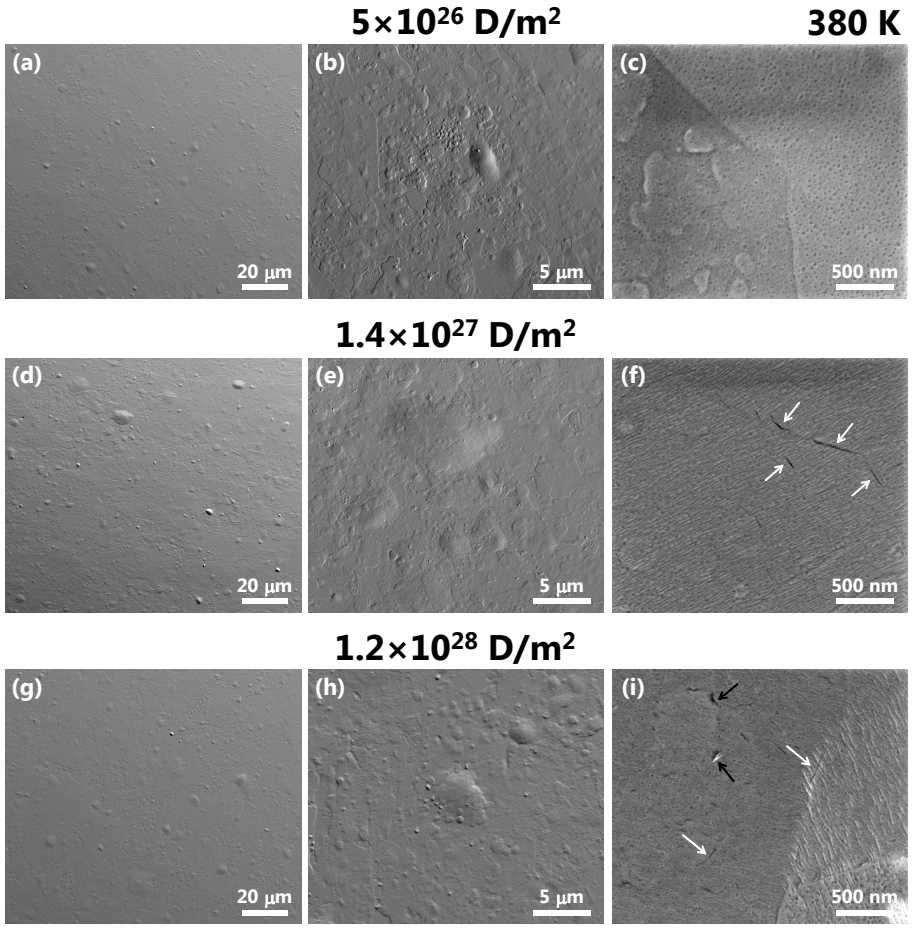

Fig. 5.1: A series of SEM images with different magnifications of polycrystalline tungsten exposed to a high-flux deuterium plasma with an ion energy near 40 eV/D at a temperature of about 380 K to different fluences: (a)–(c) 5×10^{26} D/m^2; (d)–(f) 1.4×10^{27} D/m^2; (g)–(i) 1.2×10^{28} D/m^2. Cracks near edges of protrusions are indicated by the black arrows, whereas cracks on the flat regions of the surface are indicated with white arrows.

fluence at which the cracks can be unambiguously detected is 1.4×10^{27} D/m^2, although their presence on the samples exposed to lower fluences cannot be excluded. Such cracks are observed both on blisters and protrusions (indicated by the black arrows in Fig. 5.1(i)), as well as on relatively flat regions of the surface (indicated by the white arrows in Fig. 5.1(f), (i)). Due to the fact that the cracks are small and can be detected only at high magnifications, it is difficult to judge about the evolution of the number of cracks with fluence.

Fig. 5.2 shows an example of a protrusion with cracks visible on its top and near its edges. Images shown in Fig. 5.2(a) and (b) represent the same region of the sample, but are taken with different SEM modes in order to highlight different features. In order to increase the topography contrast, Fig. 5.2(a) is taken in a

custom mode of the segmented concentric backscatter electron detector (CBS) of SEM, where the difference of the signals from two segments of the detector is used. On the other hand, Fig. 5.2(b) is taken in the backscattered electron (BSE) contrast (also referred to as Z-contrast) mode of the CBS detector (i.e., the sum of the signals from all segments of the detector) in which the cracks are better visible. Cross-sectioning of this protrusion (Fig. 5.2(c)) reveals that its cavity is formed by a crack following a grain boundary (intergranular) running parallel to the surface and located at a depth of about 500 nm. The cracks intersecting the surface are formed both along grain boundaries (see the right arrow) and within single grains (transgranular, marked with a rectangle). Transgranular cracks located at depths typically below 100 nm, which do not intersect the surface, are present as well (marked with ellipses) and can correspond to small protrusions [17, 91], which cannot be well seen due to the developed roughness of the surface.

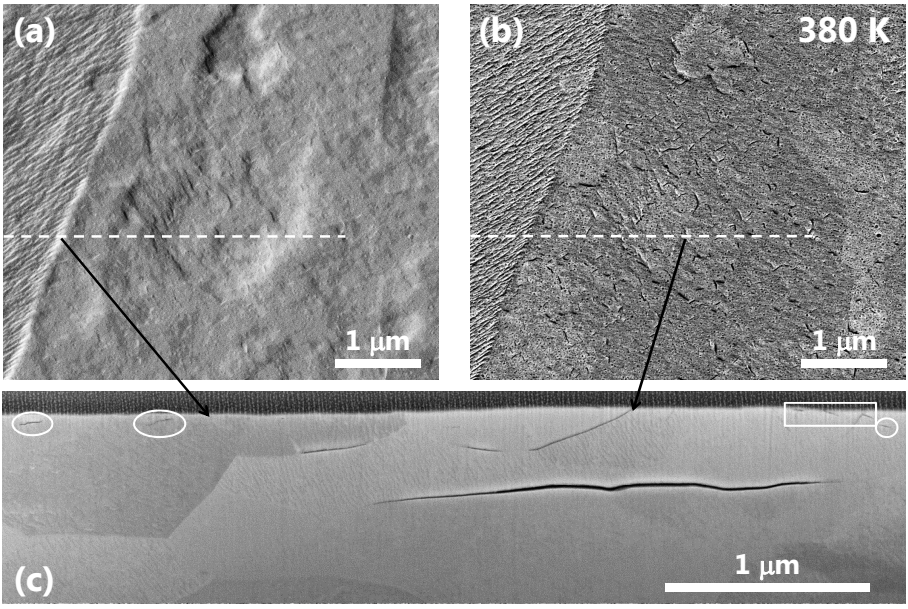

Fig. 5.2: Polycrystalline tungsten exposed to a high-flux deuterium plasma with an ion energy near 40 eV/D at a temperature of about 380 K to a fluence of 1.2×10^{28} D/m^2: A SEM image of a protrusion with a number of cracks visible on its top and near its edges taken (a) in the custom mode of the CBS detector to highlight the topography, (b) in the BSE contrast mode of the CBS detector to highlight the appearance of cracks; (c) a SEM image of a cross-section at the position indicated by the dashed line in (a) and (b). The surface in (c) was protected by a Pt-C layer before cutting. The transgranular cracks that intersect the surface are indicated with a rectangle, whereas the transgranular cracks that do not intersect the surface are indicated with ellipses. The black arrows indicate the same features in (a), (b), and (c).

The fact that cracks are observed on flat regions of the surface, as well as that the cracks observed on top of the protrusion do not reach its cavity

indicate that the appearance of cracks cannot solely be explained by rupture of a blister/protrusion cap due to high internal D_2 gas pressure. It can be hypothesized that such cracks can have the same origin as the transgranular cracks associated with protrusions.

Under the present high-flux plasma exposure conditions both dome-shaped blisters and stepped flat-topped protrusions are formed on hot-rolled tungsten. The protrusions are formed both by intergranular and transgranular cracking. Exposure of the same type of material to a low-flux (10^{20} D/m^{2}s) deuterium plasma at a similar temperature (370 K) results in the formation of only blisters, which cavities are formed by intergranular cracking [69]. However, it was recently demonstrated that even under low-flux exposure conditions both blisters and protrusions (formed by transgranular cracking) can be formed on hot-rolled tungsten, but then the exposure temperature has to be as low as 230 K [91]. It will be also shown in the following chapters that the presence of lattice defects introduced via damaging by protons (chapter 7) and via mechanical deformation (chapter 8) facilitates the formation of protrusions under a low-flux plasma exposure. This indicates that the morphological modifications of the surface depend on several factors, including the ion flux, the sample temperature, and the presence of lattice defects acting as nucleation sites.

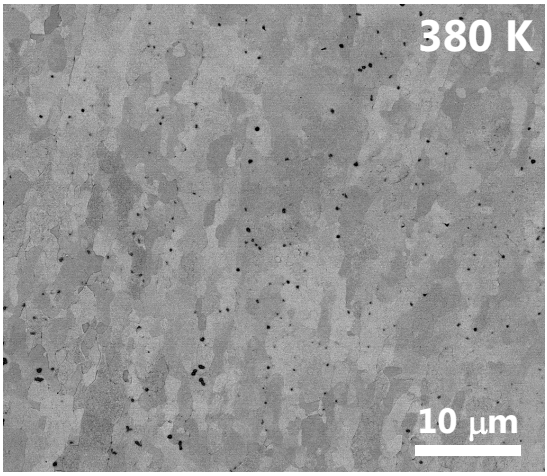

Fig. 5.3: A SEM image (Z-contrast mode) of polycrystalline tungsten exposed to a high-flux deuterium plasma with an ion energy near 40 eV/D at a temperature of about 380 K to a fluence of 1.2×10^{28} D/m^2 illustrating the presence of molybdenum impurities (black particles).

Molybdenum particles with dimensions ranging from a few hundred nm to a few μm were found on some of the exposed samples, as illustrated in Fig. 5.3. However, even in the worst case (only in some regions of some samples), the area occupied by these particles is only within a few percent, consequently, their influence on the deuterium retention should be rather small. These particles

probably originate either from the plasma source (the discharge channel of the cascaded arc source is covered with molybdenum inserts) or from the clamping ring made of TZM (due to parasitic arcing).

5.3 Deuterium retention

Fig. 5.4 shows the measured deuterium depth distributions in the samples exposed to various fluences. The measurements were carried out in the sample centre. A lateral scan with 4.5 MeV ^{3}He ions reveals that the variation of the deuterium content across the plasma-exposed area is within 30 % for all the specimens. The evolution of the depth distributions with fluence is relatively small. In the first 25 nm near the surface the deuterium concentration slightly increases with increasing fluence reaching a saturation value around 3×10^{-2} at. fr.; at larger depths no clear tendencies are visible. A substantial amount (above 80 %) of the detected deuterium is retained within the first 1.5 μm near the surface for all the investigated samples. The comparison with the deuterium depth distributions for hot-rolled tungsten after the exposure to a low-flux (10^{20} D/m^{2}s) deuterium plasma [69] leads to a striking observation: the depth distributions after the high-flux plasma exposure at 380 K strongly differ from those after the low-flux plasma exposure at a similar temperature (370 K); concurrently, they are quite similar to those after the low-flux exposure at 300 K. A correlation between the deuterium depth distributions and the occurrence of cavities of blisters and protrusions can be observed: The thickness of the subsurface region with a high deuterium concentration ($\leq$ 1.5 μm) coincides (within the depth resolution of NRA) with the depth up to which the cavities of blisters and protrusions are located (see Fig. 5.2). A similar correlation was also observed in low-flux experiments by Manhard [69]: At 300 K the blister cavities were located at depths below 1 μm, whereas at 370 K they were located at depths below 4 μm (compare with the depth profiles in Fig. 5.4). Thus, it can be suggested that creation of blisters and protrusions introduces a large number of defects in the subsurface region (e.g., cavities of blisters and protrusions, as well as additional defects generated during creation of blisters and protrusions), which can act as trapping sites for deuterium. The only small variation of the deuterium depth distributions with fluence can be then attributed to the only small variations in number density and size of blisters and protrusions with fluence. The difference between the present deuterium depth distributions and those after the low-flux exposure at 370 K can be explained in terms of differences in the depth where the cavities of blisters and protrusions are located.

Fig. 5.5 shows the fluence dependence of deuterium retention measured by TDS and NRA. Note that in this figure the values of deuterium retention determined by NRA correspond to the local incident fluence in the sample centres, whereas the values of deuterium retention determined by TDS correspond to the incident fluence averaged over the entire plasma-exposed area of

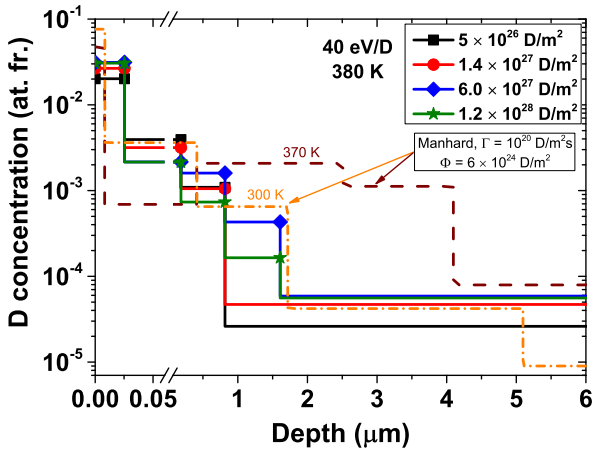

Fig. 5.4: Deuterium concentration profiles in polycrystalline tungsten exposed to a high-flux deuterium plasma with an ion energy near 40 eV/D at a temperature of about 380 K to various fluences. The measurements were carried out in the sample centre. For the comparison, the measurements performed by Manhard [69] for the same type of material (hot-rolled tungsten), exposed to a low-flux deuterium plasma (10^{20} D/m^{2}s) with a mean ion energy of 38 eV/D to the fluence of 6×10^{24} D/m^2 at the temperatures of 300 K and 370 K are shown.

the specimens. Both from the NRA and TDS data it can be concluded that the variation of the deuterium uptake with fluence Φ is certainly slower than $\sqrt{\Phi}$, i.e., not like in the case of diffusion-limited trapping in time-independent traps with a homogeneous depth distribution, and the deuterium inventory itself is quite moderate – below 2×10^{20} D/m^2. NRA gives from two to four times higher retention compared with TDS (if only D_2 and HD contributions are considered). If the estimated contribution of heavy water (mainly HDO) is also taken into account, then the difference becomes smaller[2]. It should be mentioned that the TDS analysis was performed six months after the NRA analysis for most of the specimens; the measurements of the samples exposed to fluences of 1.4×10^{27} D/m^2 and 1.2×10^{28} D/m^2 were carried out nine months after the NRA measurements. The effect of deuterium loss during the storage time even on the time scale of months was reported in literature [120] and can also partially explain the discrepancy between NRA and TDS results, as well as that the samples exposed to fluences of 1.4×10^{27} D/m^2 and 1.2×10^{28} D/m^2 show a smaller deuterium inventory (determined by TDS) compared with the rest of the samples.

The present values of deuterium retention are several times lower than that measured by Manhard [69] for the same type of material exposed to a low-flux plasma at a similar temperature (370 K) to the highest fluence (5×10^{25} D/m^2). This confirms the fact that the deuterium retention in tungsten is flux-dependent. Concurrently, the fluence dependence of the retention in the experiments of

2. The ratio of deuterium released as HDO and D_2O to the deuterium released as D_2 and HD is in the range of 0.6–1.4.

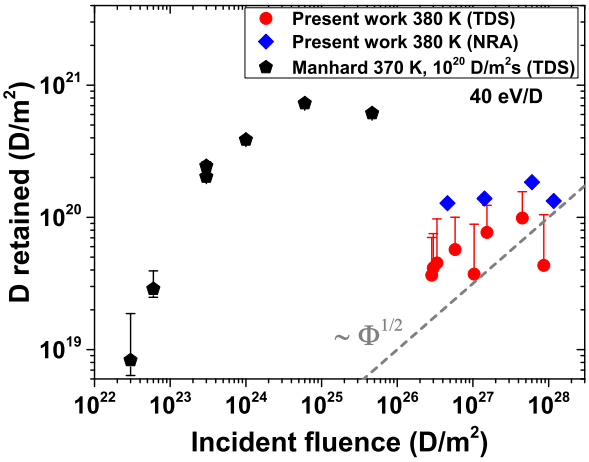

Fig. 5.5: Fluence dependence of deuterium retention in polycrystalline tungsten exposed to a high-flux deuterium plasma with an ion energy near 40 eV/D at a temperature of about 380 K. For the NRA measurements, the fluences in the sample centre are used, whereas for TDS measurements the fluences averaged over the whole exposed area of the sample are given. The data from Manhard [69] for a hot-rolled tungsten exposed to a low-flux deuterium plasma (10^{20} D/m^{2}s) with a mean ion energy of 38 eV/D at 370 K is shown for comparison. The errorbars represent the estimated amount of deuterium released as HDO and D_2O molecules.

Manhard [69] also shows a slow deuterium uptake in the samples at fluences above 10^{24} D/m^2, which correlates with the stagnation of blistering activity. A similar correlation has also been observed after high-flux (10^{24} D/m^{2}s) plasma exposures [18]. Since in the present experiments the blistering pattern, deuterium depth distributions, and total deuterium retention barely change with fluence, it is reasonable to assume that the lowest fluence used (5×10^{26} D/m^2) was already high enough that the concentration of defects produced by the high-flux plasma exposure almost saturated. In addition, as the deuterium depth distributions indicate that more than 80 % of deuterium is retained within the subsurface region ($\leq$ 1.5 μm), it can be concluded that in the present experiments the deuterium retention is dominated by trapping in the defects introduced together with blisters and protrusions.

The hypothesis about the influence of the damage induced by the plasma exposure on the deuterium retention can explain the discrepancy between the present experimental results and those reported by Doerner et al. [21], where the deuterium inventory in the samples almost obeyed the $\sqrt{\Phi}$ dependence in the investigated fluence range (up to 2×10^{28} D/m^2). The experiments by Doerner et al. [21] were carried out at a higher sample temperature (640 K) and lower ion flux (1.6×10^{23} D/m^{2}s) compared with the present experiments, which resulted in the absence of surface modifications. Hence, the amount of the plasma-induced damage must have been much smaller, and the deuterium retention was likely dominated by intrinsic bulk defects in tungsten.

The observed small cracks on the exposed surfaces can also contribute to the slow variation of the deuterium retention with fluence. During a plasma exposure, deuterium atoms diffusing from the implantation region can reach cracks and can recombine into D_2 molecules on their surfaces. This results in an increase of the effective deuterium reemission rate from the samples and a respective reduction of the effective deuterium influx into the bulk of the samples [95].

5.4 Chapter summary

Deuterium retention and surface modification of polycrystalline tungsten have been investigated after exposure to a low-energy, high-flux deuterium plasma at a temperature near 380 K up to very high fluences of about 10^{28} D/m^2. Plasma exposures resulted in severe surface modifications: Appearance of a large number of dome-shaped blisters (up to 10 μm) and stepped flat-topped protrusions (up to several μm). The cavities of blisters were solely formed due to intergranular cracking, whereas the cavities of protrusions were formed both due to intergranular and transgranular cracking. Despite more than one order of magnitude variation of the fluence, the number density and the average size of blisters and protrusions barely changed with fluence. The depth distribution of trapped deuterium, as well as the total deuterium inventory, also demonstrated a rather small evolution with fluence. Most of the deuterium was retained in a subsurface region located at depths smaller than 1.5 μm, which coincides with the depth up to which the cavities of blisters and protrusions were located. It is concluded that in the present experiments the near-surface defects produced by the high-flux plasma exposure (cavities of blisters and protrusions, and defects appearing during their creation) govern the deuterium retention. The number and features of these defects are strongly dependent on the ion flux.

A network of small cracks was observed on the exposed surfaces starting from a fluence of 1.4×10^{27} D/m^2. These cracks can provide an additional surface area for recombination of deuterium atoms into molecules during the plasma exposure, thus, reducing the effective deuterium influx into the bulk of tungsten. This can lead to a reduction of the deuterium accumulation rate at high fluences.

Chapter 6

Deuterium interaction with vacancies in tungsten

The previous chapter was devoted to investigations of deuterium trapping in defects introduced by the exposure of pristine tungsten to divertor-like particle fluxes, which is relevant for the non-nuclear phase (hydrogen discharges) of ITER. In the deuterium-tritium phase of ITER, bombardment with 14 MeV neutrons will introduce radiation defects (vacancies, vacancy clusters, dislocation loops, etc.) through the whole thickness of tungsten PFCs (see section 3.4). These defects will likely govern the retention. Therefore, the knowledge of hydrogen binding energies with them is essential for predicting hydrogen transport and trapping in tungsten PFCs. However, the reported values often show a large scatter and there is no consensus on which values are the most reliable (see section 3.3). The hydrogen binding energy with a defect can be directly determined with high accuracy from the shift of the desorption maximum in a series of TDS measurements performed with identical samples and different heating rates [53]. This technique was utilized in the present chapter[1] to determine the deuterium binding energy with vacancies in tungsten.

6.1 Experimental details

The experiments were carried out in the MEDION setup (see section 4.2.1 for the description). The sample was cut from a 25 μm thick hot-rolled polycrystalline tungsten foil with a purity of 99.97 wt. % produced by Plansee.

1. The work presented in this chapter is partly already published in the papers: M. Zibrov, Yu. Gasparyan, S. Ryabtsev, A. Pisarev, *Isolation of peaks in TDS spectra of deuterium from ion irradiated tungsten*, Physics Procedia **71**, 83 (2015) and M. Zibrov, S. Ryabtsev, Yu. Gasparyan, A. Pisarev, *Experimental determination of the deuterium binding energy with vacancies in tungsten*, Journal of Nuclear Materials **477**, 292 (2016).

The impurity concentrations specified by the supplier are listed in table C.1 in appendix C. The foil had a shiny surface finish in the as-delivered state and was not additionally polished. It was successively cleaned in an ultrasonic bath with gasoline, acetone, and ethanol. In order to minimise the concentration of dislocations and grain boundaries in the sample and to remove gaseous impurities, it was *in situ* annealed at 1800 K for 30 min, which results in the full recrystallization of the material [14]. SEM investigations reveal that the recrystallized sample has large isotropic grains up to 50 μm.

One specimen was used for all measurements. The experiments presented here were carried out after approximately 20 cycles of irradiation and annealing of the sample, which should result in the removal of surface impurities (such as oxygen and carbon) which are expected on the virgin specimen. In addition, since all the experiments were carried out under UHV conditions without exposure of the sample to air, adsorption of impurities on the sample surface was suppressed. Consequently, it is assumed that under the present experimental conditions the concentration of impurities on the sample surface was low, hence, according to the Pick and Sonnenberg model [25], the recombination rate should be high enough not to affect the TDS spectra. Therefore, the method for determination of binding energies from TDS measurements with different heating rates (see section 2.4) should be applicable under the present experimental conditions.

As the same sample was used for all measurements, it was annealed *in situ* at 1700 K for 1 h before every new experiment. Since the irradiation fluences were very low, no irreversible material modifications (e.g., formation of blister-like structures) are expected [86, 133]. This is confirmed by the reproducibility of the experimental results, which means that there was no accumulation of radiation damage in the sample after its multiple use. Therefore, the used annealing scheme was effective for elimination of all radiation defects, in line with the PALS results presented in the following chapter.

6.2 Experimental results and discussion

The present experimental approach is based on the fact that damaging by light ions produces mainly Frenkel pairs as primary damage, and that the damage levels must stay low ($< 10^{-2}$ dpa [82]) in order to avoid the formation of complex defect structures (see section 3.4).

As a first attempt, damaging of the sample by 10 keV D^+ ions to various fluences and subsequent TDS analyses were carried out (Fig. 6.1). All the obtained spectra exhibit at least three maxima at about 400 K, 600 K, and 750 K, and their amplitudes increase with fluence. The observed peaks are strongly overlapping, thus, such spectra cannot be used in experiments with different heating rates.

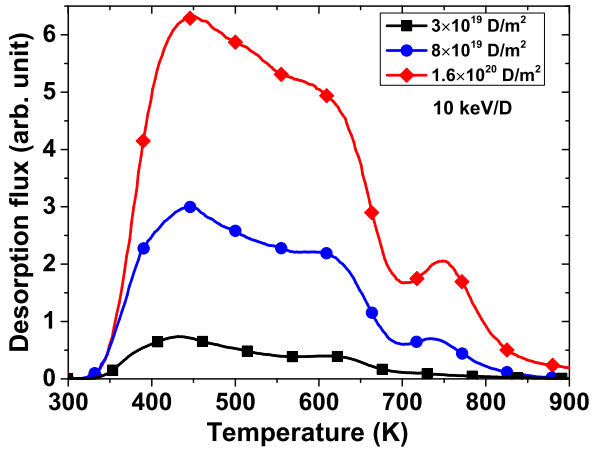

Fig. 6.1: TDS spectra of D_2 molecules from recrystallized tungsten damaged by 10 keV/D ions to various fluencies. The TDS heating rate is 2 K/s.

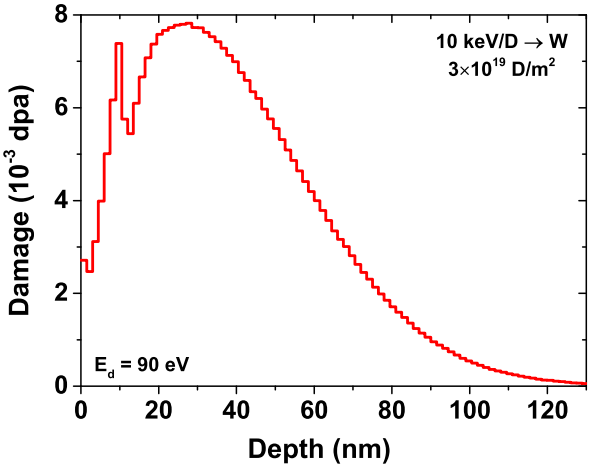

Fig. 6.2: Damage profile in tungsten irradiated by 10 keV/D ions to the fluence of 3×10^{19} D/m^2 calculated using SRIM. Note that the peak at a depth of 10 nm is an artefact due to the free flight path concept of SRIM as described in appendix A.

In order to obtain spectra with well-resolved peaks, the following procedure was used. The radiation defects were introduced by irradiation with 10 keV/D ions to a fluence of 3×10^{19} D/m^2. According to SRIM [134] calculations (the details of the calculations are described in appendix A), under such conditions the damage profile has a maximum located at a distance of 28 nm from the surface and the corresponding maximum damage level is 7.8×10^{-3} dpa (Fig. 6.2). This damaging fluence allows obtaining a TDS spectrum with a reasonable signal/background ratio while still staying at a low dpa level. Then the damaged sample was annealed at 550 K for 5 min. This temperature is high enough to remove a substantial part of deuterium from the defects, but,

concurrently, the vacancies are still immobile at this temperature, therefore, the growth of vacancy clusters should not take place, as will be shown in chapter 7. Afterwards, in order to fill the defects with deuterium without producing additional displacement damage, the sample was implanted with 0.67 keV/D ions (2 keV D_3^+) to a fluence of 1×10^{19} D/m^2. As a result, the TDS spectrum consists of a low-temperature peak near 400 K, a major release peak near 600 K, and a shoulder near 750 K (Fig. 6.3).

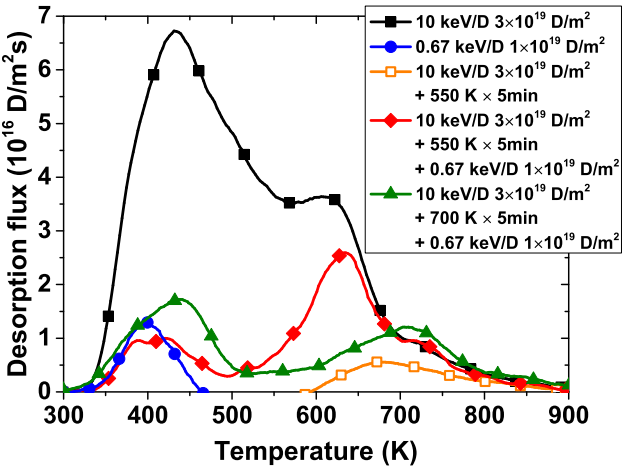

Fig. 6.3: A comparison of TDS spectra of D_2 molecules from recrystallized tungsten damaged by 10 keV/D ions to the fluence of 3×10^{19} D/m^2 (solid squares); recrystallized tungsten implanted with 0.67 keV/D ions to the fluence of 1×10^{19} D/m^2 (solid circles); recrystallized tungsten damaged by 10 keV/D ions to the fluence of 3×10^{19} D/m^2 and then annealed at 550 K for 5 min (open squares); recrystallized tungsten damaged by 10 keV/D ions to the fluence of 3×10^{19} D/m^2, subsequently annealed either at 550 K (solid diamonds) or 700 K (solid triangles, taken from [135]) for 5 min, and then implanted with 0.67 keV/D ions to the fluence of 1×10^{19} D/m^2. The TDS heating rate is 2 K/s.

Implantation of the undamaged sample with 0.67 keV/D ions to the same fluence of 1×10^{19} D/m^2 results in the appearance of only the 400 K peak in the TDS spectrum (Fig. 6.3), demonstrating that the peak near 600 K and the shoulder near 750 K correspond to deuterium release from radiation defects created by 10 keV/D ions. This low-energy implantation of the annealed sample was also performed at the end of the experimental campaign, which gave the same TDS spectrum exhibiting only one 400 K peak, confirming the fact that there was no accumulation of radiation damage in the sample after its multiple use. As was already mentioned, it is assumed that during the 10 keV/D damaging predominantly Frenkel pairs are created. The created self-interstitial atoms are already mobile at room temperature (see section 3.4) and can either disappear on the surface or agglomerate to form interstitial type dislocation loops with a Burgers vector of $\mathbf{b} = (1/2)\langle 111 \rangle$ [133]. Molecular statics simulations by Grigorev et al. [74] demonstrate that these loops exhibit

a wide spectrum of binding energies up to 1.1 eV, which is lower than the energy predicted for a single vacancy (see section 3.3.2). Consequently, the peak near 600 K can be attributed to deuterium release from vacancies in tungsten.

The first rather broad peak near 400 K was previously shown to consist of several more narrow peaks [68]. From the present results for the undamaged sample, it can be concluded that a part of this peak corresponds to deuterium release from intrinsic bulk defects (like grain boundaries, dislocations, impurities) [56] and/or from adsorption sites on the surface [57, 71].

It is important to mention that DFT studies predict that a single vacancy in tungsten can trap several hydrogen atoms at room temperature. The binding energies of the first and the second trapped atom are almost identical, whereas for the third and subsequent atoms they are considerably lower (see Fig. 3.3). As a result, the 600 K peak may be in principle composed of two closely located peaks corresponding to the release of the first and the second trapped deuterium atom from a vacancy; the third and the rest of the trapped atoms in a vacancy can give a contribution to the 400 K peak. In addition, the release of deuterium trapped by dislocation loops can also contribute to the 400 K peak.

If the annealing temperature is above 600 K, then vacancies become mobile and agglomerate in clusters, as will be shown in chapter 7. As can be seen from Fig. 6.3, in the case of annealing at 700 K the desorption peak at 600 K almost disappears, whereas the amplitude of the peak near 750 K increases [135]. Hence, the peak near 750 K can be attributed to deuterium release from vacancy clusters, indicating that they have a higher binding energy for deuterium than vacancies, in line with theoretical estimations described in section 3.3.2.

After annealing of the damaged sample at 550 K, subsequent TDS reveals that only a very small amount of deuterium remains in the sample ($<10\,\%$) and its release takes place at temperatures above 600 K (Fig. 6.3). This confirms that most of the deuterium trapped in vacancies was removed during this annealing and that the fraction of deuterium retained in traps with higher binding energies is relatively small. In addition, the amplitude of the shoulder near 750 K in the spectrum of the damaged sample annealed at 550 K and subsequently implanted with 0.67 keV/D ions is the same as that of the spectrum from the sample only damaged by 10 keV/D ions (Fig. 6.3). This confirms that no noticeable clustering of vacancies in the sample took place during annealing at 550 K. Furthermore, this also confirms that only a relatively small fraction of vacancy clusters is formed during the damaging.

In order to determine the deuterium binding energy with vacancies in tungsten, the experimental sequence described above was performed several times in series, and the only difference was the TDS heating rate. Obviously, the heating rates should be varied in a wide range for accurate determination of binding energies. However, at very low heating rates the measurements are limited by a low signal/background ratio, whereas at sufficiently high heating rates the non-linearity of the heating ramp starts playing a role. Therefore, in the present experiments, the variation of heating rates was limited to 0.15–4 K/s.

The maximum concentration of introduced vacancies $N_V \approx 1 \times 10^{-3}$ at. fr. was estimated from the amount of deuterium released in the 600 K peak by assuming that the vacancy concentration profile has the shape of the damage profile calculated in SRIM (Fig. 6.2). This concentration is within the limit of the retrapping-limited regime: $N_V \gg (\lambda/\Delta)^2 \approx 4 \times 10^{-6}$ at. fr. with $\lambda = a_0/\sqrt{8} = 0.112$ nm [42] and $\Delta \approx 60$ nm as estimated from the FWHM of the damage profile (see section 2.4 for details). Even though in simulations of TDS spectra it is commonly assumed that the activation energy for trapping E_{tr} is equal to the activation energy for diffusion E_D, the DFT calculations indicate that $E_{tr} < E_D$ for vacancies in tungsten [44]. In that case ($E_{tr} \leq E_D$) numerical calculations using the TMAP7 code [50] (using the effective recombination rate coefficient from the Pick and Sonnenberg model [25] for a clean surface) indicate that under the present experimental conditions (using the estimated concentration profile of vacancies) the sum $E_b + E_D$ will be indeed determined from the Arrhenius-like plot $\ln(\beta/T_m^2)$ versus $1/T_m$. Therefore, it is assumed that in the present experiments the sum $E_b + E_D$ for vacancies in tungsten is determined. In addition, the simulations confirm that the presence of additional trapping sites in the material (both with lower and higher binding energies) does not affect the determined binding energy.

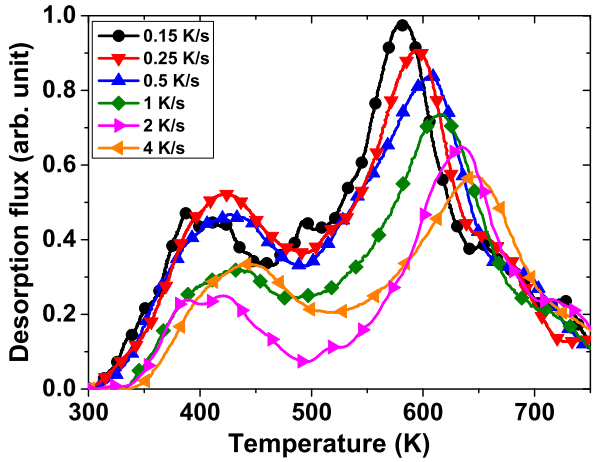

Fig. 6.4: TDS spectra of D_2 molecules from recrystallized tungsten damaged by 10 keV/D ions to the fluence of 3×10^{19} D/m^2, subsequently annealed at 550 K for 5 min, and then implanted with 0.67 keV/D ions to the fluence of 1×10^{19} D/m^2. The TDS heating rates were varied in the range of 0.15–4 K/s. Note that for convenience all the spectra are plotted not in scale.

Fig. 6.4 shows the results of the TDS measurements performed with different heating rates. For convenience, all the spectra are plotted not in scale. As can be seen, the second peak corresponding to deuterium release from vacancies clearly shifts towards higher temperatures with increasing heating rate (from 584 K at 0.15 K/s to 649 K at 4 K/s). However, no clear shift of the first peak is observed. Moreover, the ratios of amplitudes of the two peaks are also different

at various heating rates, although the conditions in all the experiments were kept as close as possible. The origin of these variations is not completely clear. An important factor might be the release of heteronuclear deuterium-containing molecules (HD, HDO, D_2O). As an example, Fig. 6.5 shows the TDS spectra of H_2, D_2, HD, HDO, and D_2O molecules in the measurement with a heating rate of 0.25 K/s. As can be seen, the contributions of HDO and D_2O molecules are small, which indicates the presence of only a relatively small amount of oxygen on the sample surface [120]. However, the HD signal is considerable and its contribution to the total retention also decreases with increase of the heating rate (from 35 % at 0.15 K/s to 24 % at 4 K/s). Such variations may be due to adsorption of different amounts of impurities (e.g., protium, water) on the sample surface from the residual gas during TDS performed at different heating rates due to the difference in duration of the measurements (from several minutes at the highest heating rate to more than one hour at the lowest heating rate). The release of H_2 molecules is significantly higher compared with that of deuterium-containing molecules, and the maximum of its release is located at around 700 K and slowly decreases at higher temperatures. Such a high release of H_2 molecules was observed also in the case of a background run with a non-irradiated sample, while essentially no increase of D_2 and HD signals were observed. Hence, the H_2 molecules probably originate from the vessel walls heated by radiation from the sample during the measurement. At high sample temperatures, H_2 molecules can dissociate on the sample surface, i.e., H-D isotope mixing on the surface can take place. This can be the reason for the presence of a long high-temperature tail in the HD spectrum, which is not present in the D_2 spectrum. More details about the mechanisms of the formation of heteronuclear molecules can be found in [119, 120].

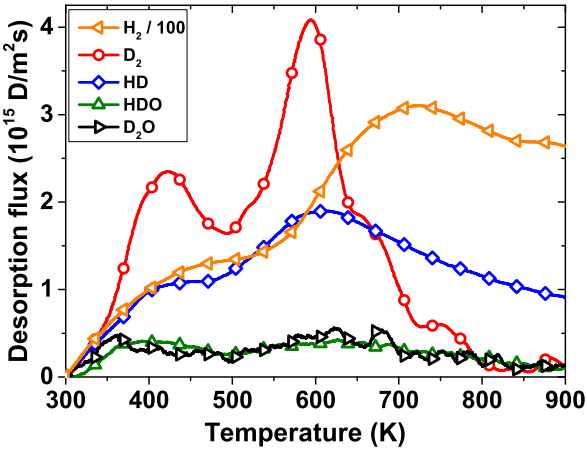

Fig. 6.5: TDS spectra of H_2, D_2, HD, HDO, and D_2O molecules from recrystallized tungsten damaged by 10 keV/D ions to the fluence of 3×10^{19} D/m^2, subsequently annealed at 550 K for 5 min, and then implanted with 0.67 keV/D ions to the fluence of 1×10^{19} D/m^2. Note that the spectrum of H_2 molecules is downscaled by a factor of 100. The TDS heating rate is 0.25 K/s.

Fig. 6.6 shows a comparison of TDS spectra obtained after identical (as technically achievable) implantation conditions for the same sample but in different experimental campaigns. Despite the non-perfect reproducibility of the shapes of the peaks and their relative amplitudes, the positions of the peaks around 600 K are the same (within the uncertainty of the measurements) for both experiments. The amounts of deuterium released as D_2 molecules differ only within 14 %. This gives additional confidence about the reliability of the experimental procedure and a rather good reproducibility of the results, which is always limited in the case of very low amounts of trapped deuterium [56, 118].

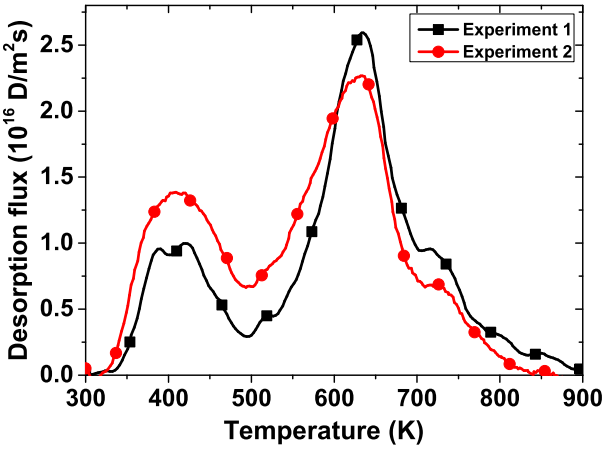

Fig. 6.6: A comparison of TDS spectra of D_2 molecules obtained in different experimental campaigns from recrystallized tungsten damaged by 10 keV/D ions to the fluence of 3×10^{19} D/m^2, subsequently annealed at 550 K for 5 min, and then implanted with 0.67 keV/D ions to the fluence of 1×10^{19} D/m^2. The same sample was used in both experiments. The TDS heating rate is 2 K/s.

Fig. 6.7 shows the semilogarithmic plot of β/T_m^2 versus $1/T_m$ for the peak corresponding to the deuterium release from vacancies. The linear fit according to the least squares analysis is also shown. The main contribution to the uncertainty of the $1/T_m$ value is given by the accuracy of the peak position determination. This is due to a high noise level in the TDS spectra at low heating rates (see Fig. 4.6): the lower the heating rate, the lower is the signal-to-noise ratio of the QMS signal. The specified uncertainty of the temperature measurement by the thermocouple of 0.7 % (for the temperature expressed in °C) is also included in the total uncertainty of the temperature measurement. The uncertainty of the heating rate has a negligible influence in the present experiments. The sum of the deuterium binding energy E_b with vacancies (for the first and probably the second trapped deuterium atom) and the activation energy for deuterium diffusion E_D in tungsten, calculated from the slope of the fit according to Eq. 2.12, is $E_b + E_D = 1.56 \pm 0.06$ eV. The fact that all data points are well fitted by a straight line indicates that the present results

are presumably not influenced by the recombination rate; otherwise, a crook on the curve would be observed, as predicted by TMAP7 simulations [136].

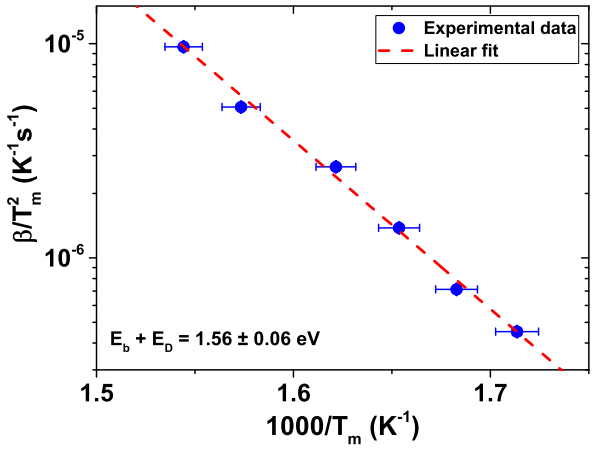

Fig. 6.7: Semilogarithmic plot of β/T_m^2 versus $1/T_m$ for the peak corresponding to the deuterium release from vacancies in tungsten, where T_m is the peak position and β is the TDS heating rate. The best linear fit is also shown.

The value of $E_b + E_D = 1.56 \pm 0.06$ eV is in a good agreement with that obtained from DFT calculations by You et al. [30] (1.57 eV both for the first and the second hydrogen atom in a vacancy) and by Heinola et al. [43] (1.6 eV and 1.57 eV for the first and the second hydrogen atom in a vacancy, respectively). It is also only 9 % higher compared with the widely used value of 1.43 ± 0.02 eV obtained by Eleveld and van Veen [57] from simulations of TDS spectra.

6.3 Chapter summary

Experiments on thermal desorption of deuterium from recrystallized tungsten were carried out under conditions when single vacancies give a dominant and well-resolved peak. Introduction of predominantly Frenkel pairs as primary defects was done by irradiation with 10 keV deuterium ions to a low damage level (7.8×10^{-3} dpa). All experimental steps were performed *in situ* without exposure of the sample to air, allowing to minimise the presence of impurities on the surface that can cause a reduction of the deuterium recombination rate. A series of TDS spectra was measured at different heating rates under identical conditions of defect production and deuterium loading. Experimental data on the shift of the desorption maxima as a function of heating rate were analysed using analytical formulas obtained for the condition of a high deuterium recombination rate at the surface. The functional Arrhenius-like dependence using the experimental data was perfectly linear as the analysis predicts. By using this method the sum of the deuterium binding energy with vacancies (for the first and probably the second trapped deuterium atom) and the activation

energy for deuterium diffusion in tungsten ($E_b + E_D = 1.56 \pm 0.06$ eV) was directly determined with a high accuracy and without any assumptions or prior knowledge of trap parameters. This was possible thanks to the good reproducibility of the data and accurate temperature measurements.

Chapter 7

Annealing and clustering of vacancies in tungsten

In ITER and future fusion reactors tungsten PFCs will operate at elevated temperatures, resulting in a thermal evolution of the primary radiation defects like annihilation or, if their concentration is high enough, agglomeration into more stable extended defects (vacancy clusters, dislocation loops). There is a lack of experimental data on the thermal evolution of vacancies in tungsten providing quantitative information about the sizes of stable defect clusters at various annealing temperatures and their relation to deuterium retention (see sections 3.3 and 3.4). This chapter presents the results of experiments devoted to the investigation of deuterium interactions with vacancy clusters in tungsten created by annealing of samples containing predominantly vacancies at various temperatures. The sizes of the clusters are determined by using the PALS technique. In addition, the effect of high damage levels on the annealing of defects is briefly examined.

7.1 Experimental details

The fate of radiation defects in a metal depends not only on their mobility and concentration but also on the presence of defect sinks, such as grain boundaries and dislocations, as well as of impurities able to decorate defects. To have a well-defined system, it is desirable to use single crystalline specimens, which do not have high-angle grain boundaries and have a smaller density of dislocations and less impurities compared with polycrystalline materials. When irradiation is done with ions, the damaged zone is only several μm thick, which makes the surface a dominant and well-defined sink for the defects.

The specimens were prepared from a high-purity single crystalline tungsten rod grown along the $\langle 100 \rangle$ direction by electron-beam floating zone melting at

the Institute of Solid State Physics (Chernogolovka, Russia) [137, 138]. The accuracy of the rod orientation is within 2°. The dislocation density in it is in the range of 10^9–10^{11} m^{-2} and most of the dislocations are arranged in walls, forming low-angle grain boundaries with a mean grain size around 500 μm. The impurity concentrations specified by the manufacturer are listed in table C.2 in appendix C. The samples with (100) crystal surfaces were cut by spark erosion from the rod to $10 \times 10 \times 1$ mm^3. The residue from the cutting was removed by grinding of the samples with a set of SiC sandpapers with decreasing grit sizes (up to P4000). Then they were electrochemically polished to a mirror-like finish in a 1.5 wt. % NaOH aqueous solution at a voltage of 19 V for 15 min. Analysis of two specimens after cutting and polishing by the Laue X-ray diffraction method showed that their surface normal is within 3° of the ⟨100⟩ direction. The samples were successively cleaned in an ultrasonic bath with acetone, isopropanol, and a high-purity acetone and then rinsed in deionized water. To reduce the possible spatial non-homogeneity of the microstructure and remove gaseous impurities, the specimens were first outgassed at a temperature near 1300 K for 20 min and then annealed at about 2600 K for 3 min (as a series of 30 s annealings) at a pressure below 10^{-5} Pa.

The present approach to introduce mainly Frenkel pairs as primary defects is similar to that used in the previous chapter and utilizes damaging by 200 keV protons to a fluence of 1×10^{20} p/m^2 at the tandem accelerator (see section 4.2.2 for the description). According to SRIM [134] calculations (the details of the calculations are described in appendix A), the damage profile is non-uniform with a pronounced maximum (Bragg peak) of 5.8×10^{-3} dpa located at a depth of 0.7 μm (Fig. 7.6). This damage level is lower compared with that used in the previous chapter (7.8×10^{-3} dpa).

After damaging, the samples were annealed in vacuum for 15 min at temperatures in the range of 500–1800 K. This range starts from a temperature at which vacancies in tungsten were reported to be immobile and ends at a temperature where full recovery of radiation defects was observed [87–89]. Annealing at temperatures in the range of 500–1300 K was done in the TESS setup (see section 4.3.2 for the description). In these experiments, the oven was preheated to a certain temperature and then quickly pushed over the quartz tube. At the end of the heating cycle, the furnace was rapidly retracted from the tube. Fig. 7.1 illustrates the heating and cooling curves for a tungsten sample during annealing at three different temperatures. With increasing annealing temperature the heating takes less time: around 40 min to reach 500 K, and only about 2.5 min to achieve 1300 K. This is due to a decrease of tungsten spectral emissivity and, respectively, absorption coefficient, with increasing wavelength in the IR range [139]. The cooling-down of a sample from 1300 K to 600 K takes only 6 min, whereas cooling to 350 K takes around 40 min. This is because at high temperatures the cooling is dominated by thermal radiation, whereas at low temperatures it is governed by thermal conductance, which is kept low for heating purposes. Annealing at temperatures in the range of

1400–1800 K was done in a different setup, where the samples were located in tungsten U-shaped cradles and heated by 3 keV electron bombardment from the side opposite to the damaged side at a pressure below 10^{-5} Pa. The sample temperature was measured with a disappearing-filament pyrometer (Keller Mikro PV 11). The real sample temperature was calculated from the measured brightness temperature by the iteration procedure employing Planck's radiation law and the temperature-dependent tungsten spectral emissivity taken from [139]. The sample temperature was ramped to the desired one within a few minutes. The cooling-down of the samples was not monitored.

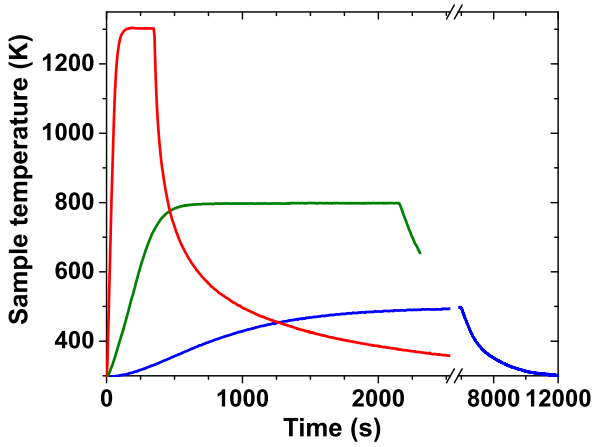

Fig. 7.1: Examples of heating and cooling curves for a tungsten sample during annealing at three different temperatures in the TESS setup. In the case of annealing at 800 K the recording was stopped during the sample cooling-down.

To study deuterium retention only in radiation-induced defects, deuterium trapping by the intrinsic defects with low binding energies observed in chapter 6 should be minimised. Therefore, deuterium plasma exposures of the samples were carried out at a temperature of 450 K in the PlaQ plasma device (see section 4.1.1 for the description) to a fluence of 1×10^{25} D/m^2.

7.2 Positron annihilation analysis

All samples were analysed by PALS at a positron energy of 18 keV. In this case, the mean positron implantation depth is 0.2 μm and the implantation profile extends to 0.6 μm (see Fig. 4.16), while the calculated maximum of the damage created by 200 keV protons is located at a depth of 0.7 μm (see Fig. 7.6). Consequently, only a part of the damaged zone is probed by positrons. Already the raw lifetime spectra shown in Fig. 7.2 clearly demonstrate significant differences in the positron lifetimes, and, hence, in the defect structure of the samples after damaging and annealing.

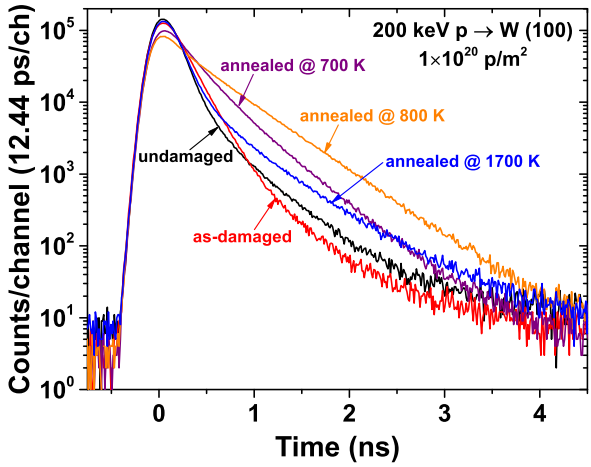

Fig. 7.2: Positron lifetime spectra at 18 keV positron implantation energy for tungsten (100) single crystals damaged by 200 keV protons to a fluence of 1×10^{20} p/m^2 and then annealed at various temperatures for 15 min.

The measured lifetime spectra can be decomposed into three to four lifetime components. Although the decomposition may be sometimes ambiguous due to the extreme sensitivity of exponential fits to noise in the data [140], the average positron lifetime is a statistically accurate parameter representing "the centre of mass" of the spectrum and is almost independent of the details of the decomposition. It reflects the interplay between the increase of the defect size (which increases lifetime) and the decrease of their concentration (which decreases their relative intensity in the spectra).

Fig. 7.3 shows the evolution of the average positron lifetime with post-damaging annealing temperature. An undamaged sample has the lowest lifetime close to the typical defect-free bulk lifetime, indicating that most of the positrons annihilate from the delocalized bulk state. Damaging by 200 keV protons increases the average lifetime to 156 ps, demonstrating introduction of small open-volume defects. Post-damaging annealing up to 600 K results in a rather slow increase of the lifetime, indicating only minor changes in the defect structure. After annealing at 700 K and 800 K, a sharp increase of the lifetime is visible, demonstrating trapping of positrons in large open-volume defects, such as vacancy clusters. The lifetime then stays almost constant after annealing at temperatures in the range of 800–1200 K, indicating a stable situation. At higher annealing temperatures, it gradually decreases with increasing annealing temperature, indicating defect recovery. Eventually, after annealing at 1800 K the average lifetime is the same as in the undamaged sample, demonstrating complete removal of radiation defects.

Fig. 7.4 shows the results of the decomposition. As the intensity of the fourth lifetime is always below 1 %, it will be neglected in the following discussion, and the third lifetime will be always referred to as the longest lifetime. To assess

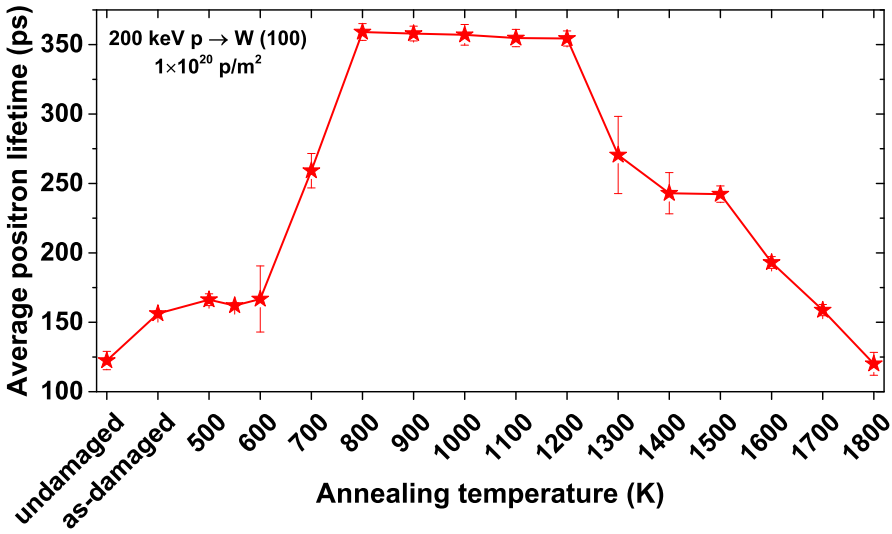

Fig. 7.3: The average positron lifetime as a function of annealing temperature for tungsten (100) single crystals damaged by 200 keV protons to a fluence of 1×10^{20} p/m^2 and then annealed at various temperatures for 15 min. The positron implantation energy is 18 keV.

the reproducibility of the sample preparation procedures, two undamaged and two as-damaged specimens have been measured and in both cases the spectra of two samples are almost indistinguishable. To reduce scatter in the data, the averaged results over two undamaged and as-damaged samples are shown in Figs. 7.3 and 7.4.

The undamaged sample exhibits three lifetime components. The shortest lifetime corresponds to the reduced bulk lifetime (its physical meaning is explained in appendix B) and the longest lifetime near 350 ps can be attributed to annihilation at the surface. Although the latter lifetime is also characteristic for vacancy clusters, their presence in the undamaged samples is very unlikely. The specimens have been annealed at 2600 K, where the equilibrium concentration of thermal vacancies is low (3×10^{-6} at. fr.) [84], and the sample cooling rate was rather slow (i.e., far from quenching). In addition, the results of positron annihilation Doppler broadening spectroscopy (DBS) measurements (also performed at NEPOMUC) indicate a positron diffusion length before the annihilation of about 120 nm, which is typical for well-annealed metal crystals [123]. Hence, a noticeable fraction of positrons must reach the surface and annihilate there and the longest lifetime should correspond to annihilation at the surface. The reported lifetimes at metallic surfaces (both experimentally determined and calculated) are lying in a wide range of 350–600 ps [124, 141, 142]. The second lifetime is around 100 ps, which is very close to the defect-free bulk lifetime in tungsten [126, 143, 144], and its appearance may be related with channelling of implanted positrons [123].

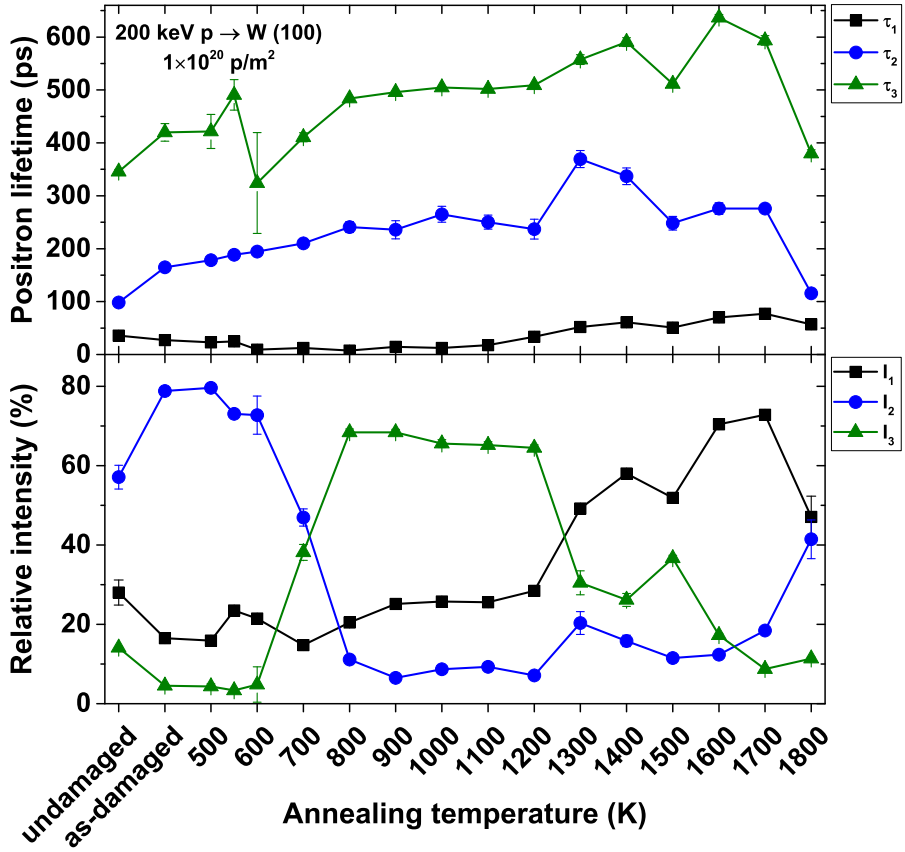

Fig. 7.4: Positron lifetimes (upper panel) and their relative intensities (lower panel) as a function of annealing temperature for tungsten (100) single crystals damaged by 200 keV protons to a fluence of 1×10^{20} p/m^2 and then annealed at various temperatures for 15 min. The positron implantation energy is 18 keV.

Damaging by protons introduces open-volume defects into the material. Almost 80 % of positrons are trapped in defects with a lifetime of 165 ps. Less than 5 % of positrons are trapped in defects with a lifetime around 420 ps. From the DBS measurements of this sample, it appears that the positron diffusion length is in the range of 10 nm. Therefore, the fraction of positrons back diffusing to the surface can be neglected and this component should correspond to annihilation at vacancy clusters introduced during damaging.

Post-damaging annealing at temperatures in the range of 500–600 K results in a gradual increase of the second lifetime up to 195 ps, which is likely due to the release of trapped protium from vacancies occurring in this temperature range, as was shown in the previous chapter. The decrease of the positron lifetime after decoration of vacancies with protium has been observed by de Vries [89] and is backed by DFT calculations [126]. A dominant lifetime near 200 ps is also observed in the samples damaged by 4.5 MeV electrons (see

appendix E for the description), where only Frenkel pairs were introduced, and is in a good agreement with the calculated positron lifetime in a single vacancy in tungsten [126, 144]. This confirms that damaging by 200 keV protons allows introducing predominantly Frenkel pairs as primary defects. The value of the longest lifetime fluctuates around 420 ps, while its intensity stays within 5 % indicating little changes in the structure of existing vacancy clusters.

Annealing at 700 K and 800 K results in a sharp increase of the value and intensity of the longest lifetime component accompanied by a decrease of the intensity of the second lifetime. This indicates that at 700 K vacancies in tungsten are appreciably mobile and can agglomerate into clusters the lifetime of which (410 ps) corresponds to clusters containing about 13 vacancies according to DFT calculations by Troev et al. [126]. Still about a half of the positrons annihilate in defects with a lifetime of 210 ps representing the mixture of annihilation at vacancies and small vacancy clusters after 700 K annealing. After annealing at temperatures in the range of 800–1200 K the lifetime components are almost constant. The dominant longest lifetime close to 500 ps demonstrates the presence of clusters containing at least 30 vacancies[1] and represents the theoretical limit of the positron lifetime in a cavity in a metal (corresponding to the spin-averaged positronium lifetime in vacuum) [124].

After annealing at 1300 K and higher temperatures, the fraction of positrons annihilating at the delocalized bulk state gradually increases, indicating defect recovery. However, the longest lifetime increases up to about 600 ps until an annealing temperature of 1700 K while its intensity decreases. This lifetime is above the theoretical limit of 500 ps described above and may correspond to pick-off annihilation of ortho-positronium formed in large vacancy clusters[2]. Since positronium can be formed only in materials without free electrons, this suggests that the internal surfaces of the clusters can be partially decorated with impurities like oxygen and carbon [145]. Hu et al. [146] reported the formation of voids with a diameter around 1 nm visible in TEM after post-irradiation annealing at 1273 K of a tungsten single crystal damaged by fission neutrons to 3×10^{-2} dpa. Therefore, it is possible that in the present experiments further coarsening of vacancy clusters accompanied by the segregation of impurities at their surfaces took place at these temperatures.

After annealing at 1800 K the lifetime components are the same as in the undamaged sample, while the intensities of the first and second components are different, which can be due to the above mentioned effect of positron channelling.

1. According to calculations by Troev et al. [126], this is the size of the cluster starting from which the positron lifetime does not depend on the cluster size anymore.
2. Positronium is the bound state of a positron and an electron (quasiatom) and has two possible states (ortho and para) depending on the total spin. The pick-off process corresponds to the annihilation of a positron in ortho-positronium with an electron of the medium.

7.3 Deuterium retention

Deuterium plasma exposure resulted in the unexpected appearance of surface modifications on the as-damaged sample (Fig. 7.5). All observed features are step-like and irregularly-shaped with dimensions of a few μm, thus, according to the classification given in chapter 5, they will be referred to as protrusions. Cross-sectioning of two protrusions reveals that their cavities are formed by cracks running approximately perpendicular to the surface and extending up to 1.6 μm (Fig. 7.5(b)). The observed cracks are also not exactly located under the corresponding surface structures. Post-damaging annealing at 500 K results in a decrease of the number density of these protrusions. On samples annealed at 550 K and higher temperatures, as well as on an undamaged sample, no apparent surface modifications were detected. Concurrently, only small changes in the defect structure are visible by PALS at these annealing temperatures.

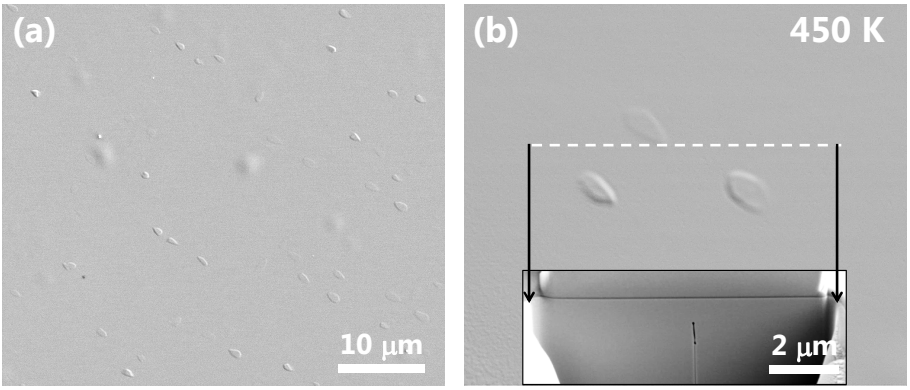

Fig. 7.5: SEM images with different magnifications of a tungsten (100) single crystal damaged by 200 keV protons to a fluence of 1×10^{20} p/m^2 and then exposed to a deuterium plasma with a mean ion energy of 10 eV/D to a fluence of 1×10^{25} D/m^2 at a sample temperature of 450 K. The inset in (b) shows a SEM image of a cross-section at the position indicated by the dashed line; the black arrows indicate the same places in (b) and the inset. The surface in the inset was protected by a Pt-C layer before cutting. Note that the hemispherical structures in (a) are artefacts of electrochemical polishing. The images were taken after TDS.

Fig. 7.6 shows the measured deuterium concentration profiles[3] in the samples annealed at various temperatures. The concentration in the undamaged sample is very low (a few times 10^{-6} at. fr.) and could not be accurately measured. The deuterium depth profile in the as-damaged sample has a maximum in the depth range agreeing with SRIM predictions. However, it extends up to 1.9 μm, while SRIM predicts no damage production at depths beyond 1 μm. Recalling the discussion in chapter 5 regarding the relation between the appearance of surface

3. To minimise the ^{3}He channelling in single crystalline specimens, the measurements were carried out at an incidence angle of 40°, which was found experimentally to be the optimal one due to the minimum variation of ^{3}He backscattering spectra among different samples.

modifications and the corresponding introduction of additional trapping sites in the material, this can be explained by the fact that the cracks observed in the cross-sectional SEM images extend up to 1.6 μm. With increasing annealing temperature, the maximum concentration decreases and the profile becomes less peaked; also the part of the profile at depths larger than 0.9 μm shrinks and its amplitude decreases. After annealing at 1300 K and above a depletion of deuterium in the near-surface region is visible and the width of the depleted zone increases with increasing annealing temperature. This probably is due to the fact that the surface acts as a sink for radiation defects, resulting in the formation of a defect-denuded zone.

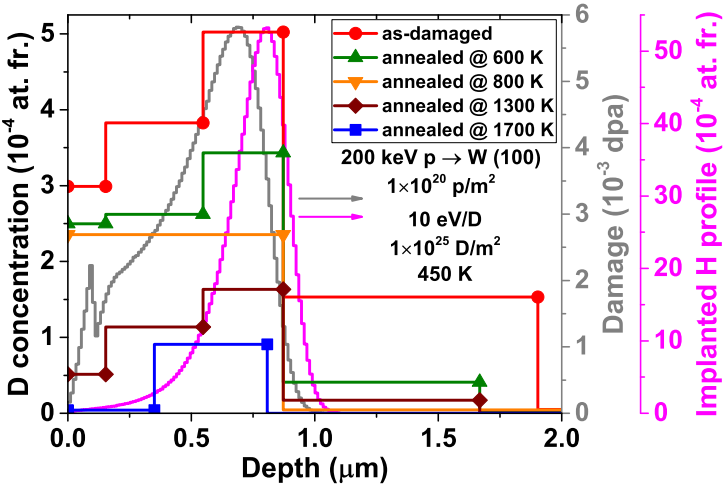

Fig. 7.6: Deuterium concentration profiles in tungsten (100) single crystals damaged by 200 keV protons to a fluence of 1×10^{20} p/m^2, post-irradiation annealed at various temperatures for 15 min and then exposed to a deuterium plasma with a mean ion energy of 10 eV/D to a fluence of 1×10^{25} D/m^2 at a sample temperature of 450 K. The damage profile created by 200 keV protons (grey line) and the implantation profile (magenta line) calculated using SRIM are also shown. Note that the peak at a depth of 93 nm in the damage profile is an artefact due to the free flight path concept of SRIM as described in appendix A.

The deuterium concentrations at the damage peak and the total deuterium inventories determined by NRA as a function of post-damaging annealing temperature are summarized in Fig. 7.7. Although the damaging was carried out near 290 K, the lowest data point is at 450 K since it is possible that some defect annealing occurred during the plasma exposure at this temperature. The first rapid decrease of the maximum deuterium concentration occurs already after annealing at 550 K. As was previously discussed, this decrease is likely not only connected with annealing of the defects introduced by damaging with protons, but also with the decrease of the concentration of defects introduced together with protrusions. The next major decrease of the concentration occurs at 800 K and 900 K and then it stays constant up to 1200 K. After annealing at 1300–1500 K the concentration slightly decreases and a rapid decrease starts after

annealing at 1600 K until complete defect recovery at 1800 K. Note that the non-zero retention in the undamaged sample is due to the presence of intrinsic defects, most likely impurities such as carbon and oxygen, which cannot be removed from the material in the course of annealing and which are able to bind deuterium relatively strongly [70]. The evolution of deuterium retention determined by NRA as a function of annealing temperature generally follows the same trend as the maximum deuterium concentration.

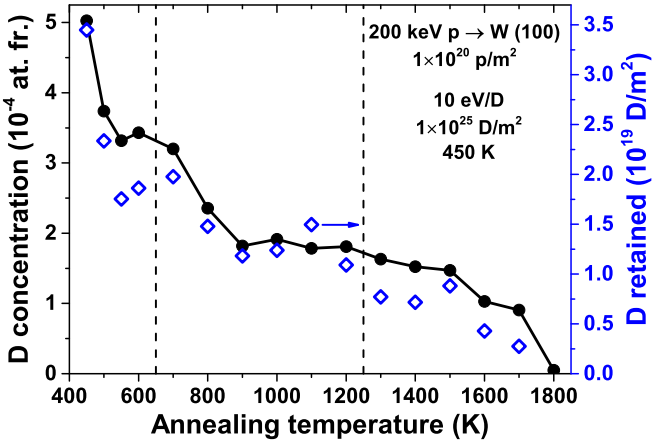

Fig. 7.7: Deuterium concentration in the damage peak (solid circles) and total deuterium inventory in the damaged layer as derived from NRA (open diamonds) as a function of the post-irradiation annealing temperature in tungsten (100) single crystals damaged by 200 keV protons to a fluence of 1×10^{20} p/m^2. The samples were exposed to a deuterium plasma with a mean ion energy of 10 eV/D to a fluence of 1×10^{25} D/m^2 at a sample temperature of 450 K. The dashed lines represent the onset of significant changes in the defect structure detected by PALS. Their position is in the middle of two examined annealing temperatures with the higher temperature corresponding to the temperature when significant changes are visible.

The evolution of TDS spectra with annealing temperature was unsystematic, presumably due to significant contributions of HD, HDO, and D_2O molecules. Therefore, they are not shown here and can be found in appendix D. The same problem occurred in measurements of samples damaged by MeV electrons; these results are presented in appendix E.

Nevertheless, TDS results indicate that the highest temperature peak of H_2 release from the samples is located near 950 K. This means that in the case of annealing at 1000 K and above all the implanted protium is removed from the samples[4] and it has no further influence on the evolution of the defect structure and on the results of PALS measurements.

4. During annealings the background pressure is below 10^{-5} Pa, therefore, the absorption of protium from the residual gas by the samples must be negligible.

7.4 Effects of high damage levels

The experiments described above were intended to study the annealing and clustering characteristics of vacancies in tungsten. For this, the used damage level was low (5.8×10^{-3} dpa). However, several orders of magnitude higher damage levels are expected in ITER and DEMO [2, 12, 13]. Hence, it is important to understand how the results obtained at low damage levels can be extrapolated to high damage levels. Due to the quite low damaging rate by protons, reaching damage levels of the order of dpa is not feasible. However, this can be easily achieved by damaging with self-ions. As was already discussed in section 3.4, in the case of damaging by heavy ions not only isolated Frenkel pairs are formed as primary defects, but also vacancy clusters. This situation is close to that expected in the case of bombardment with 14 MeV neutrons, thus, the use of self-ions for simulating the effects of high damage levels is reasonable.

Two tungsten single crystals were damaged by 9 MeV tungsten ions to a fluence of 3×10^{18} W/m^2 corresponding to a maximum damage level of 1.1 dpa, which is above the onset of saturation of the concentration of deuterium-decorable defects [96, 97]. This ion energy was chosen in order to have a similar depth range of the damaged zone (shown in Fig. 7.9) as in the case of damaging with 200 keV protons. One of the targets was post-irradiation annealed at 1800 K for 15 min, when complete recovery of radiation defects at a low damage level was observed. To unravel the evolution of the defect structure with the damage level, one sample was irradiated to a fluence of 3×10^{15} W/m^2 corresponding to a maximum damage level of 10^{-3} dpa, which is even lower than that in experiments with damaging by protons. The samples were analysed with PALS at positron implantation energies of 16 keV and 18 keV. Fig. 7.8 shows the comparison of the measured spectra. The effects of increasing damage level and annealing are apparent.

The measured lifetime spectra were decomposed into three components. In the sample damaged to 10^{-3} dpa the positrons predominantly (80 %) annihilate at defects with a lifetime near 190 ps, i.e., single vacancies. There is a 5 % contribution of the longest lifetime (500 ps) representing annihilation at large vacancy clusters. In the sample damaged to 1.1 dpa, the intensity of the second lifetime is the same as in the sample damaged to 10^{-3} dpa while its value increases to 215 ps representing a mixture of positron annihilation at vacancies and small vacancy clusters. The intensity of the longest lifetime near 460 ps increases to 14 % indicating a larger fraction of big vacancy clusters at high damage levels. This can be explained both by the overlap of defects produced in different cascades and by the accumulation of large clusters produced directly in displacement cascades, as predicted by molecular dynamics simulations [147]. Accordingly, with increasing damage level the average positron lifetime increases from 184 ps to 240 ps.

Already from the raw data shown in Fig. 7.8 it is evident that a full recovery of defects does not happen after annealing of the 1.1 dpa damaged sample

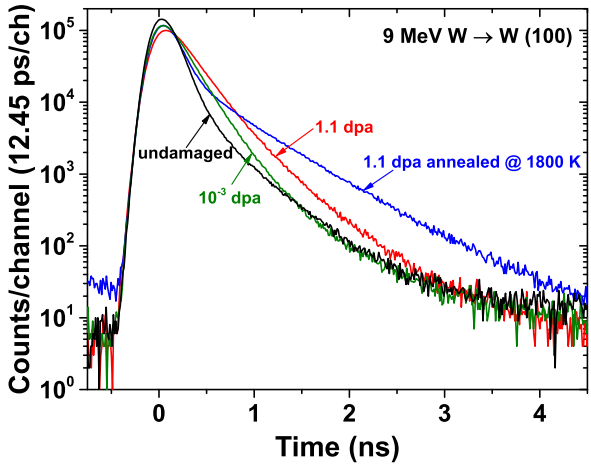

Fig. 7.8: Positron lifetime spectra at 18 keV positron implantation energy for tungsten (100) single crystals damaged by 9 MeV tungsten ions to fluences of 3×10^{15} W/m^2 (10^{-3} dpa) and 3×10^{18} W/m^2 (1.1 dpa). The spectrum of the sample damaged to 3×10^{18} W/m^2 and post-irradiation annealed at 1800 K for 15 min is also shown.

at 1800 K. Near 60 % of positrons annihilate from the delocalized bulk state indicating considerable defect recovery. Nevertheless, 26 % of the positrons annihilate in defects with a lifetime near 580 ps corresponding to large vacancy clusters with surfaces probably partially decorated with impurities, as was discussed in the previous section. The formation of voids with an average diameter of 4 nm (containing several thousand vacancies) already after post-irradiation annealing at 1673 K of tungsten damaged by 2 MeV self-ions to a fluence of 1×10^{18} W/m^2 was observed by TEM [85]. In addition, 14 % of positrons annihilate in defects with a lifetime of 260 ps corresponding to clusters containing around four vacancies [126].

All these samples were exposed to a deuterium plasma under the same conditions as the samples damaged by protons. SEM examinations of all samples do not detect the presence of any surface modifications, in contrary to the samples damaged by protons. Hence, damaging with protons introduces defects acting as nucleation sites for the protrusions that are not provided (or provided in an insufficient quantity) by damaging with self-ions.

Fig. 7.9 shows the measured deuterium depth distributions. The maximum deuterium concentration in the sample damaged to 10^{-3} dpa (not shown in the graph) is 3.3×10^{-4} at. fr. and increases to 1.2×10^{-2} at. fr. at 1.1 dpa. The latter is comparable with that previously reported for a polycrystalline tungsten damaged to a similar level [96], indicating that the saturation concentration of deuterium-decorable radiation defects is almost independent of the used tungsten grade. Post-irradiation annealing at 1800 K of the sample damaged to 1.1 dpa results in a decrease of the maximum deuterium concentration to 8.6×10^{-4} at. fr., which is still more than two orders of magnitude larger

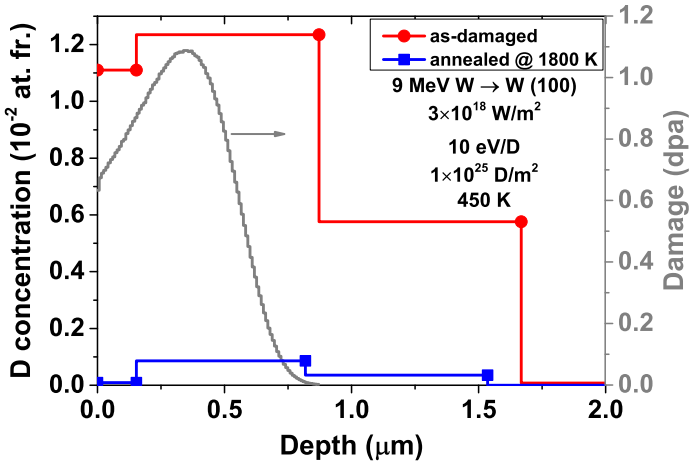

Fig. 7.9: Deuterium concentration profiles in tungsten (100) single crystals damaged by 9 MeV tungsten ions to a fluence of 3×10^{18} W/m^2 (1.1 dpa, as-damaged and post-irradiation annealed at 1800 K for 15 min) and then exposed to a deuterium plasma with a mean ion energy of 10 eV/D to a fluence of 1×10^{25} D/m^2 at a sample temperature of 450 K. The damage profile created by 9 MeV tungsten ions (grey line) calculated using SRIM is also shown.

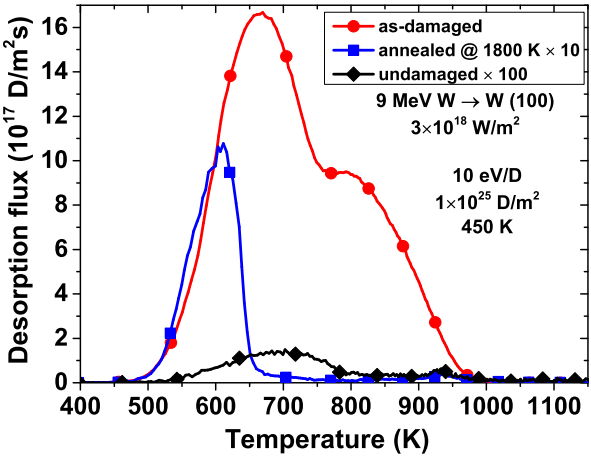

Fig. 7.10: TDS spectra of D_2 molecules from tungsten (100) single crystals damaged by 9 MeV tungsten ions to a fluence of 3×10^{18} W/m^2 (1.1 dpa, as-damaged and post-irradiation annealed at 1800 K for 15 min) and then exposed to a deuterium plasma with a mean ion energy of 10 eV/D to a fluence of 1×10^{25} D/m^2 at a sample temperature of 450 K. Note that the spectra of the sample annealed at 1800 K and of an undamaged sample are enlarged by factors of 10 and 100, respectively.

compared with that in an undamaged single crystal and is also higher compared with that in the sample damaged to 10^{-3} dpa.

The TDS spectrum from the sample damaged to 1.1 dpa (Fig. 7.10) exhibits a broad peak with a maximum at 670 K and a broad shoulder at 800 K. The

annealed specimen exhibits one dominant release peak near 600 K and a faint peak near 940 K. A dominant peak near 600 K was previously observed in tungsten containing voids [148]. Hence, this peak likely corresponds to the release of D_2 gas stored inside very large vacancy clusters (voids) detected by PALS; the peak near 940 K might correspond to deuterium trapped at internal surfaces of these clusters and/or trapped in small vacancy clusters (that are also present in the sample). The fact that the position of the major peak is close to that for deuterium release from vacancies (see Fig. 6.3) is explained by the close values of detrapping energies: 1.56 eV for a deuterium in a vacancy (see chapter 6) and 1.43 eV for D_2 molecules inside voids (see section 3.3.2).

7.5 Discussion

There are five major defect recovery stages in irradiated metals linked either with the onset of defect mobility (vacancy, interstitial or their clusters) or with the dissociation of defect clusters and defect-impurity complexes (see section 3.4). Although the reported onset temperatures of the various stages have some scatter, it should be stressed that these temperatures are not universal physical quantities since they depend on the used annealing scheme, on the concentration of defects and their depth distribution [84]. The corresponding fundamental quantities are the activation energies for the respective processes.

In tungsten the recovery stage I, corresponding to the onset of self-interstitial mobility, and stage II, attributed to the onset of migration and/or dissociation of small interstitial clusters and interstitial-impurity complexes, start already below room temperature [84]. Therefore, they are not relevant for fusion applications and were not examined in the present study. Recovery stage III starts above 500 K and is nowadays commonly attributed to the onset of vacancy mobility. This has been observed by the positron annihilation techniques (PALS and DBS) [87–89] as the beginning of the formation of vacancy clusters driven by vacancy mobility. The present experimental results support this interpretation and the intensive formation of vacancy clusters observed after annealing at 700 K corresponds to the stage III.

The decrease of the concentration of vacancy clusters after annealing at 1300 K and higher temperatures is accompanied by their coarsening resulting in the formation of voids visible by TEM [146]. This corresponds to the recovery stage V. However, no indication of the intermediate stage (IV) is visible in the present experiments, which means that only little changes of open-volume defects occur during it. The nature of this stage is still under debate, but it is usually attributed to migration and/or dissociation of vacancy-impurity complexes.

The sizes of vacancy clusters at various annealing temperatures determined in the present experiments can be compared with estimations of the thermal stability of clusters of different sizes. Fig. 7.11 summarizes the results of

atomistic calculations of the vacancy binding energy to a cluster as a function of its size reported in [149–154]. Despite the differences in absolute values, all the calculations indicate that the vacancy binding energy to a cluster non-monotonically increases with its size and has several local maxima. Assuming that the cluster thermal dissociation occurs via "evaporation" of vacancies from it, this process can be considered as first-order Arrhenius-like with a rate constant $R_{diss} = \nu_0 \exp(-E^{VC}_{diss}/(k_B T))$, where ν_0 is the attempt frequency and $E^{VC}_{diss} = E^{VC}_b + E^V_m$ is the dissociation energy of the cluster, which is equal to the sum of the vacancy binding energy to the cluster E^{VC}_b and the activation energy for the vacancy diffusion E^V_m. In the case of a constant temperature during annealing, the decrease of the concentration of clusters of a particular size with time will be expressed by an exponential decay law. Hence, during the time t_{ann} the concentration of clusters will be reduced by e times if $R_{diss} t_{ann} = 1$. This can be used as a criterion to estimate the maximum vacancy binding energy corresponding to a significant dissociation of clusters at a given annealing temperature T_{ann}:

$$E^{VC}_{b,max} = k_B T_{ann} \ln(\nu_0 t_{ann}) - E^V_m. \tag{7.1}$$

In the present estimations the attempt frequency ν_0 was assumed to be the same as that for the vacancy diffusion of 5.5×10^{12} s^{-1} [155]. Both experimentally determined and calculated values of the activation energy for the vacancy migration in tungsten E^V_m are around 1.7 eV [84, 153].

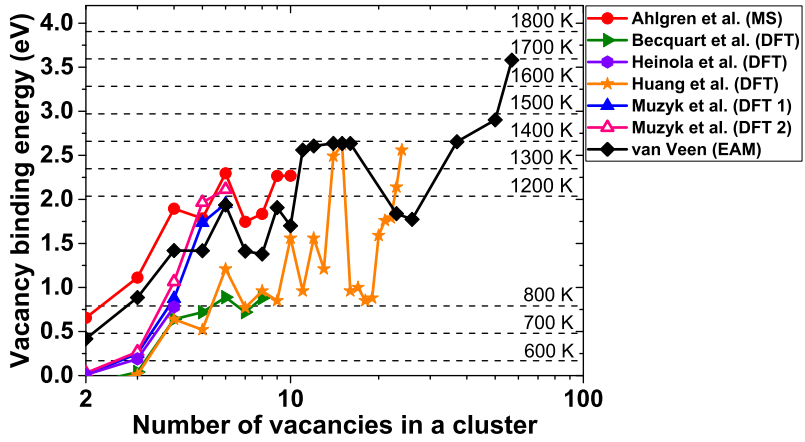

Fig. 7.11: Binding energies of a single vacancy to a vacancy cluster as a function of cluster size obtained by atomistic calculations [149–154]. The dashed lines indicate the maximum binding energy calculated using Eq. 7.1 (assuming $E^V_m = 1.7$ eV and $\nu_0 = 5.5 \times 10^{12}$ s^{-1}) at which a significant dissociation of clusters is expected during the 15 min annealing at a temperature given above each line.

The results of this estimation are also shown in Fig. 7.11 as horizontal dashed lines, which indicate that the clusters with binding energies larger than the value given by the line should be mostly stable at the temperature indicated

above the line. The present experimental results show that annealing already at 800 K results in a predominant presence of large vacancy clusters (> 30 vacancies). A similar result was also obtained by de Vries [89]. Concurrently, the results of all calculations presented in Fig. 7.11 suggest that clusters with smaller sizes should still be stable at this temperature. Note that the results of DBS measurements by Eleveld and van Veen [87] were interpreted in terms of the vacancy cluster size as a function of annealing temperature based on the considerations given above and this interpretation has been commonly accepted. However, it clearly contradicts to the present experimental findings.

After annealing at 1200 K of samples damaged by 4.5 MeV electrons (see appendix E) large vacancy clusters were detected as well, indicating that these are the most stable configurations at this annealing temperature, irrespectively of damaging species.

There exist two mechanisms explaining the coarsening of vacancy clusters with increasing annealing temperature [156, 157]. The first is the Ostwald ripening mechanism where vacancies are released from small clusters, then migrate and attach to other clusters. Since there exists a competition between the annihilation of vacancies and their retrapping by clusters, large clusters can be formed only when the retrapping probability is sufficiently high (employing high defect concentrations). The second mechanism involves migration and coalescence of small vacancy clusters. Since the presence of mainly single vacancies and small vacancy clusters in the as-damaged samples was detected by PALS, the fact that clusters containing more than 30 vacancies are predominant after annealing at 800 K is difficult to explain in terms of the first mechanism. According to Fig. 7.11, at 800 K it is energetically unfavourable for small clusters of certain sizes (which can be still determined by PALS) to dissociate, which is supported by the results of Kinetic Monte Carlo simulations [158]. Hence, it is more likely that in the present experiments the cluster coarsening occurred via the second mechanism. Unfortunately, very little is known about the mobility of vacancy clusters in tungsten [154, 158].

All the calculations presented in Fig. 7.11 are limited to clusters containing 60 vacancies. The vacancy binding energy to larger clusters can be estimated using the capillary approximation, which assumes that a vacancy cluster containing n vacancies has a spherical shape and its total energy $E_{tot}^{VC}(n)$ is proportional to its surface area [151]:

$$E_b^{VC}(n) = E_f^V + E_{tot}^{VC}(n-1) - E_{tot}^{VC}(n) = E_f^V - \gamma(n^{2/3} - (n-1)^{2/3}), \quad (7.2)$$

where E_f^V is the vacancy formation energy and γ is a proportionality factor. For large n the binding energy asymptotically approaches E_f^V, which can be understood in a way that with increasing cluster size the properties of its surface are approaching those of a free metal surface. It is known that the formation of thermal vacancies in metals predominantly occurs at surfaces, thus, the vacancy formation energy can be considered as an upper limit for the vacancy binding energy to a large cluster. The experimentally determined values of E_f^V

in tungsten are around 3.6 eV [84], while atomistic calculations predict lower values (3.05–3.57 eV) [153]. All these values lead to the conclusion that very large vacancy clusters (voids) should be unstable at 1800 K (see Fig. 7.11). The presence of voids in the sample annealed at 1800 K after damaging to 1.1 dpa (while this was not observed at 5.8×10^{-3} dpa) can be explained by the large retrapping rates of released vacancies by the clusters (due to their high concentration) impeding reaching the surface or another sink. In this case the clusters are not actually stable, but metastable and larger annealing times (or temperatures) are needed to dissociate them. It is also possible that impurities segregating at the surfaces of the voids during the high temperature annealing, as suggested by PALS measurements, stabilize the voids and higher temperatures are required to dissociate them. For instance, Zakharova et al. [159] observed complete recovery of defects in a tungsten single crystal irradiated by fission neutrons only after annealing at 2340 K.

Such temperatures (above 1800 K) required to completely anneal radiation defects are higher than the expected operation temperature of tungsten PFCs in the ITER divertor during inter-ELM phases of discharges and are also higher than the recrystallization temperature of tungsten. Hence, in ITER and DEMO complete recovery of neutron-induced defects is unlikely under normal operational conditions. Nevertheless, at elevated temperatures thermal detrapping of deuterium from the defects is considerable, which means that the defects will be only partially filled with it [98].

Small vacancy clusters ($\leq$ 10 vacancies) are detected even after annealing at high temperatures, although they should be unstable according to Fig. 7.11. They can be the metastable precursors of large clusters. In addition, they could also be formed during the sample cooling down from the vacancies "evaporated" from large clusters, since in the present experiments the cooling-down to room temperature was not rapid (see Fig. 7.1). It is also possible that these clusters are stabilized via decoration with impurities [154].

Using deuterium as a probe of the defect concentration shows that the decrease of the trapped concentration with annealing temperature generally follows the recovery stages detected by PALS (see dashed lines in Fig. 7.7). However, the details are sometimes different, for example, the average positron lifetime is almost the same after annealing at 800 K and 900 K while the maximum deuterium concentration decreases. This can be because several types of defects contribute to the retention and defects like vacancy clusters can trap multiple deuterium atoms; large clusters (voids) can also be filled with D_2 gas.

Although the TDS results of the present samples are inconclusive, the *in situ* TDS experiments partially reported in the previous chapter and described in more detail in [135] clearly show that annealing at 700 K and higher temperatures results in disappearance of the peak corresponding to the deuterium release from vacancies and appearance of a new higher temperature peak, indicating the growth of vacancy clusters at the expense of vacancies, in line with the results of present PALS measurements.

7.6 Chapter summary

An investigation of the thermal evolution of vacancies and vacancy clusters in single crystalline tungsten in the temperature range 500–1800 K and their influence on deuterium retention has been carried out. The introduction of predominantly Frenkel pairs as primary defects was done by irradiation with 200 keV protons to a low damage level (5.8×10^{-3} dpa). Substantial changes in the defect structure were observed after post-damaging annealing at 700 K and were driven by the onset of vacancy mobility, resulting in their agglomeration into clusters containing on average 13 vacancies. Annealing at 800 K and above resulted in the formation of large clusters containing more than 30 vacancies, a size which cannot be further distinguished by PALS. In the temperature range of 800–1200 K the concentration of open-volume defects practically did not change, whereas at temperatures of 1300 K and above recovery of the defects started and is likely accompanied by a further coarsening of the vacancy clusters. The complete removal of radiation defects was observed after annealing at 1800 K. The determined sizes of the clusters were larger than those expected from thermal stability considerations, therefore, it is suggested that the coarsening of clusters is mainly driven by the mobility of small clusters.

The concentration of trapped deuterium as a function of post-damaging annealing temperature is the result of an interplay between the reduction of the defect concentration and trapping of multiple deuterium atoms in vacancy clusters and of D_2 molecules in large vacancy clusters (voids). Its behaviour with annealing temperature generally followed the recovery stages determined by PALS.

Increase of the damage level causes the shift of the complete defect recovery temperature to higher values. Annealing at 1800 K of the sample damaged to 1.1 dpa by 9 MeV tungsten ions resulted in the formation of very large vacancy clusters (voids). Their persistence was attributed to the high retrapping rate of vacancies dissociated from voids by other voids. The trapped deuterium concentration in this sample was only about one order of magnitude smaller than in the as-damaged sample. The TDS spectrum exhibited one dominant peak located in the same temperature range as deuterium release from vacancies and corresponds to the release of D_2 gas stored inside voids.

Damaging with protons facilitated the formation of protrusions under deuterium plasma exposure. Post-damaging annealing at temperatures starting from 550 K allowed suppressing their appearance. Damaging by self-ions both to low and high damage levels did not lead to the formation of protrusions.

Chapter 8

Deuterium interaction with dislocations in tungsten

While the previous two chapters were devoted to investigations of deuterium interaction with radiation-induced defects in tungsten, this chapter will be focused on deuterium interactions with dislocations, which are one of the typical intrinsic defects in tungsten. Large densities of dislocations are present already in as-manufactured tungsten, and additional dislocations can be introduced in tungsten PFCs during a plasma operation via plastic deformation caused by transient heat loads [5, 8], as well as by high concentrations of solute hydrogen [15, 16]. There is still no consensus regarding the contribution of dislocations to hydrogen inventory in tungsten (see section 3.3). This chapter presents the results of experiments devoted to investigations of deuterium retention in tungsten samples with various dislocation densities produced by tensile plastic deformation to different strains at two different temperatures.

8.1 Experimental details

Hot-rolled polycrystalline tungsten with a purity of 99.97 wt. % manufactured by Plansee was used. This tungsten grade originates from a different manufacturing batch compared with the grade used in chapter 5 and the grade previously used at IPP; however, all these grades have the same production route and purity (listed in table C.1 in appendix C). A number of flat dog bone-shaped tensile specimens with an overall length of 120 mm and the gauge section dimensions of $50 \times 13 \times 0.8$ mm^3 were cut by spark erosion from a single plate of the material. In order to minimise the initial density of dislocations and grain boundaries, the tensile samples were recrystallized at 1873 K for 1 h in vacuum (0.02–0.05 Pa) at Forschungszentrum Jülich (Germany). To produce specimens with various dislocation densities, interrupted tensile tests

were carried out on a tensile testing machine equipped with a furnace, which is feedback-controlled by a thermocouple attached to the sample, at SCK • CEN (Belgium). The tensile tests were performed at sample temperatures of 573 K and 873 K in air. The displacement rate was 0.2 mm/min (corresponding to a strain rate of 6.7×10^{-5} s^{-1}), and the achieved engineering strains ranged from 3 % to 38 %. The whole gauge section of each sample was homogeneously deformed since no local necking was formed even at the highest strain applied, as shown in Fig. 8.1.

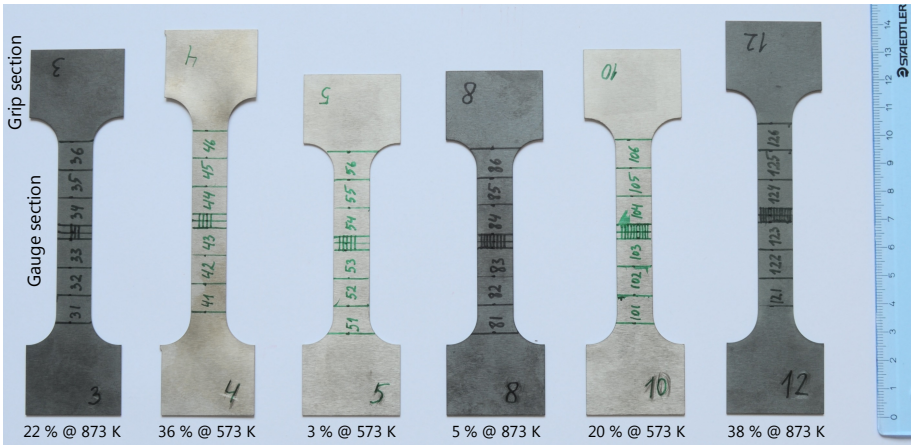

Fig. 8.1: Tensile tungsten specimens after deformation to various strains at two different temperatures (573 K and 873 K). The lines represent the cutting scheme of the tensile specimens to produce samples for TEM examinations and deuterium plasma exposures. Note that the specimens deformed at 873 K appear darker compared with the specimens deformed at 573 K due to thicker oxide layers developed during the tests.

The samples for deuterium retention studies with linear dimensions of 10×10 mm^2 were cut by spark erosion from the gauge sections of the tensile specimens as marked in Fig. 8.1. The reference (undeformed) samples were cut from the grip sections (which did not experience deformation during the tests) of the tensile specimens. The obtained samples were first grinded with a set of SiC sandpapers with decreasing grit sizes (up to P4000), which resulted in the removal of the oxide layer developed during the tensile test. Then they were electrochemically polished to a mirror-like finish in a 1.5 wt. % NaOH aqueous solution at a voltage of 19 V for 15 min, which allowed to remove the distorted near-surface layer introduced during grinding [132]. Afterwards, the samples were successively cleaned in an ultrasonic bath with acetone, isopropanol, and a high-purity acetone and then rinsed in deionized water.

In addition, two specimens with linear dimensions of 2.4×10 mm^2 were cut from the central part of each gauge for TEM investigations. These samples were first grinded from both sides to reduce their thickness to 100–130 μm and then cut into pieces (2.4×2.4 mm^2) with a diamond wire saw. Afterwards, they

were glued on 3 mm copper TEM grids with an aperture of 1 mm. Finally, the TEM specimens were electrochemically thinned from both sides in a 1.5 wt. % NaOH aqueous solution at a voltage of 30 V until a small hole appeared in the centre of the sample. The specimens were investigated with a JEOL 3010 TEM operating at 300 kV at SCK • CEN by A. Dubinko [160]. The TEM images were acquired in bright field imaging mode providing a good contrast of dislocation lines. The average dislocation density defined as the total length of dislocation lines per unit volume was determined using Ham's interception method [161]. In this method, a circle is drawn randomly in a TEM image and the number of intersections with dislocations is counted using the Gatan DigitalMicrograph 3 software. The dislocation density is then computed as $\rho = 2N/(Lt)$, where N is the number of intersections of the circle with dislocation lines, L is the length of the circle, and t is the local sample thickness determined from the convergent beam electron diffraction (CBED) pattern analysis. Several calculations at different regions of the sample were carried out in order to obtain the average value of the dislocation density.

In order to load the introduced defects with deuterium, samples of all types were simultaneously exposed to a low-flux deuterium plasma in the PlaQ plasma device (see section 4.1.1 for the description). The exposures were carried out at sample temperatures of 370 K and 450 K to a fluence of 2.4×10^{25} D/m^2.

8.2 Material characterization

8.2.1 Electron microscopy

Fig. 8.2(a) shows a SEM image with BSE contrast (which is sensitive for the misorientation between grains) of a surface of the recrystallized undeformed tungsten. The material has large isotropic grains with dimensions up to 50 μm, which is confirmed by the examination of the sample cross-section. The grains show uniform grey levels and sharp contours typical for recrystallized tungsten [14], which demonstrates that the applied annealing procedure was effective for elimination of the grain distortion introduced during material manufacturing. A TEM image of the recrystallized tungsten is shown in Fig. 8.3(a). The annealed material still has some dislocations appearing mostly as short and straight isolated lines. Their spatial distribution is inhomogeneous: There are regions where groups of dislocations are present (as in the upper left corner of Fig. 8.3(a)), as well as areas with almost no dislocations. The measured average dislocation density in the grain interior is $(5.1 \pm 1.7) \times 10^{12}$ m^{-2}, which agrees with the values reported by Manhard et al. [14] for the same type of material after recrystallization.

Figs. 8.2(b) and (e) show BSE SEM images of the surfaces of the recrystallized tungsten deformed to the lowest strains: 3 % at 573 K and 5 % at 873 K, respectively. The sizes of the grains are the same as in the undeformed material.

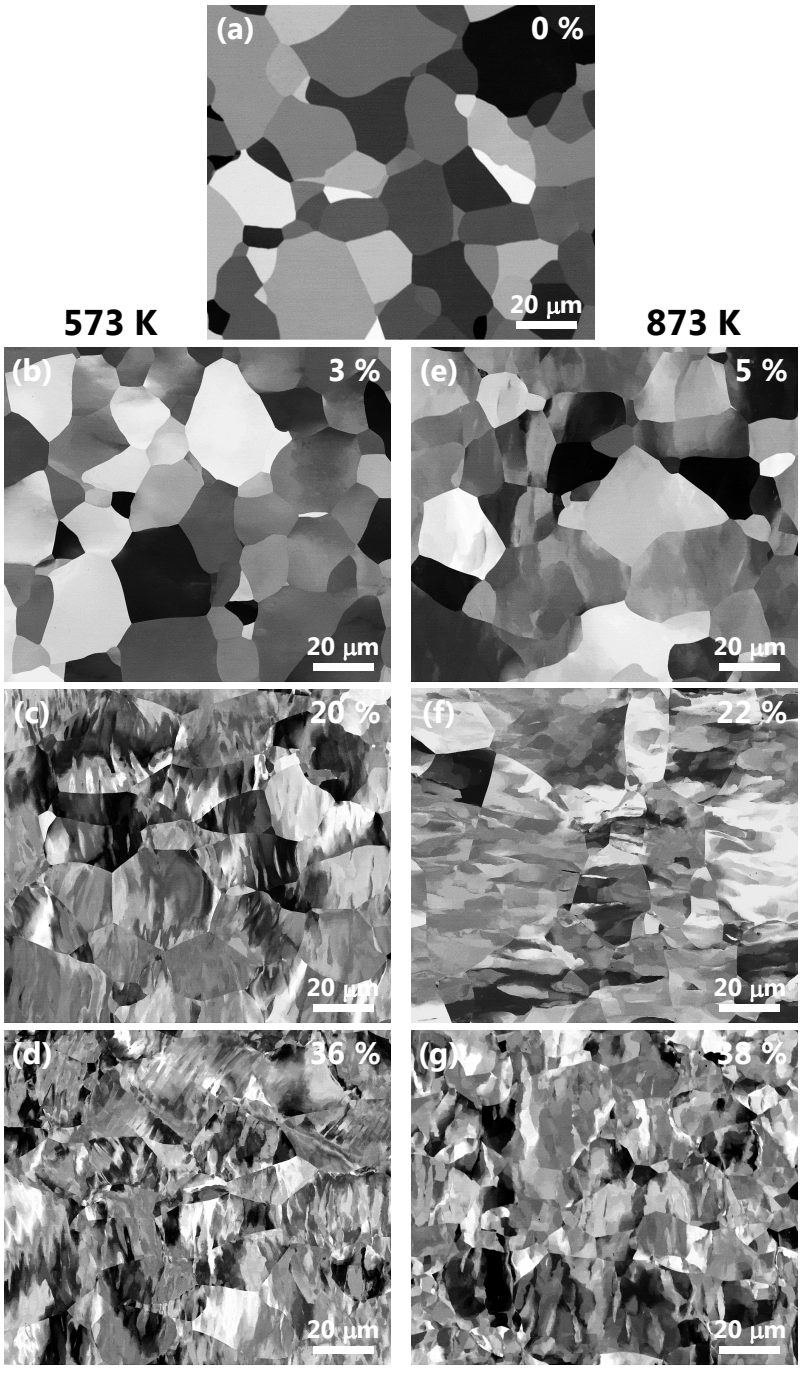

Fig. 8.2: SEM images (BSE contrast) of the surfaces of recrystallized tungsten: (a) undeformed; (b) deformed to 3 % strain at 573 K; (c) deformed to 20 % strain at 573 K; (d) deformed to 36 % strain at 573 K; (e) deformed to 5 % strain at 873 K; (f) deformed to 22 % strain at 873 K; (g) deformed to 38 % strain at 873 K. All images are taken parallel to the tensile loading direction.

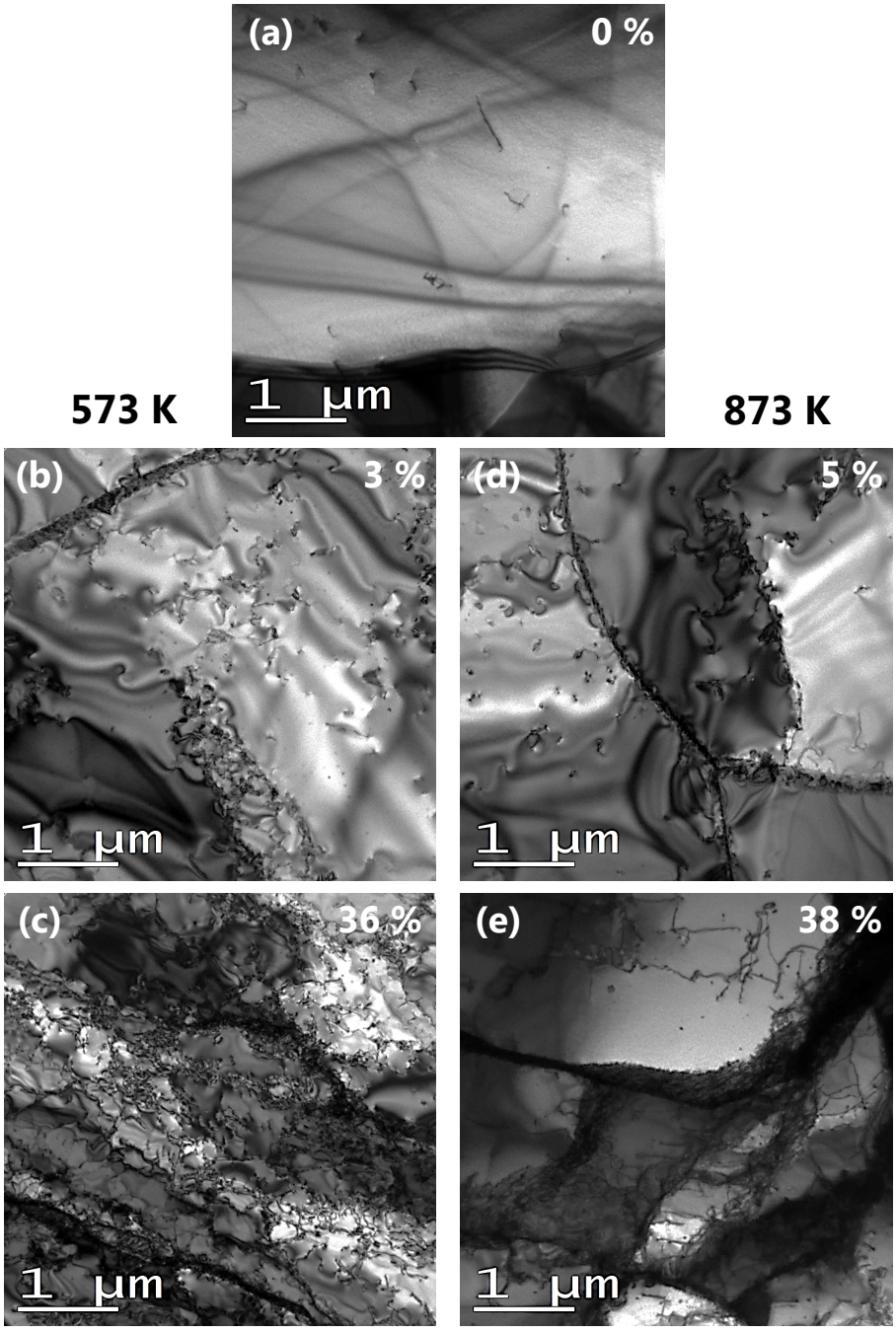

Fig. 8.3: TEM bright field images of the recrystallized tungsten: (a) undeformed; (b) deformed to 3 % strain at 573 K; (c) deformed to 36 % strain at 573 K; (d) deformed to 5 % strain at 873 K; (e) deformed to 38 % strain at 873 K. The broad blurred dark lines in the images are artefacts of the TEM specimen preparation and correspond to bend contours and thickness fringes, which appear due to bending of the specimens and non-uniformity of their thicknesses, respectively.

However, most of the grains have a non-uniform grey level indicating the presence of lattice distortions, which affect channelling and backscattering of the incident electrons. This effect is more pronounced for the sample deformed to 5 % strain at 873 K. Figs. 8.3(b) and (d) show TEM images of tungsten deformed to 3 % strain at 573 K and 5 % strain at 873 K, respectively. The average length of dislocations in the grain interiors is larger compared with the undeformed material for both samples. Furthermore, in the deformed samples not only isolated dislocation lines are present, but also tangles of dislocations. In tungsten deformed to 3 % strain at 573 K the observed dislocation networks are more dense and tangled compared with those observed in the material deformed to 5 % strain at 873 K. The presence of dislocation pile-ups near grain boundaries is also visible. The latter can be explained by the influence of two factors: grain boundaries act as obstacles for dislocation motion, resulting in the formation of dislocation pile-ups in their vicinity, and they can also act as dislocation sources [39]. Similarly to the undeformed material, the lateral distribution of dislocations in both specimens is inhomogeneous. Some insight into the spatial distribution of dislocations can be gained from the stitched TEM images shown in appendix F. The average dislocation densities (in the grain interior) are almost the same in both materials: $(1.4 \pm 0.1) \times 10^{13}$ m^{-2} in the sample deformed to 3 % strain at 573 K and $(1.2 \pm 0.3) \times 10^{13}$ m^{-2} in the sample deformed to 5 % strain at 873 K.

With increasing strain (20 % at 573 K and 22 % at 873 K) the original grains are still recognizable in the BSE SEM images (Figs. 8.2(c) and (f), respectively) and their dimensions are almost the same as in the undeformed material. However, in the grain interior many regions with different grey levels are present indicating that the original grains have subdivided into misoriented regions (resulting in different channelling contrast in BSE images), i.e., grain fragmentation took place. Unfortunately, TEM analysis of these samples has not been done.

At the highest applied strains (36 % at 573 K and 38 % at 873 K) the grain fragmentation is more severe, which is manifested by a stronger contrast between different misoriented regions within grains and by a higher number of misoriented regions within a single grain (Figs. 8.2(d) and (g), respectively). Furthermore, it is more difficult to recognize the outlines of the original grains. TEM investigations of the material deformed to 38 % strain at 873 K (Fig. 8.3(e)) confirm the presence of grain fragmentation, i.e., the formation of new low-angle grain boundaries via the arrangement of dislocation tangles in walls (formation of the so-called "cellular substructure") [39]. In fact, it is not easy to distinguish visually between the original high-angle grain boundaries with dense dislocation pile-ups in their vicinity and the newly formed dislocation walls. The increase of the dislocation density inside the grains is also apparent and most of the dislocations are tangled. Nevertheless, still some regions nearly free of dislocations are present in the grain interior. In the material deformed to 36 % strain at 573 K the formation of a cellular substructure is also visible,

but the thicknesses of the dislocation walls are smaller compared with those observed in the sample deformed at 873 K, and more dislocations are present in the cell interior. It has been also observed in other metals that deformation at lower temperatures results in more homogeneous dislocation distribution [39]. The measured average dislocation densities (in the grain interior) are again almost the same in both materials: $(2.1\pm0.3)\times10^{14}$ m^{-2} in the sample deformed to 38 % strain at 873 K and $(2.2\pm0.3)\times10^{14}$ m^{-2} in the sample deformed to 36 % strain at 573 K. These dislocation densities are comparable with the dislocation density in stress-relieved hot-rolled tungsten of $(3.2 \pm 1.7) \times 10^{14}$ m^{-2} [14] and with the dislocation (both lines and loops) density in recrystallized tungsten damaged by self-ions to 2.3 dpa of 5.2×10^{14} m^{-2} [162]. Note that Manhard et al. [14] counted not only dislocations in the grain interior (like in the present work), but also dislocation pile-ups near grain boundaries and dislocation walls.

Previous investigations of the plastic deformation at 873 K of double forged recrystallized tungsten reported in [160, 163] revealed that the observed dislocation lines in the non-deformed and the 5 % deformed material are screw dislocations with a Burgers vector $\mathbf{b} = (1/2)\langle111\rangle$, which are the typical dislocations in bcc metals [39]. The dislocation tangles observed in highly-deformed samples (above 20 % strain) contain both screw and edge segments.

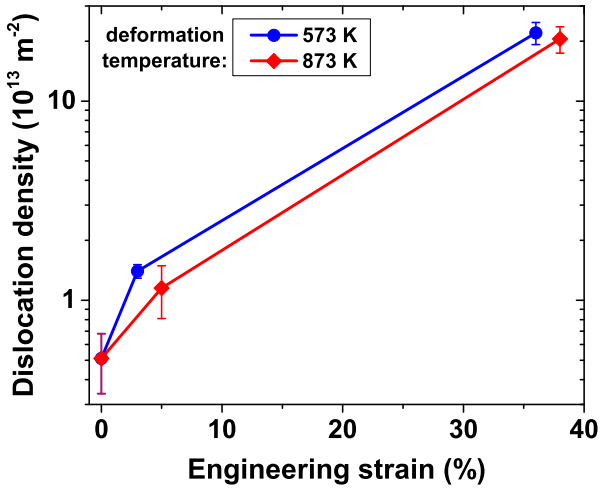

Fig. 8.4: Average dislocation density in the grain interior measured by TEM as a function of engineering strain in the recrystallized tungsten deformed at 573 K and 873 K.

The evolution of the dislocation density versus the applied strain measured by TEM is summarized in Fig. 8.4. As previously mentioned, when measuring the dislocation density the intention was to study its evolution in the grain interior. Hence, regions containing dislocation pile-ups near grain boundaries and dislocation walls were excluded from the examination. As can be seen, the

dislocation density increases non-linearly with the strain: The growth rates at low strains are lower compared with those at high strains.

In conclusion, the initial contribution to the plastic deformation originates from the creation of screw dislocations. With increasing strain, more dislocations are produced and during their movement they can intersect with each other and form tangles. In addition, they can also reach high-angle grain boundaries and form pile-ups near them. At even larger strains the transformation of tangles into dislocation walls occurs, resulting in the formation of a cellular substructure (grain fragmentation).

8.2.2 Positron annihilation analysis

All types of samples were analysed by PALS at 16 keV and 18 keV positron implantation energies. The effect of deformation temperature and strain is evident already from the raw lifetime spectra shown in Fig. 8.5.

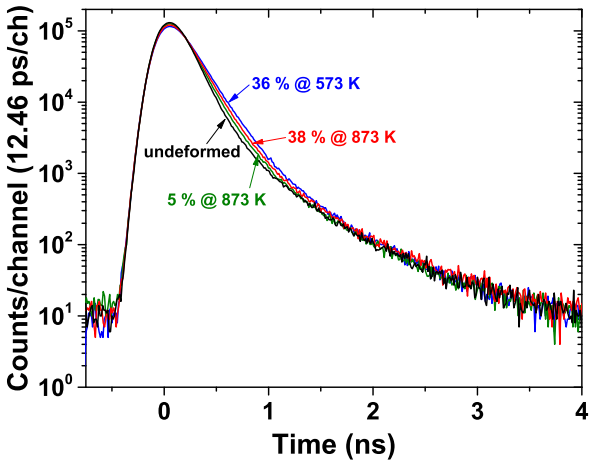

Fig. 8.5: Positron lifetime spectra at 18 keV positron implantation energy for recrystallized tungsten deformed to various strains at two different temperatures (573 K and 873 K).

All measured lifetime spectra were decomposed into three components. Since the positron implantation profiles at 16 keV and 18 keV are almost identical and the defect depth distributions are expected to be homogeneous, in order to reduce the statistical error due to scatter in the data the mean values of both lifetimes and intensities obtained at these two energies will be used in the following discussion. Fig. 8.6 shows the results of the deconvolution. The spectrum of the undeformed sample is dominated by the shortest lifetime component (reduced bulk lifetime), while the second lifetime of 170 ps has a 30 % contribution. With increasing strain the intensity of the second lifetime increases non-linearly at both deformation temperatures: The growth rate is higher at low strains. At intermediate and highest strains the intensity of

the second lifetime component is higher after deformation at 573 K. Its value, however, stays near 170 ps for both deformation temperatures. The longest lifetime in all samples varies in the range of 490–530 ps and likely represents annihilation at voids in the material; its intensity is around 5 % for all samples. The average positron lifetime also increases non-linearly with strain and its increase rate at low strains is higher compared with that at high strains. At intermediate and highest strains the average lifetime is larger in the samples deformed at 573 K.

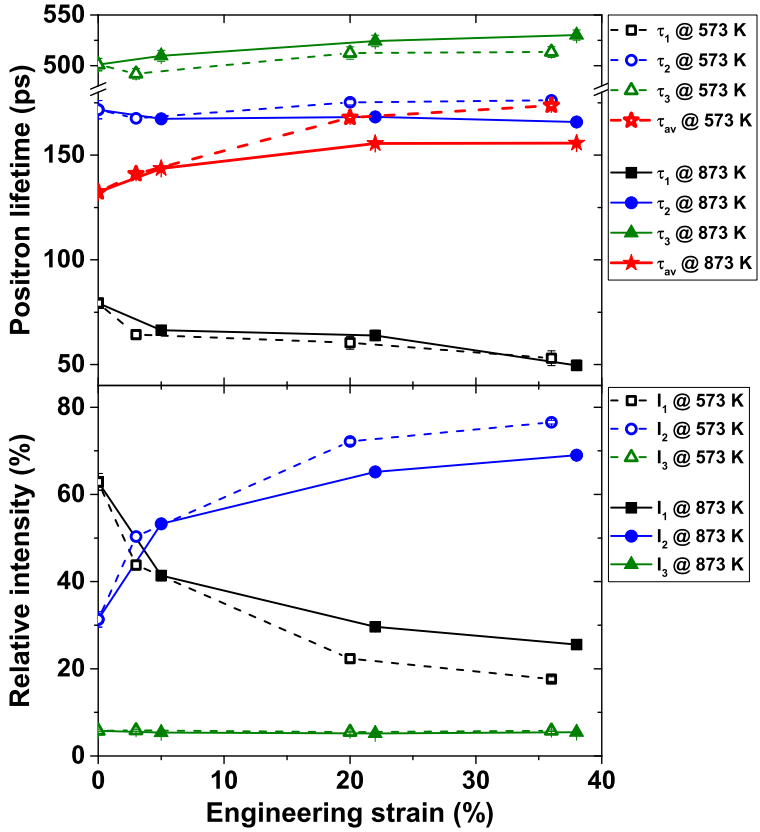

Fig. 8.6: Positron lifetimes (upper panel) and their relative intensities (lower panel) as a function of engineering strain in the recrystallized tungsten deformed at 573 K and 873 K. The shown values are averaged over the decomposition results at 16 keV and 18 keV positron implantation energies.

The second lifetime of 170 ps is shorter than that for positrons trapped in single vacancies of around 200 ps (see chapter 7). A similar situation has been observed in several plastically-deformed metals [125], including tungsten [164]. However, the nature of the corresponding positron trapping sites is still under debate, as summarized in [165, 166]. Some authors reported that a dislocation line itself is only a shallow trap for positrons and the theoretically calculated positron lifetimes at dislocations are almost the same as those in the

bulk. Concurrently, a positron trapped at a dislocation can diffuse along its line and eventually become trapped at a much deeper trap associated with the dislocation. The following traps were suggested: either jogs[1] at the dislocation line or vacancies either trapped in the stress field around the dislocation line or attached to the dislocation line, which forms a pair of jogs with a spacing of one interatomic distance. Jogs on dislocations can be formed when two moving dislocations intersect. Vacancies are also supposed to be created during plastic deformation with the help of two mechanisms [39, 164–166]. First, when two edge dislocations with opposite Burgers vectors meet and their glide planes are separated by one or a few atomic distances, during their annihilation a row of vacancies will be created. Second, movement of a screw dislocation with a jog results in the creation of a row of either vacancies or interstitial atoms, and the creation of vacancies is favoured due to their lower formation energy.

However, some researchers reported that a dislocation line itself can act as a strong trap for positrons. DFT calculations by Staikov and Djourelov [144] predict positron lifetimes for $\mathbf{b} = \langle 100 \rangle$ edge and $\mathbf{b} = (1/2)\langle 111 \rangle$ screw dislocations in tungsten of 161 ps and 130 ps, respectively. The calculated lifetimes for vacancies attached to edge and screw dislocations cores are 192 ps and 188 ps, respectively (the lifetime at a single vacancy is 193 ps).

8.3 Deuterium retention

8.3.1 Plasma exposure at 370 K

A sample temperature of 370 K was chosen because it is lower than the first deuterium release peak in TDS spectra from tungsten (see Fig. 6.1 and references [54, 56, 68]), hence, many of the trapping sites in the material are expected to be able to hold deuterium (at least partially) at this temperature.

Deuterium plasma exposure at this temperature resulted in the appearance of blister-like structures on all types of samples (Fig. 8.7). While on the recrystallized undeformed sample the number density of these features is very low, it noticeably increases already after the smallest used strain at both deformation temperatures. Further increase of the strain results in a rather weak increase of the number density and of the average size of the surface modifications. These features are distributed inhomogeneously across the surface and tend to appear in groups. Note that the observed blister-like structures often have a large aspect ratio, therefore, their contrast on the images is not very high.

The samples with the highest strains (36 % at 573 K and 38 % at 873 K) were examined in detail with SEM. Two types of surface modifications, similar to those observed after high-flux plasma exposures (see chapter 5), are present:

1. Jog is a step of atomic dimension in the dislocation line which is not contained in the glide plane of the dislocation, see Fig. 2.3.

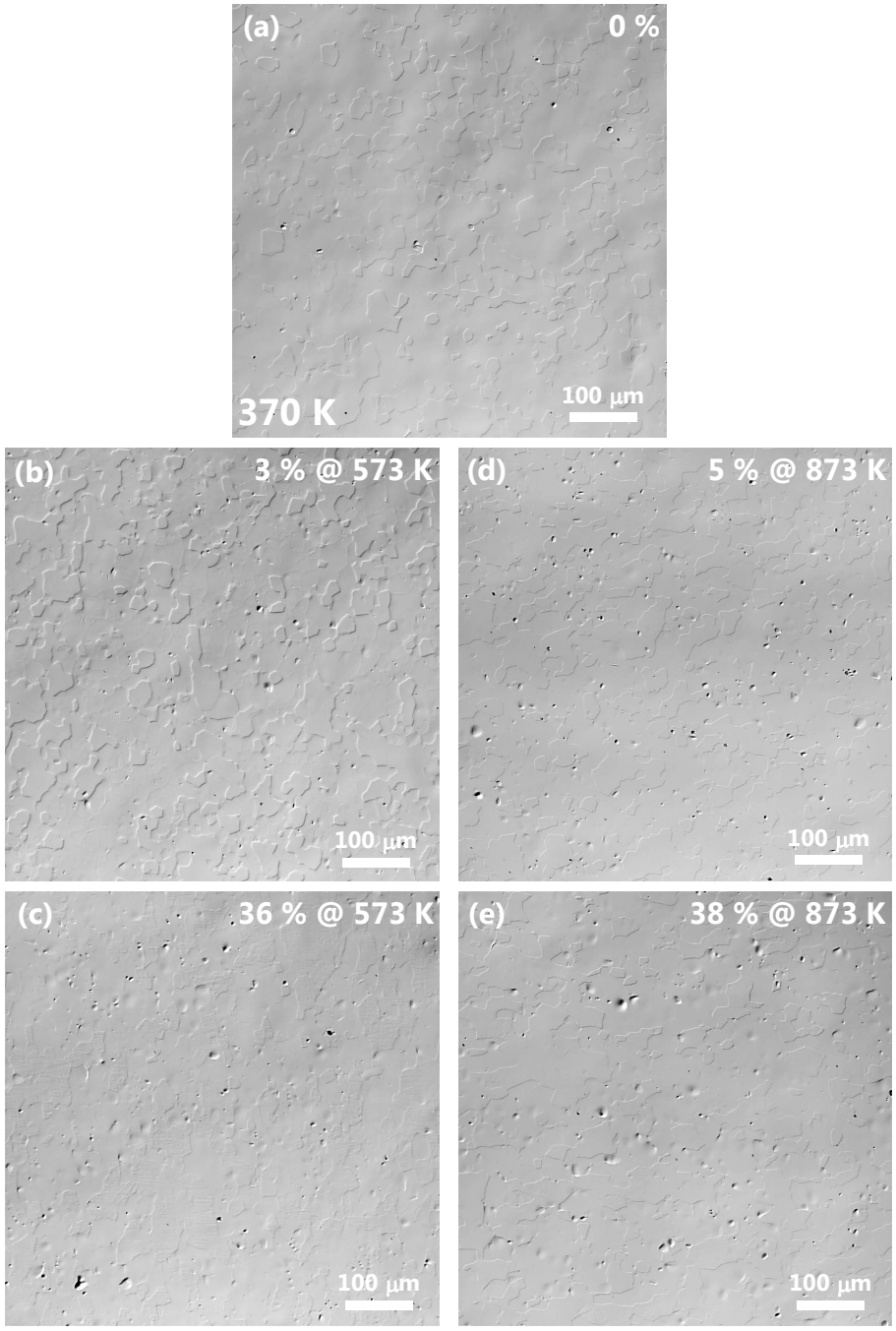

Fig. 8.7: A series of CLSM images of the recrystallized tungsten samples after the exposure to a deuterium plasma with a mean ion energy of 10 eV/D to a fluence of 2.4×10^{25} D/m^2 at a sample temperature of 370 K: (a) undeformed (b) deformed to 3 % strain at 573 K; (c) deformed to 36 % strain at 573 K; (d) deformed to 5 % strain at 873 K; (e) deformed to 38 % strain at 873 K. The visible height differences between the grains are due to the polishing procedure.

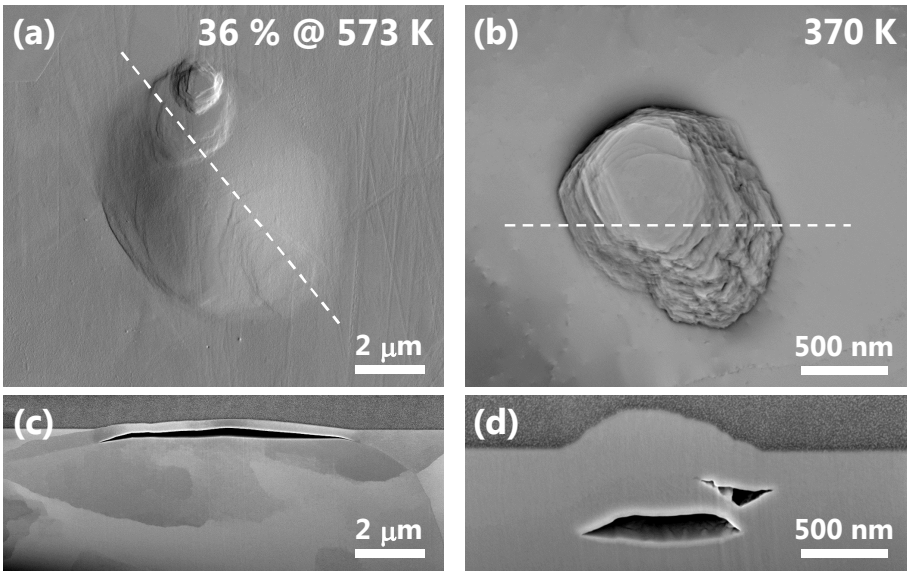

Fig. 8.8: Recrystallized tungsten deformed to 36 % strain at 573 K and exposed to a deuterium plasma with a mean ion energy of 10 eV/D to a fluence of 2.4×10^{25} D/m^2 at a sample temperature of 370 K: A SEM image of a blister with protrusions on its top; (b) a SEM image of a stepped high-dome protrusion; (c) a SEM image of a cross-section approximately at the position indicated by the dashed line in (a); (d) a SEM image of a cross-section approximately at the position indicated by the dashed line in (b). The surfaces in (c) and (d) were protected by a Pt-C layer before cutting. The images were taken after TDS. Note the different scales in (a), (c) and (b), (d).

dome-shaped blisters and stepped flat-topped protrusions. They all have dimensions of a few μm. In total, cross-sections of eight structures were examined, and seven of them (both blisters and protrusions) are formed by intergranular cracks, as illustrated in Fig. 8.8(c). Only one high-dome protrusion is formed by transgranular cracking (Fig. 8.8(d)). The cavities of the investigated structures are located in a depth range of 0.3–2.3 μm. The grain contrast in the cross-sectional SEM images suggests that the intergranular cracks are formed along high-angle grain boundaries, which were initially present in the recrystallized material prior to the mechanical deformation. Since the number density of blisters and protrusions considerably increases already after the deformation to the lowest strain (when no grain fragmentation is visible), the reason for the enhancement of blistering activity after the mechanical deformation is presumably linked with the change of the properties of the high-angle grain boundaries during the deformation. As was shown in section 8.2, already at the lowest applied strain the formation of dislocation pile-ups near grain boundaries takes place. Due to the overlap of the stress fields of the dislocations, a high concentration of stress is expected on the head dislocation in the pile-up [33, 39]. In the presence of additional stresses in the material caused by the high solute deuterium concentration during the plasma exposure, nucleation of a crack at

a grain boundary near to a pile-up may be possible. Such a crack then can be filled with D_2 gas, which pressure then can drive the further cavity growth. In addition, dislocations in the pile-ups themselves can serve as nucleation sites for the blister-like structures. Since one of the investigated protrusions was found to be formed by transgranular cracking, it is also possible that the dislocations (and their tangles) in the grain interior can serve as nucleation sites for the protrusions. Manhard [69] did not observe formation of any surface modifications on recrystallized tungsten after the plasma exposure at 370 K to fluences up to 5×10^{25} D/m^2 at a similar ion energy and flux. In the present study the samples (including undeformed) were polished after the recrystallization (while Manhard did the opposite), which results in the fact that some of the grain boundaries are located close to the surface (as can be seen in Fig. 8.8(c)), which is not the case when the polishing is done before the recrystallization. This might favour the formation of cavities via intergranular cracking near the surface since less material has to be pushed up in order to inflate a blister-like structure.

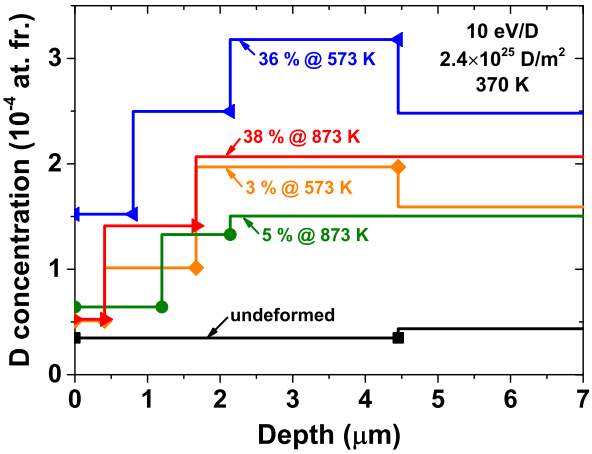

Fig. 8.9: Deuterium concentration profiles in recrystallized tungsten deformed to various strains at two different temperatures (573 K and 873 K) and then exposed to a deuterium plasma with a mean ion energy of 10 eV/D to a fluence of 2.4×10^{25} D/m^2 at a sample temperature of 370 K.

All the deformed samples exhibit non-homogeneous deuterium depth distributions after exposure at 370 K (Fig. 8.9): They all show an enhancement (compared with that near the surface) of the deuterium concentration (up to four times) starting from a depth of around 0.4 μm; some of the samples exhibit a maximum in a certain depth range. In contrast, the undeformed recrystallized sample has a flatter depth profile. The depth range with enhanced deuterium concentration coincides (within the depth resolution of NRA) with the depth region where the cavities of the blisters and protrusions were found. Consequently, similarly to the cases described in chapters 5 and 7, it is reasonable to assume that the increase of the deuterium concentration

with depth is caused by its trapping in the defects introduced together with blisters and protrusions, since the depth distribution of dislocations introduced by mechanical deformation is expected to be (on average) homogeneous through the whole bulk. This hypothesis can explain the dependence of the maximum deuterium concentration on the strain: Already at the lowest strains the deuterium concentration at the maximum is by more than a factor of four higher compared with that in the undeformed sample, which is higher than the measured increase of dislocation density in the grain interior – a factor of two for the sample deformed to 5 % strain at 873 K (see section 8.2). Concurrently, there is a significant increase in the number density of surface modifications on the samples deformed to low strains (Fig. 8.7). Increasing the strain to the maximum value results in up to 1.6 times increase of the maximum deuterium concentration (as compared with that at the lowest strain), which is much smaller compared with the increase of the dislocation density (more than one order of magnitude). This is accompanied by a relatively weak increase (compared with the increase at low strains) of the number density and average size of the surface modifications. Hence, the appearance of blisters and protrusions under the plasma exposure and the dependence of their number on the applied strain hinders revealing the concentration of deuterium trapped by dislocations in these samples.

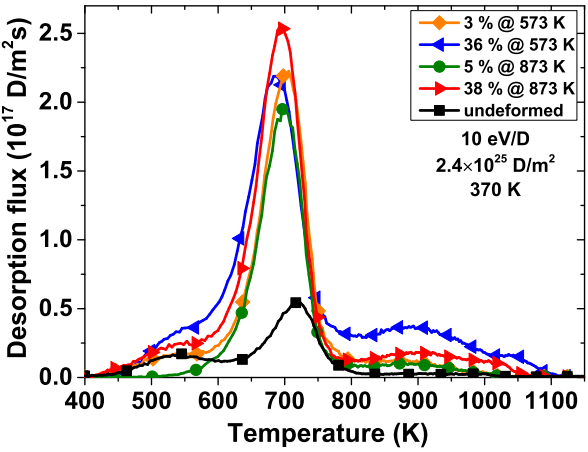

Fig. 8.10: TDS spectra of D_2 molecules from recrystallized tungsten deformed to various strains at two different temperatures (573 K and 873 K) and then exposed to a deuterium plasma with a mean ion energy of 10 eV/D to a fluence of 2.4×10^{25} D/m^2 at a sample temperature of 370 K.

Fig. 8.10 shows the TDS spectra from the corresponding specimens. The spectra consist of a shoulder near 550 K, a major release peak near 700 K, and additional high-temperature shoulders extending up to 1100 K. The amplitude of the 700 K peak noticeably increases in mechanically-deformed samples compared with the undeformed one. Interestingly, its amplitude increases with strain for the samples deformed at 873 K, while almost no difference

is observed for the samples deformed at 573 K. The amplitudes of the high-temperature shoulders also considerably increase with strain, and this effect is more pronounced for the samples deformed at 573 K. The amplitude of the shoulder near 550 K also has a tendency to increase with strain (except for the sample deformed to 5 % strain at 873 K). Note that the slight variations in peak positions among different samples can partially be due to the non-perfect heating ramp reproducibility (see section 4.3.2), therefore, they should not be overinterpreted. The total deuterium inventories in all deformed samples determined by NRA and TDS are in a good agreement[2], indicating that most of the deuterium is trapped within the first 7 μm near the surface. Only in the undeformed sample TDS yields higher retention than NRA[3], indicating deeper deuterium diffusion due to the smaller concentration of trapping sites in the material compared with that in deformed samples. Overall, the spectra exhibit a complicated structure with multiple peaks, which amplitudes depend on the strain and the deformation temperature.

8.3.2 Plasma exposure at 450 K

Increasing the exposure temperature to 450 K makes the trapping sites with low detrapping energies not able to hold deuterium anymore. In addition, this also results in a decrease of the solute deuterium concentration during the plasma exposure, which suppresses the formation of blister-like structures on all samples, as observed by CLSM and SEM. Therefore, the amount of defects induced by the plasma exposure should be rather small (if present at all), so such an exposure can be used as a probe for the presence of deformation-induced defects with high detrapping energies.

After the 450 K exposure, all the samples exhibit almost flat concentration profiles (Fig. 8.11) and the concentrations are considerably smaller compared with those after the exposure at 370 K (compare with Fig. 8.9). This also suggests that the number of defects introduced during the plasma exposure is much smaller compared with the 370 K exposure. The deuterium concentrations in the undeformed sample and the sample deformed to 5 % strain at 873 K are almost identical; the increase of the strain to 38 % results in less than three times increase of the deuterium concentration. In the case of a deformation temperature of 573 K, the effect of increasing strain is more pronounced: There is a 5.5 times difference in concentrations between the lowest and the highest strain. Nevertheless, at both deformation temperatures there is no linear dependence between the dislocation density in the grain interior and the deuterium concentration. Furthermore, the ratio of deuterium concentrations

2. The ratio of deuterium retention determined by TDS and NRA is in the range of 0.8–1.0 when D_2 and HD contributions are considered. Taking into account the estimated contributions of HDO and D_2O molecules increases this ratio to 1.1–1.3.
3. 1.2 times higher considering only D_2 and HD contributions, and 2.4 times higher taking into account HDO and D_2O contributions.

at the highest strains at 573 K and 873 K is much larger than the ratio of the corresponding dislocation densities.

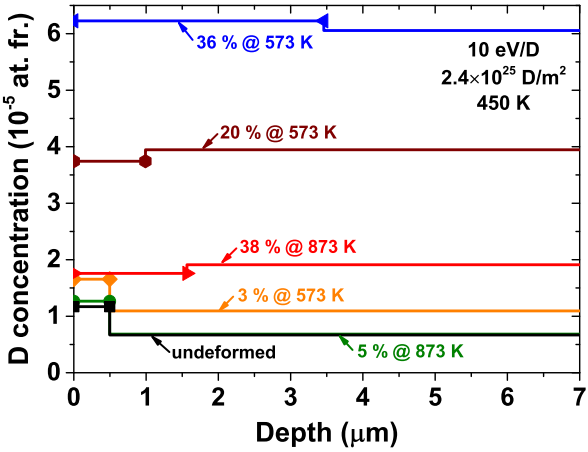

Fig. 8.11: Deuterium concentration profiles in recrystallized tungsten deformed to various strains at two different temperatures (573 K and 873 K) and then exposed to a deuterium plasma with a mean ion energy of 10 eV/D to a fluence of 2.4×10^{25} D/m^2 at a sample temperature of 450 K.

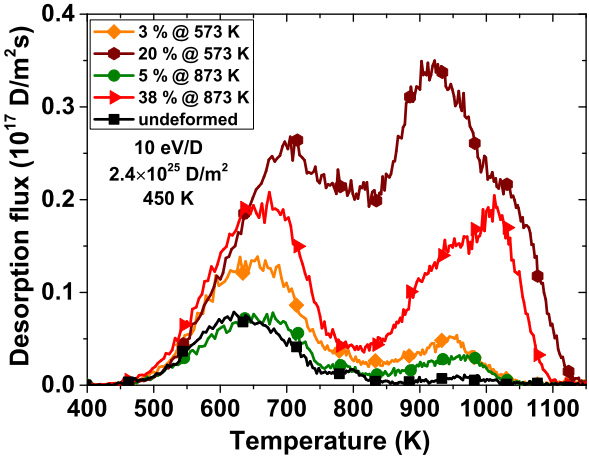

Fig. 8.12: TDS spectra of D_2 molecules from recrystallized tungsten deformed to various strains at two different temperatures (573 K and 873 K) and then exposed to a deuterium plasma with a mean ion energy of 10 eV/D to a fluence of 2.4×10^{25} D/m^2 at a sample temperature of 450 K.

Fig. 8.12 shows the TDS spectra after the exposure at 450 K. Due to technical reasons, the spectrum from the sample deformed to 36 % strain at 573 K could not be measured, therefore, the spectrum of the sample deformed at the same temperature to a lower strain (20 %) is shown. As can be seen, the peak close to 550 K has disappeared, while the peak near 700 K is still present

together with high-temperature peaks. The amplitudes of all peaks increase with strain, but the most pronounced increase is in the high-temperature part of the spectra for both deformation temperatures. The deuterium retention determined from TDS is 1.6–2.9 times larger compared with that determined by NRA[4], indicating deeper deuterium diffusion into the bulk compared with the 370 K exposure. Nevertheless, the total deuterium inventory after the 450 K exposure is several times lower compared with that after the 370 K exposure.

8.4 Discussion

Plasma exposure of all types of samples at 370 K results in the appearance of blisters and protrusions. The noticeable increase in their number density is observed already after the smallest used strain and with further increasing strain their number density increases only slowly. This is reflected in the deuterium depth profiles as enhancement of the concentration in the subsurface region where the cavities of blisters and protrusions are located, which is similar to the situation observed after the high-flux deuterium plasma exposure of tungsten at about 380 K described in chapter 5. However, the number densities of surface modifications observed in the present experiments are significantly lower compared with those after the high-flux exposure, which results in almost one order of magnitude lower deuterium concentration in the subsurface layer (compare Figs. 8.9 and 5.4). The deuterium inventories in the deformed samples determined by TDS and NRA are in a good agreement, indicating that most of the deuterium is trapped within the zone probed by NRA. Hence, in the present experiments at 370 K the deuterium retention is presumably dominated by trapping in the defects associated with blisters and protrusions (see also discussions in chapter 5). Since a substantial part of deuterium is released in the TDS peak with the maximum close to 700 K, it can be suggested that this peak corresponds to deuterium release from these defects. This peak was also dominant in the case of deuterium plasma exposure at 370 K of a tungsten single crystal damaged by 200 keV protons (Fig. D.5 in appendix D). Also this sample showed a considerable formation of protrusions, despite the different initial materials and their treatment. Note that in the present experiments the number density of surface modifications is significantly lower than on the proton-damaged single crystal (although the plasma exposure conditions are identical), which results in almost one order of magnitude lower concentrations of trapped deuterium (compare Figs. D.4 and 8.9). A major release peak at a similar temperature has also been observed after low-flux deuterium plasma exposure of hot-rolled tungsten at 370 K, where significant blistering of the material happened [69]. Consequently, the 700 K peak seems to accompany the formation of blisters and protrusions.

4. Taking into account HDO and D_2O contributions this ratio increases to 3.9–7.2.

Manhard [69] showed that the amount of deuterium trapped in gaseous form inside the cavities of blisters cannot fully explain the enhanced deuterium trapping. Hence, it was suggested that the material surrounding a growing blister cavity is subjected to a plastic deformation inducing the creation of dislocations, which then can trap deuterium. A significantly enhanced density of dislocations in blister caps (up to 7×10^{14} m^{-2}) was indeed observed by TEM [16]. However, the present experiments both at 370 K, which are affected by the presence of blisters, and at 450 K, when no apparent surface modifications are detected, do not show the expected linear correlation between the dislocation density and the concentration of trapped deuterium. Moreover, in the case of 450 K exposure the TDS spectra still have a complicated structure consisting of several peaks, which amplitudes depend on the strain and the deformation temperature and their maxima are located at high temperatures (700 K and higher). This indicates that several types of trapping sites for deuterium are present in the mechanically-deformed materials and some of them have high detrapping energies, comparable with those for vacancies and vacancy clusters (see chapter 6). However, PALS measurements indicate that the defects corresponding to the second lifetime component are dominant in all deformed samples, while the intensity of the longest lifetime component (which probably corresponds to large vacancy clusters) is practically independent of the strain and is within 5 %.

There are several possible reasons for this observation. One possibility is that some of the deuterium-decorable defects are invisible for positrons. However, positrons, like deuterium atoms, are attracted by the open-volume defects with reduced electron density. The only exception are impurities (such as carbon, oxygen), which form chemical bonds with deuterium but do not have an open volume (i.e., invisible for positrons). But their concentration should be the same in all specimens. So this option can be ruled out. Another possibility is that new defects are introduced during the plasma exposure, even if no surface modifications are visible, and their concentration depends on the strain. Such defects may be deuterium-containing bubbles, which can be nucleated on dislocations, as suggested by Terentyev et al. [34]. Experiments at even higher exposure temperatures, when the solute deuterium concentration is low enough to prevent nucleation of such defects, would be necessary to clarify this.

To get an idea about the contributions of various kinds of trapping sites to the deuterium inventory, the TDS spectra of the samples exposed at 450 K were decomposed into two to four asymmetric Gaussian peaks[5] and the area under a decomposed peak is considered as the amount of deuterium released in the respective peak. Fig. 8.13 shows the strain dependence of the deuterium released in the 700 K peak and in the rest of the peaks at higher temperatures taking into account both D_2 and HD contributions. The evolution of the average dislocation density in the grain interior measured by TEM is also shown in the graph. In addition, the positron trapping rate (which is proportional to the

5. Since the TDS peaks are inherently asymmetric [53].

defect concentration) into the defects corresponding to the second lifetime τ_2 (which dominates the positron trapping) computed using the standard positron trapping model (Eq. B.7 in appendix B) is shown. The applicability of the standard trapping model was checked by using Eq. B.8, which yields the bulk lifetimes τ_B in the range of 101–128 ps, which are in fair agreement both with the experimentally determined and the calculated values [126, 143, 144]. For all variables in Fig. 8.13 the shown dependences are normalized by their respective values for the undeformed sample, which allows to reveal their relative increase with strain. At both deformation temperatures the strain dependences of the concentration of positron-trapping defects and of the dislocation density in the grain interior are quite different: Only at the lowest strain they increase in a similar manner, whereas at higher strains the increase rate of positron-trapping defects is much slower than the increase of the dislocation density. Note that the standard trapping model assumes a homogeneous defect distribution, while in the present samples even at low strains the inhomogeneous defect distribution is apparent: formation of dislocation pile-ups near grain boundaries and formation of dislocation walls at high strains (especially in the case of deformation at 873 K). This can result in underestimation of the defect concentration [125].

The amount of deuterium released in the 700 K peak increases with strain in a similar manner as the estimated positron trapping rate at both deformation temperatures. Hence, this peak may correspond to deuterium release from the deformation-induced defects visible for positrons. Since at intermediate and highest strains the concentration of these defects increases much less than the dislocation density, it seems that these defects are not the dislocation lines themselves, but rather another type of deformation-induced defects. As was discussed in section 8.2.2, during the deformation the dislocations can both acquire jogs and trap deformation-induced vacancies, and the value of the second lifetime can correspond to positron annihilation at these defects. DFT calculations by Terentyev et al. [34] predict that the hydrogen binding energy with a vacancy attached to a screw dislocation line is comparable with that to a single vacancy. Therefore, these defects can correspond to the TDS peak around 700 K, which position is characteristic for vacancy-type defects.

This hypothesis can explain why the 700 K peak is dominant in TDS spectra of highly-blistered samples. Since it is observed that with decreasing deformation temperature (at the same strain) the concentration of positron-trapping defects (presumably jogs and/or vacancies) increases, it is possible that their concentration is even higher during the deformation at 370 K induced by the growth of blisters and protrusions. This can explain higher deuterium concentrations in the depth region affected by blisters and protrusions. Note that the molecular deuterium stored in the voids may also contribute to the 700 K peak since there is only a small difference in the deuterium detrapping energies from these defects (see chapter 7).

The strain dependence of the amount of deuterium released in the higher temperature peaks (which positions are characteristic for vacancy clusters)

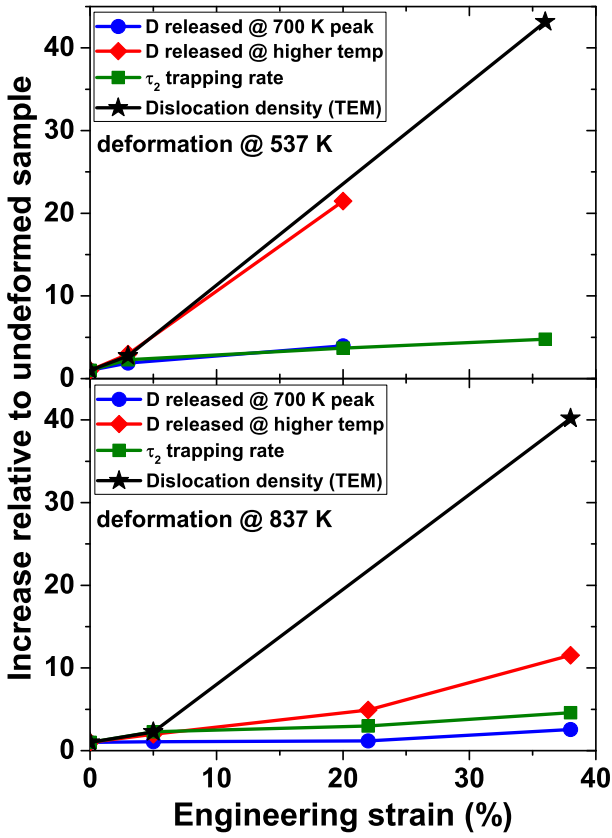

Fig. 8.13: The amount of deuterium released in a 700 K peak and in the peaks at higher temperatures in TDS spectra from recrystallized tungsten deformed to various strains at two different temperatures (573 K and 873 K) after the exposure to a deuterium plasma with a mean ion energy of 10 eV/D to a fluence of 2.4×10^{25} D/m^2 at a sample temperature of 450 K. The strain dependence of the positron trapping rate into the defects corresponding to the second lifetime (τ_2) estimated using the standard trapping model is also shown. The dislocation density in the grain interior measured by TEM as a function of strain is also demonstrated. All the values are normalized by the respective values for the undeformed sample.

increases faster than the amount of deuterium released in the 700 K peak. However, the increase rates at large strains are considerably different at the two deformation temperatures, hence, no definite conclusions about the origin and nature of the defects corresponding to this peak can be made.

Despite the complications in the interpretation of the defect types, it can be concluded that the mechanical deformation introduces not simply dislocation lines, but also jogs and/or vacancies and maybe vacancy clusters, which dominate deuterium retention under the used plasma exposure conditions. Hence, it can be suggested that the dislocations themselves are very shallow traps for deuterium, as predicted by DFT calculations [34], and are not able to hold appreciable amounts of deuterium both at 370 K and 450 K. In addition, the

trapped deuterium concentrations measured in the present experiments are still at least one order of magnitude smaller compared with those in radiation defects at high damage levels (see Fig. 7.9). Consequently, under reactor-relevant temperatures the deuterium trapping by dislocations and other deformation-induced defects should play only a minor role.

Note that the present study examined only deformation-induced dislocations (i.e., edge and screw), while radiation-induced dislocation loops were not examined, which may have a different binding energy with deuterium [74]. However, experimental assessment of their trapping properties is challenging since it seems to be impossible to prepare samples having predominantly dislocation loops without other radiation-induced defects (vacancies and vacancy clusters).

8.5 Chapter summary

The experiments devoted to the investigation of deuterium interactions with dislocations in tungsten have been carried out using a set of samples with more than one order of magnitude difference in the dislocation density. The specimens were prepared by tensile deformation of recrystallized tungsten to various strains (3–38 %) at two different temperatures (573 K and 873 K). Plasma exposure at 370 K revealed that mechanical deformation already to low strains (3–5 %) results in a significant increase in the number density of emerging blisters and protrusions. Based on TEM observations, this was attributed to the formation of dislocation pile-ups near grain boundaries during the deformation, which can facilitate the formation of intergranular cracks during the plasma exposure. The appearance of these surface modifications resulted in the introduction of additional trapping sites for deuterium in the material, albeit the trapped deuterium concentration was still quite low (a few times 10^{-4} at. fr.).

Plasma exposure at 450 K allowed to avoid the formation of these surface modifications, resulting in practically flat deuterium concentration profiles and smaller deuterium concentrations (below 10^{-4} at. fr.) suggesting that the experimental results were less obscured by the plasma-induced defects. Nevertheless, the dependence of the trapped deuterium concentration on the strain was weaker than the respective increase of dislocation density in the grain interior measured by TEM. The TDS spectra exhibited a complicated structure consisting of at least two peaks which amplitudes depended on the strain and their positions were characteristic for deuterium release from vacancies and vacancy clusters. PALS analysis also detected the presence of vacancy-type defects which concentration increased with strain in a similar manner as the amount of deuterium released in the corresponding TDS peak. Therefore, it is suggested that the dislocation lines themselves act only as shallows trap for deuterium, which agrees with the predictions based on DFT calculations. The deuterium retention in mechanically-deformed samples at the used temperat-

ures of 370 K and 450 K is governed by the by-products of the deformation: jogs on the dislocation lines and/or deformation-induced vacancies and probably vacancy clusters.

Chapter 9

Conclusions and outlook

The aim of this thesis is to clarify the contributions of various types of lattice defects to hydrogen isotope retention in tungsten. For this, samples having one dominant defect type were prepared. To introduce predominantly vacancies, well-annealed tungsten specimens were irradiated by light ions (200 keV protons or 10 keV deuterons) to damage levels below 10^{-2} dpa. To introduce dislocations, well-annealed tungsten samples were subjected to a tensile plastic deformation to various strains (3–38 %) at two temperatures (573 K and 873 K). Plasma-induced defects were introduced by exposing polycrystalline tungsten to high fluxes (3–5$\times 10^{23}$ D/m^{2}s) of low-energy (40 eV/D) deuterium ions, similar to those expected in the divertor of ITER, to high fluences up to 1.2×10^{28} D/m^2 at a sample temperature near 380 K. The introduced defects were then thoroughly characterized. Open-volume defects (vacancies and vacancy clusters) were studied using positron annihilation lifetime spectroscopy (PALS). The dislocation microstructure was investigated using transmission electron microscopy (TEM). The structure of plasma-induced blisters was examined using scanning electron microscopy (SEM).

It was found that vacancies act as strong traps for deuterium. The sum of the deuterium binding energy with vacancies and the activation energy for deuterium diffusion in tungsten was determined to be $E_b+E_D = 1.56\pm0.06$ eV from a series of thermal desorption spectroscopy (TDS) measurements performed using identical samples and different heating rates. This allowed to determine $E_b + E_D$ directly from the shift of the desorption maximum with increasing heating rate using the analytical formula proposed by Guterl et al. [53] without any additional knowledge, in contrast to the commonly used method based on the simulation of a single TDS spectrum.

At temperatures above 600 K vacancies become mobile in tungsten and can either annihilate at various sinks, or agglomerate in clusters. Post-irradiation annealing at temperatures of 800 K and above resulted in the formation of clusters containing more than 30 vacancies. This size is larger than that

expected from thermal stability considerations based on calculated values of vacancy binding energies to clusters [87, 149]. It is, therefore, suggested that the coarsening of clusters with increasing annealing temperature is mainly driven by the mobility of small vacancy clusters. At temperatures above 1200 K annealing of vacancy clusters sets in and is presumably accompanied by further coarsening of clusters. The complete removal of vacancy clusters requires temperatures above 1700 K. Higher annealing temperatures are required at higher damage levels. The concentration of deuterium trapped in these defects decreased with increasing post-irradiation annealing temperature and generally followed the annealing stages detected by PALS. TDS results indicate that small vacancy clusters bind deuterium stronger than vacancies [135]. Large vacancy clusters (voids) can also store D_2 gas in their volume. The binding energy of molecular deuterium inside voids was found to be close to that for a deuterium atom in a vacancy, in line with thermodynamic estimations [73].

It was concluded that dislocations in tungsten are not able to trap appreciable amounts of deuterium already at temperatures as low as 370 K. It was also found that mechanical deformation introduces not only dislocations, but also jogs at the dislocation lines and/or vacancies and probably vacancy clusters. However, their concentration was found to be quite low even at very high strains, therefore, their contribution to deuterium inventory is low.

It was observed that blister-like structures introduce additional trapping sites for deuterium in a subsurface region with a thickness coinciding with the depth up to where the cracks corresponding to blister cavities are located. The concentration of these defects was higher than the concentration of intrinsic defects in the material, therefore, the trapping in these defects can govern the deuterium retention in pristine tungsten under certain conditions. The same tendencies were also observed in experiments with mechanically-deformed and proton-damaged samples under exposure conditions causing blistering. Hence, the emergence of blister-like structures often hinders revealing the features of deuterium interaction with the defects and care must be taken when interpreting such results.

Damaging of tungsten either by protons or by mechanical deformation facilitates the formation of blister-like structures. Some introduced defects seem to act as nucleation sites for blisters. In mechanically-deformed samples, this was attributed mainly to the formation of dislocation pile-ups near grain boundaries, while in proton-damaged samples the nucleation process remains unclear.

In ITER, DEMO, and future power plants tungsten plasma-facing components (PFCs) will operate at elevated temperatures determined by the heat flux, PFC thickness, and the coolant temperature (around 340 K for water in ITER; 570 K for water and 770 K for helium in DEMO [2]). Therefore, based on the current results, partial annealing of neutron-induced defects and considerable clustering of vacancies can be expected in tungsten PFCs. However, the temperatures required to completely anneal radiation defects (above 1700 K) are higher than the expected operation temperature of tungsten PFCs during inter-ELM

phases of discharges and are also higher than the recrystallization temperature of tungsten. Hence, in ITER and DEMO complete recovery of neutron-induced defects is unlikely under normal operational conditions. Nevertheless, since deuterium release both from vacancies and from voids takes place around 600 K, significant hydrogen isotope detrapping from these defects should take place in tungsten PFCs, meaning that only some fraction of neutron-induced defects will be filled with hydrogen isotopes. Due to their low hydrogen binding energy, dislocations are expected to yield a negligible contribution to the tritium inventory. Due to the high incident fluxes of hydrogen isotopes, blister-like structures may form in some areas, despite the high surface temperatures [6]. Nevertheless, due to the relatively small depth affected by the blister-like structures (up to a few tens of μm [17, 90, 93]) compared with the thickness of tungsten PFCs the influence of these defects should be also relatively minor compared with the influence of neutron-induced defects which are distributed through the whole PFC thickness.

The results presented here highlight several research topics that can be investigated in the future:

- The method of determination of deuterium binding energies with defects from TDS measurements with different heating rates can be applied for other radiation-induced defects in tungsten such as D_2 gas-filled voids and helium bubbles.

- The next studies utilizing samples having one dominant defect type (vacancies, vacancy clusters, and voids) can be focussed on hydrogen isotope exchange in these defects. It was recently shown that such kind of experiments allow to determine the fill-level-dependent hydrogen binding energies with the defects [47, 48]. This will allow to estimate the hydrogen binding energy with a second, third, etc. trapped atom in a vacancy in tungsten and compare these energies with density functional theory predictions. In addition, no theoretical predictions for the fill-level-dependent trapping exist for three-dimensional defects such as vacancy clusters, voids, and helium bubbles. Therefore, such experimental studies can stimulate further theoretical work.

- The PALS technique used in the present work can determine the sizes only of small defects, i.e., clusters containing less than 30 vacancies. Therefore, it is desirable to perform TEM investigations of the samples after annealing at different temperatures to get information about annealing of dislocation loops and formation of voids at high temperatures. This will allow to gain a complete interpretation of the defect recovery stages in tungsten.

Appendix A

Dpa calculations

The procedures used for computing the radiation damage levels created by ions and electrons used in chapters 6 and 7 and in appendix E are described here.

All depth profiles of displacement damage under ion irradiation were calculated using the SRIM code version 2013.00 [134], which is commonly used in the ion irradiation community. SRIM uses the Monte Carlo approach to simulate the interaction of energetic particles with solids in the binary collision approximation, i.e., as a sequence of independent classical elastic collisions. Thus, the simulations are valid only for projectile energies above several tens of eV. The programme assumes an amorphous target structure at 0 K. As an additional simplification, only large-angle collisions are treated, between which the particle moves in a straight free flight path[1], i.e., between two collisions it skips over many monolayers of the target. Hence, displacement cascades are only initiated at the end of each flight path, which can result in the appearance of anomalous peaks in the calculated damage distribution at a distance of one free flight path from the surface (see, e.g., Fig. 6.2). The projectile also continuously loses energy on its path due to inelastic (electronic) energy losses.

As input, the type, energy, and the incidence angle of the projectile, as well as the composition, thickness, the lattice binding energy, and the effective threshold displacement energy of the target atoms are specified. The modelled target consists of one-dimensional layers with infinite lateral size. The target composition is fixed during the whole simulation, i.e., there is no sputtering, accumulation of incident projectiles and damage in the target. As recommended by Stoller et al. [167] and Nordlund et al. [80], the calculations are performed using the "Ion Distribution and Quick Calculation of Damage" option which means that only incident particles are followed three-dimensionally until their energy drops below the lowest displacement energy of any target atom or they

1. The mean free flight path is defined as the maximum distance the particle can travel until a collision with an energy transfer above a certain minimum value will occur. At low projectile energies it is fixed to the mean interatomic distance.

leave the target. The energy E_{PKA} transferred in a collision to a target atom (PKA) is then converted into the number of displacements by using the NRT Eq. 3.5 (see section 3.4). The effective displacement threshold energy of 90 eV, as recommended by ASTM [78], is used. Although, as mentioned in section 3.4, this value is considerably higher compared with that derived from experimental data, it is nevertheless used in the present work in order to be comparable with results reported by other researchers. The lattice binding energy is set to 0 eV.

The depth distribution of the number of displacements per incident ion per unit depth $N_{displ}(x)$ [displacements/(ion $\cdot$ m)] is then obtained by summing the displacements created by ions and recoils listed in the "vacancy.txt" output file. The damage distribution as a function of depth is then calculated as:

$$\mathrm{dpa}(x) = \frac{N_{displ}(x)\Phi}{\rho}, \tag{A.1}$$

where Φ is the incident fluence and $\rho = 6.306 \times 10^{28}$ atoms/m^3 is the atomic density of tungsten.

Since SRIM assumes an amorphous target, the results of the calculations should be also valid for polycrystalline materials, since they have many randomly oriented grains and the typical ion beam analysis measurement (e.g., NRA) averages the result over many grains. However, in single crystals, specific effects like ion channelling and focused collision sequences along specific directions take place [33], which can change defect distribution as compared to a polycrystalline material.

For computing the damage caused by irradiation with MeV electrons, in accordance with ASTM recommendations [78], the relativistic scattering cross-section data from Oen [168] calculated using Mott's theory was used. However, this allows computing the damage near the surface only if the energy losses by the beam can be neglected. The depth distribution of the damage can be calculated with the help of Monte Carlo codes, such as ElectronDamage [169], which was used in the present study. Its general principle is quite similar to that of SRIM. The code also uses the concept of a free flight path between collisions, which is chosen according to the total scattering cross-section. It is further assumed that the stopping power is constant along this path. In order to avoid infinitely large cross-sections, the minimum (cutoff) energy transfer in a collision has to be specified. The code uses the McKinley-Feshbach cross-section formula, which is accurate for light elements ($Z \leq 29$) only, while for high-Z elements, such as tungsten, it underestimates the cross-section: The ratio of Mott to McKinley-Feshbach cross-sections for tungsten increases with increasing electron scattering angle (0–180°) in the range of 0.95–2.6 and is only weakly dependent on the incident energy (in the relevant range of 1–10 MeV) [168]. The damage computed using Oen's tables is about 1.8 times higher compared with that calculated by the code for 4.5 MeV electrons near the surface. Nevertheless, the simulation results still can be used to estimate the shape of the damage distribution.

Appendix B

Standard positron trapping model

The standard trapping model for positrons used in chapter 8 for estimating the concentration of defects is presented here.

The fate of a positron in a metal is determined by the competition between trapping in various kinds of defects (with subsequent annihilation there) and annihilation in the bulk. This situation can be described by a set of rate equations, which are referred to as the standard positron trapping model [125]. This model is based on the following assumptions:

- The material contains N types of positron-trapping defects having a homogeneous depth distribution;
- The detrapping of positrons from the defects is negligible;
- At time $t = 0$ all the positrons are thermalized and are located in a delocalized bulk state;
- The positron trapping rate κ_d^i into a defect type i is proportional to the defect concentration N_d^i: $\kappa_d^i = \mu_d^i N_d^i$, where μ_d^i is the specific positron trapping rate into the defect.

Then the governing equations describing the time evolution of the probabilities of the existence of a positron in a free delocalized state in the bulk $n_b(t)$ and in the i type defect $n_d^i(t)$ are given by:

$$\frac{dn_b}{dt} = -\sum_{i=1}^{N} \kappa_d^i n_b - \frac{n_b}{\tau_b}, \tag{B.1}$$

$$\frac{dn_d^i}{dt} = \kappa_d^i n_b - \frac{n_d^i}{\tau_d^i}, \tag{B.2}$$

where τ_d^i and τ_b are the positron lifetimes in the type i defect and in the bulk, respectively. By using the initial conditions $n_b(0) = 1$ and $n_d^i(0) = 0$ this system can be solved analytically giving the probability that a positron is still alive at time t:

$$n(t) = n_b(t) + \sum_{i=1}^{N} n_d^i(t) = \sum_{j=1}^{N+1} I_j \exp\left(-\frac{t}{\tau_j}\right), \tag{B.3}$$

where I_1 and I_j refer to the relative intensity of the positrons in the bulk and in the type $j-1$ defect, respectively, and are expressed as:

$$I_1 = 1 - \sum_{j=2}^{N+1} I_j, \qquad \tau_1 = \frac{1}{\frac{1}{\tau_B} + \sum_{i=1}^{N} \kappa_d^i}; \tag{B.4}$$

$$I_j = \frac{\kappa_d^{j-1}}{\frac{1}{\tau_B} - \frac{1}{\tau_j} + \sum_{i=1}^{N} \kappa_d^i}, \qquad \tau_j = \tau_d^{j-1}. \tag{B.5}$$

The τ_1 is referred to as the reduced bulk lifetime, which comprises both the annihilation from the delocalized bulk state and disappearance from it via trapping into defects.

The positron lifetime spectrum $Z_{theor}(t)$, which is the probability that a positron will annihilate at time t, is then given by the negative derivative of Eq. B.3:

$$Z_{theor}(t) = -\frac{dn}{dt} = \sum_{i=1}^{N+1} \frac{I_i}{\tau_i} \exp\left(-\frac{t}{\tau_i}\right). \tag{B.6}$$

A measured lifetime spectrum is described by Eq. B.6 convoluted with an instrumental time resolution function plus the background (see Eq. 4.4).

The trapping rates κ_d^i can be calculated from Eqs. B.4–B.5:

$$\kappa_d^i = I_{i+1}\left(\frac{1}{\tau_1} - \frac{1}{\tau_{i+1}}\right). \tag{B.7}$$

The applicability of the standard trapping model can be checked using the equation:

$$\frac{1}{\tau_B} = \sum_{i=1}^{N+1} \frac{I_i}{\tau_i} \tag{B.8}$$

with the lifetimes and relative intensities obtained from the deconvolution of an experimental lifetime spectrum and comparing the computed value of τ_B with the theoretical one.

Appendix C

Impurity content of the used tungsten materials

The maximum impurity concentrations specified by the suppliers in polycrystalline tungsten (used in chapters 5, 6, and 8) and in single crystalline tungsten (used in chapter 7) are presented here.

Table C.1: Maximum impurity concentrations (as specified by the supplier) in the hot-rolled polycrystalline tungsten supplied by Plansee (Austria).

Impurity	10^{-4} wt. %	10^{-4} at. %
Al	15	102
Fe	30	99
Si	20	131
H	5	919
Cd	5	33
Cr	20	71
K	10	47
Mo	100	192
N	5	66
Hg	1	1
Cu	10	29
Ni	20	63
C	30	459
O	20	230
Pb	5	4

Table C.2: Maximum impurity concentrations (as specified by the supplier) in the tungsten (100) single crystals supplied by the Institute of Solid State Physics (Chernogolovka, Russia) [137].

Impurity	10^{-4} wt. %	10^{-4} at. %
O	0.5	5.8
C	1	15.3
N	0.6	7.9
Si	0.3	2.0
Al	0.1	0.7
K	0.1	0.5
Ca	0.1	0.5
Na	0.3	2.4
P	0.3	1.8
S	0.3	1.7
Mn	0.3	1.0
Nb	0.1	0.2
Ta	0.1	0.1
Re	0.1	0.1
V	0.3	1.1
Fe	0.1	0.3
Ni	0.06	0.2
Co	0.3	0.9
Cr	0.05	0.2
Cu	0.05	0.1
Pb	0.1	0.1

Appendix D

TDS data of samples damaged by protons

The results of TDS measurements of the samples damaged by 200 keV protons, post-irradiation annealed at various temperatures and then exposed to a deuterium plasma at 450 K (see chapter 7 for details) are presented here. In addition, SEM, NRA, and TDS results of an as-damaged sample exposed to a deuterium plasma at 370 K are also shown.

D.1 Plasma exposure at 450 K

Fig. D.1 shows the TDS spectra of different molecules (H_2, D_2, HD, HDO, and D_2O) from the sample damaged by 200 keV protons and then annealed at 500 K. As can be seen, heteronuclear molecules dominate over the D_2 contribution, which has not been observed in the case of *in situ* TDS measurements presented in chapter 6 (Fig. 6.5), where the deuterium inventories were similar to those in the present experiments. This confirms the detrimental effect (in the case of low amounts of trapped deuterium) of air exposure of the samples in between deuterium loading and TDS analyses [120]. The important consequence is that the peak near 950 K is much more pronounced in the HD spectrum for all samples. This peak is also present in the spectrum of H_2 molecules, while no peaks are visible in the H_2 spectrum during the background run without a sample. Hence, these H_2 molecules originate from the samples. However, their amount is varying among different samples (including the undamaged) up to a factor 4.6, despite the fact that all samples have been degassed prior to damaging under identical conditions. In addition, no correlation with the post-damaging annealing temperature is visible. Therefore, the reason for this variation remains unclear. The domination of the peak near 950 K in HD molecules is visible also on the undamaged sample, as well as on the sample

damaged by 9 MeV tungsten ions to 10^{-3} dpa (not shown here), so this cannot be explained by the protium implanted into the samples during damaging, but is rather explainable by low amounts of trapped deuterium, as was discussed in chapter 6 and in [119, 120].

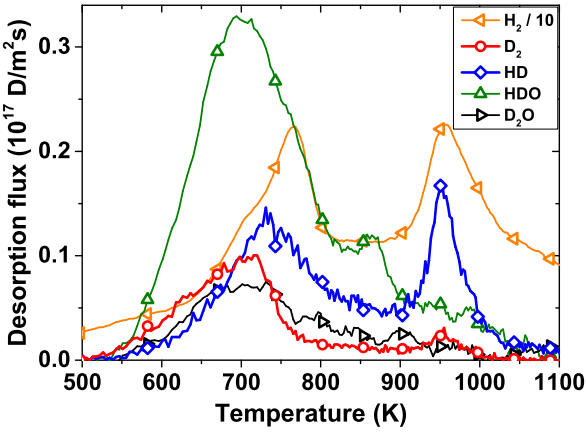

Fig. D.1: TDS spectra of H_2, D_2, HD, HDO, and D_2O molecules from a tungsten (100) single crystal damaged by 200 keV protons to a fluence of 1×10^{20} p/m^2, post-irradiation annealed at 500 K for 15 min and then exposed to a deuterium plasma with a mean ion energy of 10 eV/D to a fluence of 1×10^{25} D/m^2 at a sample temperature of 450 K. Note that the spectrum of H_2 molecules is downscaled by a factor of ten.

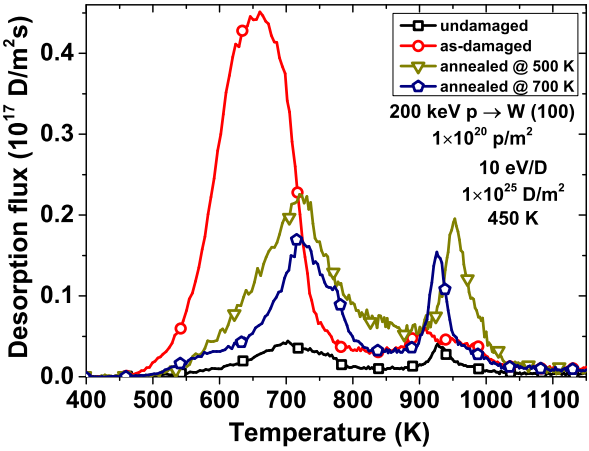

Fig. D.2: The sum of TDS spectra of D_2 and HD molecules from tungsten (100) single crystals damaged by 200 keV protons to a fluence of 1×10^{20} p/m^2, post-irradiation annealed at various temperatures for 15 min and then exposed to a deuterium plasma with a mean ion energy of 10 eV/D to a fluence of 1×10^{25} D/m^2 at a sample temperature of 450 K.

Fig. D.2 shows a comparison of TDS spectra from the following samples: undamaged, as-damaged, and post-damaging annealed at 500 K and 700 K.

Since the HD contribution is considerable for all samples, the sums of D_2 and HD spectra are shown[1]. The spectrum of the as-damaged sample exhibits one dominant release peak near 650 K with an additional rather small but broad peak near 910 K and high-temperature tails extending up to 1250 K. The undamaged sample has a much smaller deuterium release, characterized by peaks near 700 K and 930 K. Already after annealing at 500 K the first peak shifts to 700 K and its amplitude decreases by a factor of two, while the peak near 950 K becomes prominent. With increasing annealing temperature the amplitudes of both peaks change in an unsystematic way and there is no correlation between the changes in the TDS spectra and the respective changes in the defect structure detected by PALS. For instance, PALS indicates considerable differences in defect structure between annealings at 500 K and 700 K, while the TDS spectra are very similar. A few measurements have been repeated and the reproducibility of the results was unsatisfactory. The reason for this is not clear. Consequently, for such samples *in situ* TDS measurements would be necessary in order to reduce the uncertainties related to the contributions of heteronuclear molecules. It can be also noted that the peak near 950 K is very narrow, e.g., it is narrower than the peak attributed to the deuterium release from vacancy clusters in the measurements presented in chapter 6 and its position is 250 K higher (compare with Fig. 6.3). The latter can be partially explained by the ten times wider damaged zone, which considerably increases the retrapping probability. A narrow high-temperature peak has been previously observed after the exposure of self-damaged tungsten to a deuterium atomic beam at 800 K [170], while it has never been observed after post-irradiation annealing of tungsten damaged both by light ions [73, 87] and by self-ions [171]. The reason for this behaviour is still unclear.

D.2 Plasma exposure at 370 K

To check for the presence of trapping sites with low binding energies which are not able to hold deuterium at 450 K and can correspond, for example, to filling of vacancies with multiple deuterium atoms, one as-damaged and one undamaged sample were exposed to a deuterium plasma at 370 K. In order to compensate for the slower deuterium diffusion at 370 K, a larger incident fluence (compared with the experiments at 450 K) of 2.4×10^{25} D/m^2 was used.

These exposure conditions resulted in a considerable increase (compared with that under 450 K exposure) of the number density and average size of protrusions emerged on the as-damaged sample: compare Figs. D.3 and 7.5. No surface modifications were detected on the undamaged sample.

1. Note that the shapes and the positions of the peaks are different in D_2 and HD spectra, which is reflected by broadening of the resulting peaks and change of their positions in the sum of D_2 and HD spectra.

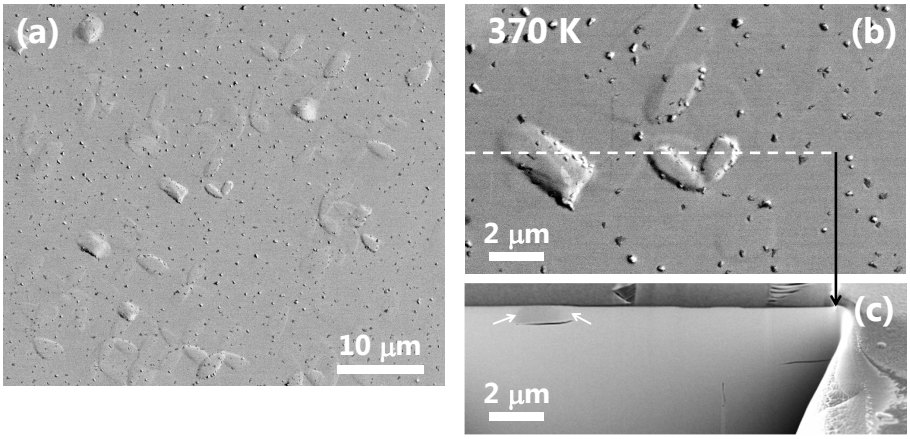

Fig. D.3: A tungsten (100) single crystal damaged by 200 keV protons to a fluence of 1×10^{20} p/m^2 and then exposed to a deuterium plasma with a mean ion energy of 10 eV/D to a fluence of 2.4×10^{25} D/m^2 at a sample temperature of 370 K: (a) and (b) SEM images of the surface with different magnifications; (c) a SEM image of a cross-section at the position indicated by the dashed line in (b). The surface in (c) was protected by a Pt-C layer before cutting. The black arrow indicates the same place in (b) and (c). The white arrows in (c) indicate the visible lattice distortion above the crack. The images were taken after TDS. The small particles with dimensions of a few hundred nm are silicon dioxide contaminations (as detected by X-ray photoelectron spectroscopy (XPS) and EDX) presumably introduced during TDS measurements (since the samples were heated in a quartz tube).

Cross-sections of several regions containing protrusions were examined with SEM. Figs. D.3(b) and (c) show a SEM image of several protrusions and the cross-sectional SEM image of three visible structures, respectively. Cracks are present underneath the protrusions, but sometimes also without apparent surface structures (see the crack on the right in Fig. D.3(c)). Most of the observed cracks are either approximately parallel or perpendicular to the surface. The analysis of the sample with electron backscatter diffraction (EBSD) technique reveals that these cracks are lying in the {100} planes (recall that the crystal surface is formed by a (100) plane), which is the preferred cleavage plane of tungsten single crystals at low deformation temperatures [172]. The cracks extend to depths up to 6.6 μm, which are considerably larger than those observed after the exposure at 450 K. The change of the contrast above some cracks running parallel to the surface (marked with white arrows in Fig. D.3(c)) is also visible in SEM images indicating the presence of lattice distortion.

Fig. D.4 shows the deuterium concentration profile in the as-damaged sample after the plasma exposure at 370 K. The deuterium concentration in the undamaged sample is again low (not shown), although definitely higher compared with that after the 450 K exposure, but still the counting statistics of the NRA spectra is too poor to extract a depth profile. The maximum deuterium concentration in the as-damaged sample is about four times higher compared

with that after the exposure at 450 K (compare with Fig. 7.6). In addition, the concentration profile is much broader and no decrease of deuterium concentration to the bulk value (as in the undamaged sample, i.e., below 10^{-5} at. fr.) at large depths is visible. This can be explained by the fact that the observed cracks extend practically up to the maximum depth probed by NRA (see also section 7.3).

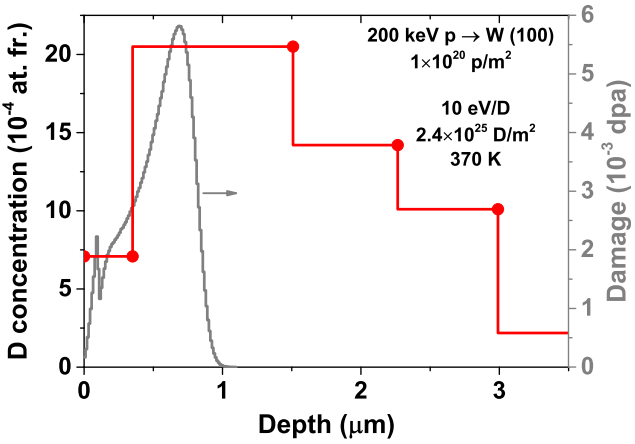

Fig. D.4: Deuterium concentration profile in a tungsten (100) single crystal damaged by 200 keV protons to a fluence of 1×10^{20} p/m^2 and then exposed to a deuterium plasma with a mean ion energy of 10 eV/D to a fluence of 2.4×10^{25} D/m^2 at a sample temperature of 370 K. The damage profile created by 200 keV protons (grey line) calculated using SRIM is also shown. Note that the peak at a depth of 93 nm in the damage profile is an artefact due to the free flight path concept of SRIM as described in appendix A.

Fig. D.5 shows the measured TDS spectra from the as-damaged and undamaged samples. It is clearly visible that the deuterium retention in the as-damaged sample is significantly larger compared with that in the undamaged sample. The spectrum from the as-damaged sample has a major release peak near 700 K, a shoulder near 500 K, and a high-temperature tail extending up to 1000 K. It seems that this spectrum is dominated by trapping in the defects introduced with protrusions, as discussed in detail in chapter 8.

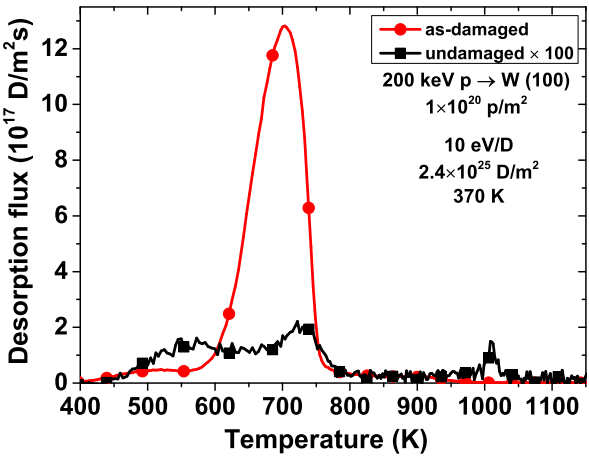

Fig. D.5: TDS spectrum of D_2 molecules from a tungsten (100) single crystal damaged by 200 keV protons to a fluence of 1×10^{20} p/m^2 and then exposed to a deuterium plasma with a mean ion energy of 10 eV/D to a fluence of 2.4×10^{25} D/m^2 at a sample temperature of 370 K. Note that the spectrum of the undamaged sample is enlarged by a factor of 100.

Appendix E

Damaging by electrons

The irradiation procedure, PALS, NRA, and TDS results of tungsten single crystals damaged by 4.5 MeV electrons are described here.

Damaging of samples by 4.5 MeV electrons was performed by using a linear electron accelerator (ENEA, Frascati, Italy) [173]. The accelerator works in pulsed mode with a peak electron current measured by a Rogowski coil of about 140 mA, a pulse duration close to 3 μs, and a repetition rate of 20 Hz. This corresponds to an average beam current of 8 μA. The beam at the target position has an approximately Gaussian radial distribution with a FWHM of 15 mm as determined by measuring the beam spot on exposed radiochromic films. The average incident electron flux on the sample is about 1.7×10^{17} e/m^{2}s. The target is installed perpendicularly to the electron beam at the beam centre. It is clamped to a water-cooled copper holder with a flexible graphite interlayer by using a copper mask with an opening area of 8×8 mm^2 (Fig. E.1). The sample temperature during irradiation does not exceed 300 K as measured by a K-type thermocouple clamped between the sample and the flexible graphite interlayer. The irradiations are performed in air, which results in the formation of ozone (induced both by the electron beam and by bremsstrahlung) in front of the sample. The ozone reacts with the tungsten surface leading to the formation of an oxide layer visible by naked eye. In order to remove this layer, the irradiated samples are first ultrasonically cleaned in a NaOH aqueous solution and then electrochemically polished to remove 5–10 μm from each side.

The samples were damaged to fluences in the range of 0.6–1.9$\times 10^{22}$ e/m^2. Linear interpolation of the data from Oen's tables [168] for the electron energy of 4.5 MeV and a displacement threshold energy of 90 eV yields the displacement cross-section close to 50 barns corresponding to damage levels close to the surface in the range of 3–9$\times 10^{-5}$ dpa. In contrast to ion irradiation, the damage produced by electrons is distributed practically throughout the whole sample thickness, as illustrated in Fig. E.2, and within the analysis ranges of PALS and NRA (≤ 7 μm) the damage profile can be considered as flat.

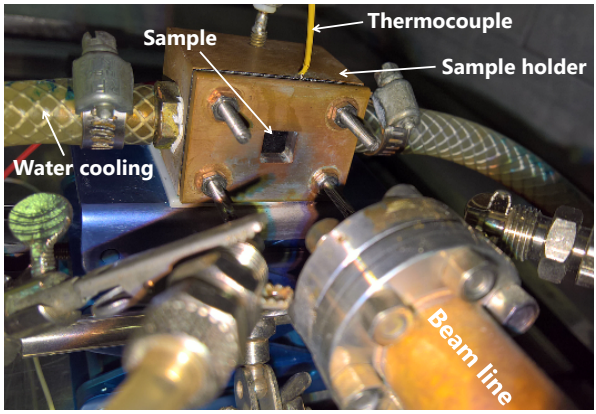

Fig. E.1: The sample holder used for damaging at the electron accelerator.

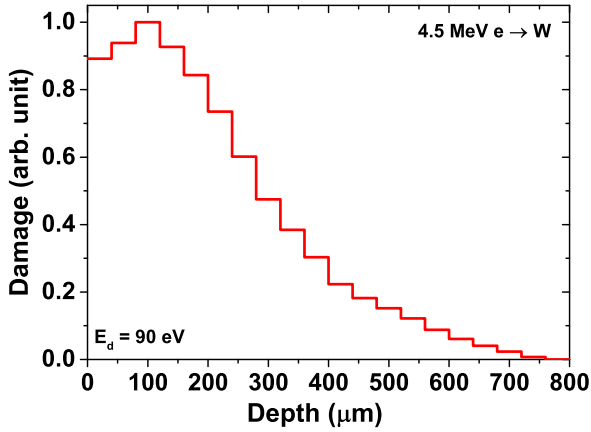

Fig. E.2: The damage profile in tungsten irradiated by 4.5 MeV electrons calculated using the ElectronDamage code [169]. The details of the calculations are described in appendix A.

In order to be able to compare the results of the experiments with damaging by protons and electrons and to minimise the risk of the formation of surface modifications, the samples damaged by electrons were exposed at 450 K. However, since the damage levels achieved via electron damaging (maximum 9×10^{-5} dpa) are significantly lower compared with that in the experiments with protons (5.8×10^{-3} dpa), in order to allow deuterium to diffuse deep into the sample to have an appreciable deuterium inventory measurable by TDS, a larger fluence (compared with that for the samples damaged by protons) of 3.2×10^{25} D/m^2 was applied. Examination of the samples with SEM after the plasma exposure did not give indications of the presence of any apparent surface modifications.

Fig. E.3 shows the measured deuterium concentration profiles in the samples: They are almost flat and the increase of the deuterium concentration with

increasing damage level is apparent. Note the lower deuterium concentrations in these samples compared with those in the samples damaged by protons (Fig. 7.6). However, there is no proportionality between the calculated dpa and the measured deuterium concentration in the samples damaged by protons and electrons. The deuterium concentration in the undamaged sample is very low (a few times 10^{-6} at. fr.) and could not be accurately measured.

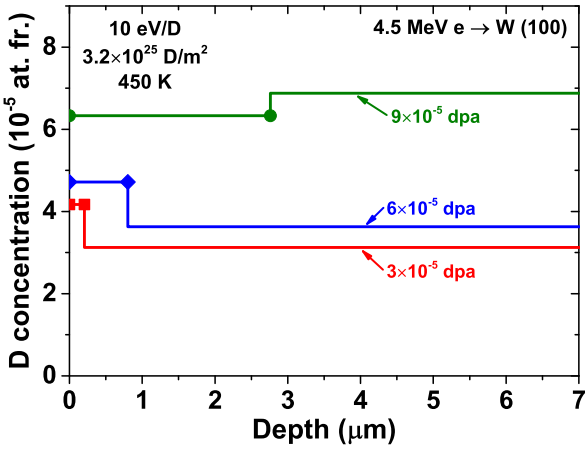

Fig. E.3: Deuterium concentration profiles in tungsten (100) single crystals damaged by 4.5 MeV electrons to various damage levels and then exposed to a deuterium plasma with a mean ion energy of 10 eV/D to a fluence of 3.2×10^{25} D/m^2 at a sample temperature of 450 K.

Fig. E.4 shows the TDS spectra of the corresponding samples. Compared with the samples damaged by protons, in the TDS spectra of the present specimens the D_2 contribution dominates over HD and D_2O, while the HDO contribution is still higher. It is clearly visible that the deuterium release from the damaged samples is significantly larger compared with that from the undamaged sample. The spectra of the samples damaged by MeV electrons are significantly different from the spectra of the samples damaged by 200 keV protons (Fig. D.2) and by 10 keV deuterium ions (Fig. 6.3), albeit in all cases vacancies are expected to be the dominant trapping sites for deuterium. The spectrum of the sample damaged to the lowest damage level (3×10^{-5} dpa) exhibits a major release peak near 900 K. With increasing damage level the spectra get broader: in the case of the sample damaged to 6×10^{-5} dpa the presence of a shoulder near 800 K becomes apparent and at the highest damage level of 9×10^{-5} dpa the spectrum has a very peculiar shape with no distinct peaks. The ratio of deuterium inventories determined by TDS (D_2 and HD) and NRA is in the range of 1.5–1.8, which increases to 2.6–4.0 when HDO and D_2O contributions are taken into account. This means that the deuterium is trapped within a few tens of μm beneath the surface, despite the low concentration of trapping sites and large incident deuterium fluence.

The observed peak positions rather correspond to deuterium release from vacancy clusters and cannot be explained by the deep location of trapped deuterium. As was mentioned in chapter 7, PALS measurements indicate that the samples have a dominant lifetime typical for a single vacancy. Hence, the formation of vacancy clusters during damaging is quite improbable since the sample temperature during irradiation stayed well below the onset temperature of vacancy mobility. There are two possibilities that can explain this observation. The first possibility is that vacancy clusters are formed during the TDS and that deuterium released from vacancies is then retrapped by vacancy clusters. Indeed, as was previously shown, between 600 K and 700 K vacancy clustering starts to occur and the deuterium release from vacancies also happens near 600 K. According to the criterion given in section 2.4, for the measured concentration of deuterium (which reflects the concentration of defects) and the estimated depth where deuterium is located, the deuterium retrapping during TDS should be significant. Quantitatively this can only be checked by diffusion-trapping simulations which take into account the evolution of defects with temperature, which is not easy to implement and introduces additional free parameters in the model. There is another possibility that a diffusion barrier is present near the surface, which prevents the deuterium release from the sample at low temperatures (and also reduced the rate of deuterium uptake during the plasma exposure). It might be possible that the applied electrochemical polishing procedure was not long enough to remove completely the oxygen-rich near-surface layer, albeit after polishing the surface had a mirror-like finish. Hence, more dedicated experiments are required to resolve this issue.

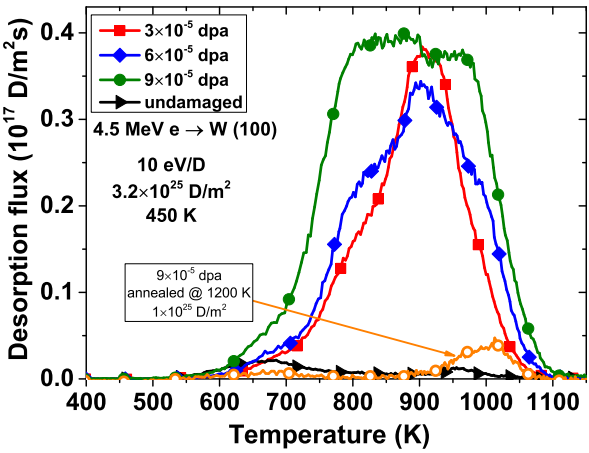

Fig. E.4: TDS spectra of D_2 molecules from tungsten (100) single crystals damaged by 4.5 MeV electrons to various levels and then exposed to a deuterium plasma with a mean ion energy of 10 eV/D to a fluence of 3.2×10^{25} D/m^2 at a sample temperature of 450 K. The spectrum of the sample damaged to 9×10^{-5} dpa which was annealed at 1200 K for 15 min and then exposed to a deuterium plasma with a mean ion energy of 10 eV/D to a fluence of 1×10^{25} D/m^2 at a sample temperature of 450 K is also shown.

For the samples damaged to levels of 6×10^{-5} dpa and 9×10^{-5} dpa the TDS heating was performed until 1200 K, which is sufficient to remove all trapped deuterium, while still a significant fraction of vacancy clusters is visible in experiments with the samples damaged by protons (see Fig. 7.4). The samples were kept at this temperature for 15 min, similarly to the samples damaged by protons. Afterwards, they were electrochemically polished to remove approximately 10 μm from each side in order to get rid of the consequences of NRA measurements, i.e., the damaged zone introduced by the ^{3}He ions and implanted ^{3}He. Then the samples were analysed with PALS. Both samples are dominated by annihilation from the delocalized bulk state indicating a significant defect recovery. The intensity of the second lifetime component near 200 ps is the same for both types of samples (22 %) indicating the presence of vacancies. The intensity of the longest lifetime near 500 ps increases with increasing damage level from 12 % to 20 %, which is an evidence that larger amounts of vacancy clusters are formed in the sample damaged to a higher level. The average positron lifetime also increases with increasing damage level from 146 ps to 189 ps.

After the PALS analyses, the samples were again exposed to a deuterium plasma at 450 K to a fluence of 1×10^{25} D/m^2, i.e., under the same conditions as the samples damaged by protons. The TDS spectrum of the sample damaged to a level of 9×10^{-5} dpa is shown in Fig. E.4. As can be seen, the sample has a major release peak near 1000 K and its amplitude is about an order of magnitude smaller than the amplitude of the peaks on the spectra of the as-damaged sample; a small peak near 650 K is also present and its amplitude is almost the same as in the undamaged sample. The spectrum of the sample damaged to 6×10^{-5} dpa exhibits the same features, but the amplitudes of the peaks are smaller. Hence, annealing at 1200 K leads to a substantial reduction of the concentration of defects, as confirmed by the PALS measurements. Since PALS detects the presence of vacancy clusters which concentration increases with increasing damage level, this suggests that the 1000 K peak may correspond to deuterium release from vacancy clusters. It can be also noted that the peak is not as narrow as that observed in the experiments with the samples damaged by protons (see Fig. D.2).

Appendix F

Stitched TEM images of deformed tungsten

Stitched TEM images of recrystallized tungsten deformed to various strains at two temperatures (573 K and 873 K) studied in chapter 8 are presented here.

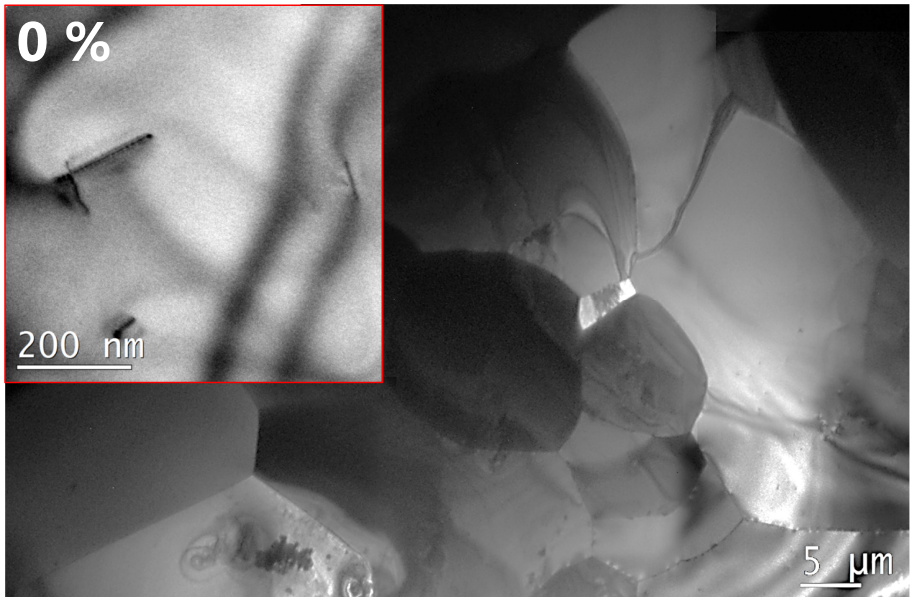

Fig. F.1: Stitched TEM bright field image of an undeformed recrystallized tungsten. The inset illustrates the appearance of dislocation lines. The broad blurred dark lines in the images are artefacts of the TEM specimen preparation and correspond to bend contours and thickness fringes, which appear due to bending of the specimens and non-uniformity of their thicknesses, respectively. This figure is adopted from Ref. [160].

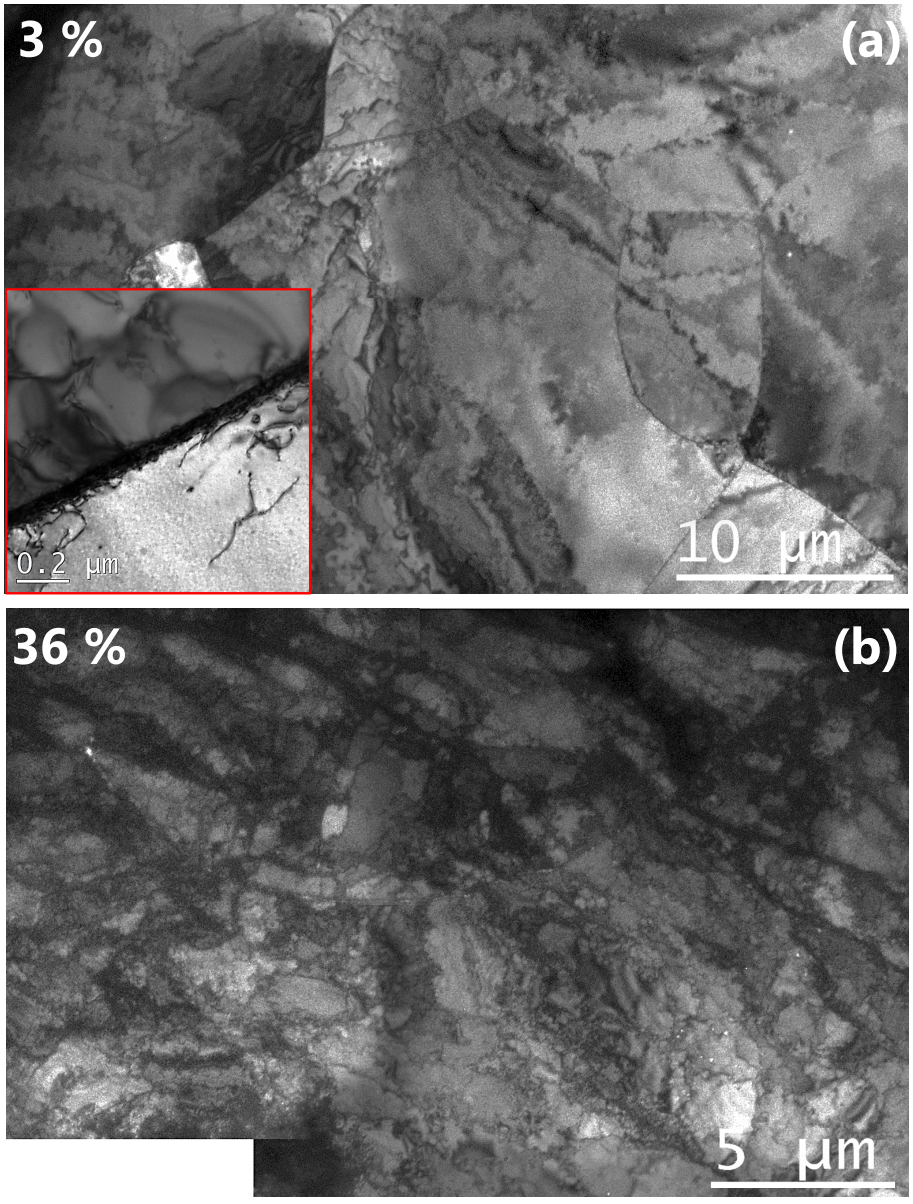

Fig. F.2: Stitched TEM bright field images of recrystallized tungsten: (a) deformed to 3 % strain at 573 K; (b) deformed to 36 % strain at 573 K. The inset in figure (a) shows dislocation pile-ups near a grain boundary. The broad blurred dark lines in the images are artefacts of the TEM specimen preparation and correspond to bend contours and thickness fringes, which appear due to bending of the specimens and non-uniformity of their thicknesses, respectively. The visible bright dots are due to the perforation of the TEM specimens. Note the different scales in (a) and (b).

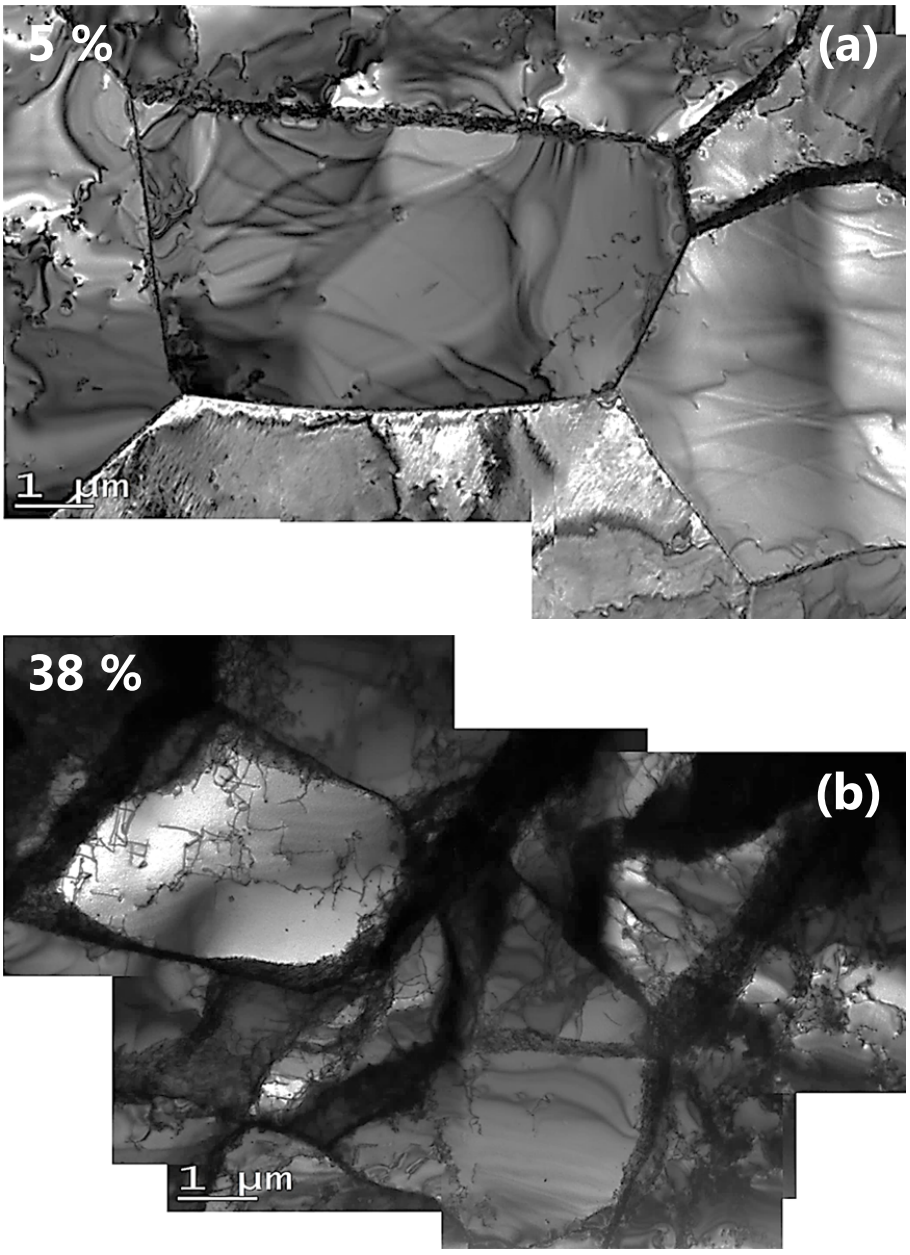

Fig. F.3: Stitched TEM bright field images of recrystallized tungsten: (a) deformed to 5 % strain at 873 K; (b) deformed to 38 % strain at 873 K. The broad blurred dark lines in the images are artefacts of the TEM specimen preparation and correspond to bend contours and thickness fringes, which appear due to bending of the specimens and non-uniformity of their thicknesses, respectively. This figure is adopted from Ref. [160].

Bibliography

[1] M. Keilhacker et al., *High fusion performance from deuterium-tritium plasmas in JET*, Nuclear Fusion **39**, 209 (1999).

[2] G. Federici et al., *European DEMO design strategy and consequences for materials*, Nuclear Fusion **57**, 092002 (2017).

[3] G. Federici et al., *Plasma-material interactions in current tokamaks and their implications for next step fusion reactors*, Nuclear Fusion **41**, 1967 (2001).

[4] J. Roth et al., *Recent analysis of key plasma wall interactions issues for ITER*, Journal of Nuclear Materials **390-391**, 1 (2009).

[5] Y. Ueda et al., *Baseline high heat flux and plasma facing materials for fusion*, Nuclear Fusion **57**, 092006 (2017).

[6] G. De Temmerman, T. Hirai and R. Pitts, *The influence of plasma-surface interaction on the performance of tungsten at the ITER divertor vertical targets*, Plasma Physics and Controlled Fusion **60**, 044018 (2018).

[7] G. Pintsuk, *Tungsten as a Plasma-Facing Material*, in *Comprehensive Nuclear Materials*, edited by R. J. Konings (Elsevier, Oxford, 2012) pp. 551–581.

[8] T. Hirai et al., *Use of tungsten material for the ITER divertor*, Nuclear Materials and Energy **9**, 616 (2016).

[9] V. Philipps, *Tungsten as material for plasma-facing components in fusion devices*, Journal of Nuclear Materials **415**, S2 (2011).

[10] R. Neu et al., *Overview on plasma operation with a full tungsten wall in ASDEX Upgrade*, Journal of Nuclear Materials **438**, S34 (2013).

[11] S. Brezinsek, *Plasma-surface interaction in the Be/W environment: Conclusions drawn from the JET-ILW for ITER*, Journal of Nuclear Materials **463**, 11 (2015).

[12] R. Villari et al., *Nuclear analysis of the ITER full-tungsten divertor*, Fusion Engineering and Design **88**, 2006 (2013).

[13] M. Gilbert et al., *Neutron-induced dpa, transmutations, gas production, and helium embrittlement of fusion materials*, Journal of Nuclear Materials **442**, S755 (2013).

[14] A. Manhard, M. Balden and S. Elgeti, *Quantitative Microstructure and Defect Density Analysis of Polycrystalline Tungsten Reference Samples after Different Heat Treatments*, Practical Metallography **52**, 437 (2015).

[15] A. Dubinko et al., *Sub-surface microstructure of single and polycrystalline tungsten after high flux plasma exposure studied by TEM*, Applied Surface Science **393**, 330 (2017).

[16] A. Manhard et al., *Microstructure and defect analysis in the vicinity of blisters in polycrystalline tungsten*, Nuclear Materials and Energy **12**, 714 (2017).

[17] M. 't Hoen et al., *Surface morphology and deuterium retention of tungsten after low- and high-flux deuterium plasma exposure*, Nuclear Fusion **54**, 083014 (2014).

[18] Y. Zayachuk et al., *Depth profiling of the modification induced by high-flux deuterium plasma in tungsten and tungsten-tantalum alloys*, Nuclear Fusion **54**, 123013 (2014).

[19] L. Buzi et al., *Influence of tungsten microstructure and ion flux on deuterium plasma-induced surface modifications and deuterium retention*, Journal of Nuclear Materials **463**, 320 (2015).

[20] B. Lipschultz et al., *An assessment of the current data affecting tritium retention and its use to project towards T retention in ITER*, Tech. Rep. PSFC/RR-10-4 (Massachusetts Institute of Technology, Cambridge, Massachusetts, USA, 2010).

[21] R. Doerner et al., *Retention in tungsten resulting from extremely high fluence plasma exposure*, Nuclear Materials and Energy **9**, 89 (2016).

[22] J. Lennard-Jones, *Processes of adsorption and diffusion on solid surfaces*, Transactions of the Faraday Society **28**, 333 (1932).

[23] A. Pisarev, *Hydrogen adsorption on the surface of metals*, in *Gaseous Hydrogen Embrittlement of Materials in Energy Technologies*, Vol. 1, edited by R. P. Gangloff and B. P. Somerday (Woodhead Publishing, 2012) pp. 3–26.

[24] A. Pisarev and O. Ogorodnikova, *Elementary processes near the interface between hydrogen gas and solid*, Journal of Nuclear Materials **248**, 52 (1997).

[25] M. Pick and K. Sonnenberg, *A model for atomic hydrogen-metal interactions – application to recycling, recombination and permeation*, Journal of Nuclear Materials **131**, 208 (1985).

[26] J. Davis and A. Haasz, *Reemission of deuterium atoms from Mo, Ta and W during D^+-irradiation*, Journal of Nuclear Materials **223**, 312 (1995).

[27] W. Möller and J. Roth, *Implantation, Retention and Release of Hydrogen Isotopes in Solids*, in *Physics of Plasma-Wall Interactions in Controlled Fusion*, edited by D. E. Post and R. Behrisch (Springer US, Boston, Massachusetts, 1986) pp. 439–494.

[28] Y. Fukai, *The Metal-Hydrogen System: Basic Bulk Properties*, 2nd ed. (Springer Berlin Heidelberg, 2005).

[29] H.-D. Cabstanjen, *Interstitial positions and vibrational amplitudes of hydrogen in metals investigated by fast ion channeling*, Physica Status Solidi A **59**, 11 (1980).

[30] Y.-W. You et al., *Dissolving, trapping and detrapping mechanisms of hydrogen in bcc and fcc transition metals*, AIP Advances **3**, 012118 (2013).

[31] K. Heinola and T. Ahlgren, *Diffusion of hydrogen in bcc tungsten studied with first principle calculations*, Journal of Applied Physics **107**, 113531 (2010).

[32] R. Frauenfelder, *Solution and Diffusion of Hydrogen in Tungsten*, Journal of Vacuum Science and Technology **6**, 388 (1969).

[33] G. Was, *Fundamentals of Radiation Materials Science* (Springer Berlin Heidelberg, 2007).

[34] D. Terentyev et al., *Dislocations mediate hydrogen retention in tungsten*, Nuclear Fusion **54**, 042004 (2014).

[35] U. von Toussaint and S. Gori, *Modeling hydrogen transport in large disordered systems*, Physica Scripta **T159**, 014058 (2014).

[36] S. Myers et al., *Ion-beam studies of hydrogen-metal interactions*, Journal of Nuclear Materials **165**, 9 (1989).

[37] *http://www.tf.uni-kiel.de/matwis/amat/def_en/*.

[38] W. Callister and D. Rethwisch, *Materials Science and Engineering: An Introduction*, seventh ed. (John Wiley and Sons, 2007).

[39] D. Hull and D. Bacon, *Introduction to Dislocations*, 5th ed. (Butterworth-Heinemann, Oxford, 2011).

[40] R. Piechoczek et al., *Deuterium trapping and release in Be(0001), Be(11-20) and polycrystalline beryllium*, Journal of Nuclear Materials **438**, S1072 (2013).

[41] A. McNabb and P. Foster, *A new analysis of the diffusion of hydrogen in iron and ferritic steels*, Transactions of the Metallurgical Society of AIME **227**, 618 (1963).

[42] O. Ogorodnikova, *Trapping Effect In Hydrogen Retention In Metals*, in *Hydrogen and Helium Recycling at Plasma Facing Materials*, edited by A. Hassanein (Springer Netherlands, Dordrecht, 2002) pp. 7–15.

[43] K. Heinola et al., *Hydrogen interaction with point defects in tungsten*, Physical Review B **82**, 094102 (2010).

[44] N. Fernandez, Y. Ferro and D. Kato, *Hydrogen diffusion and vacancies formation in tungsten: Density Functional Theory calculations and statistical models*, Acta Materialia **94**, 307 (2015).

[45] G.-H. Lu, H.-B. Zhou and C. S. Becquart, *A review of modelling and simulation of hydrogen behaviour in tungsten at different scales*, Nuclear Fusion **54**, 086001 (2014).

[46] K. Schmid, U. von Toussaint and T. Schwarz-Selinger, *Transport of hydrogen in metals with occupancy dependent trap energies*, Journal of Applied Physics **116**, 134901 (2014).

[47] K. Schmid et al., *Recent progress in the understanding of H transport and trapping in W*, Physica Scripta **T170**, 014037 (2017).

[48] J. Bauer, *Hydrogen Isotope Exchange in Tungsten at Low Temperatures*, Ph.D. thesis, Technische Universität München, Germany (2018).

[49] R. Causey, *Hydrogen isotope retention and recycling in fusion reactor plasma-facing components*, Journal of Nuclear Materials **300**, 91 (2002).

[50] G. R. Longhurst, *TMAP7 user manual*, Tech. Rep. INEEL/EXT-04-02352 Rev. 2 (Idaho National Engineering and Environmental Laboratory, Idaho Falls, Idaho, USA, 2008).

[51] A. Pisarev, O. Ogorodnikova and M. Titkov, *Plasma driven tritium uptake and leakage through plasma facing materials*, Fusion Engineering and Design **41**, 103 (1998).

[52] E. Hodille et al., *Simulations of atomic deuterium exposure in self-damaged tungsten*, Nuclear Fusion **57**, 056002 (2017).

[53] J. Guterl, R. D. Smirnov and S. I. Krasheninnikov, *Revisited reaction-diffusion model of thermal desorption spectroscopy experiments on hydrogen retention in material*, Journal of Applied Physics **118**, 043302 (2015).

[54] K. Schmid, V. Rieger and A. Manhard, *Comparison of hydrogen retention in W and W/Ta alloys*, Journal of Nuclear Materials **426**, 247 (2012).

[55] T. Ahlgren et al., *Simulation of irradiation induced deuterium trapping in tungsten*, Journal of Nuclear Materials **427**, 152 (2012).

[56] O. Ogorodnikova, J. Roth and M. Mayer, *Deuterium retention in tungsten in dependence of the surface conditions*, Journal of Nuclear Materials **313-316**, 469 (2003).

[57] H. Eleveld and A. van Veen, *Deuterium interaction with impurities in tungsten studied with TDS*, Journal of Nuclear Materials **191**, 433 (1992).

[58] C. H. Skinner et al., *Recent Advances on Hydrogen Retention in ITER's Plasma-Facing Materials: Beryllium, Carbon, and Tungsten*, Fusion Science and Technology **54**, 891 (2008).

[59] J. Roth and K. Schmid, *Hydrogen in tungsten as plasma-facing material*, Physica Scripta **T145**, 014031 (2011).

[60] T. Tanabe, *Review of hydrogen retention in tungsten*, Physica Scripta **T159**, 014044 (2014).

[61] L. Ryabchikov, *Mass spectrometric investigation of degasation of molybdenum, tungsten and niobium on heating them in a vacuum*, Ukrainian Journal of Physics **9**, 293 (1964).

[62] A. P. Zakharov, V. M. Sharapov and E. I. Evko, *Hydrogen permeability of polycrystalline and monocrystalline molybdenum and tungsten*, Soviet materials science : a transl. of Fiziko-khimicheskaya mekhanika materialov / Academy of Sciences of the Ukrainian SSR **9**, 149 (1975).

[63] G. Benamati, E. Serra and C. Wu, *Hydrogen and deuterium transport and inventory parameters through W and W-alloys for fusion reactor applications*, Journal of Nuclear Materials **283-287**, 1033 (2000).

[64] G. Esteban et al., *Hydrogen isotope diffusive transport parameters in pure polycrystalline tungsten*, Journal of Nuclear Materials **295**, 49 (2001).

[65] T. Otsuka, T. Hoshihira and T. Tanabe, *Visualization of hydrogen depth profile by means of tritium imaging plate technique: determination of hydrogen diffusion coefficient in pure tungsten*, Physica Scripta **T138**, 014052 (2009).

[66] R. Anderl et al., *Deuterium Transport and Trapping in Polycrystalline Tungsten*, Fusion Technology **21**, 745 (1992).

[67] Y. Gasparyan et al., *Deuterium ion-driven permeation and bulk retention in tungsten*, Journal of Nuclear Materials **417**, 540 (2011).

[68] V. Efimov, Y. Gasparyan and A. Pisarev, *Investigation of a fine structure of deuterium thermal desorption spectra from tungsten*, Journal of Surface Investigation. X-ray, Synchrotron and Neutron Techniques **7**, 472 (2013).

[69] A. Manhard, *Deuterium inventory in tungsten after plasma exposure: a microstructural survey*, Ph.D. thesis, Universität Augsburg, Germany (2011).

[70] K. Heinola and T. Ahlgren, *Hydrogen retention to impurities in tungsten: A multi-scale study*, Journal of Nuclear Materials **438**, S1001 (2013).

[71] P. W. Tamm and L. D. Schmidt, *Binding States of Hydrogen on Tungsten*, The Journal of Chemical Physics **54**, 4775 (1971).

[72] H. Eleveld, *Hydrogen and helium in selected fusion reactor materials*, Ph.D. thesis, Technische Universiteit Delft, The Netherlands (1996).

[73] A. van Veen et al., *Hydrogen exchange with voids in tungsten observed with TDS and PA*, Journal of Nuclear Materials **155-157**, 1113 (1988).

[74] P. Grigorev et al., *Interaction of hydrogen and helium with nanometric dislocation loops in tungsten assessed by atomistic calculations*, Nuclear Instruments and Methods in Physics Research Section B **393**, 164 (2017).

[75] P. Vajda, *Anisotropy of electron radiation damage in metal crystals*, Reviews of Modern Physics **49**, 481 (1977).

[76] F. Maury et al., *Frenkel pair creation and stage I recovery in W crystals irradiated near threshold*, Radiation Effects **38**, 53 (1978).

[77] D. R. Mason et al., *Elastic trapping of dislocation loops in cascades in ion-irradiated tungsten foils*, Journal of Physics: Condensed Matter **26**, 375701 (2014).

[78] *Standard Practice for Neutron Radiation Damage Simulation by Charged-Particle Irradiation*, Tech. Rep. ASTM E521-96(2009)e2 (ASTM International, West Conshohocken, Pennsylvania, USA, 2009).

[79] K. Nordlund et al., *Improving atomic displacement and replacement calculations with physically realistic damage models*, Nature Communications **9**, 1084 (2018).

[80] K. Nordlund et al., *Primary Radiation Damage in Materials*, Tech. Rep. NEA/NSC/DOC(2015)9 (OECD, 2015).

[81] M. Norgett, M. Robinson and I. Torrens, *A proposed method of calculating displacement dose rates*, Nuclear Engineering and Design **33**, 50 (1975).

[82] C. Abromeit, *Aspects of simulation of neutron damage by ion irradiation*, Journal of Nuclear Materials **216**, 78 (1994).

[83] S. Zinkle, *Radiation-Induced Effects on Microstructure*, in *Comprehensive Nuclear Materials*, edited by R. J. Konings (Elsevier, Oxford, 2012) pp. 65–98.

[84] H. Ullmaier, ed., *Landolt-Börnstein – Group III Condensed Matter. Volume 25: "Atomic Defects in Metals"* (Springer-Verlag Berlin Heidelberg, 1991).

[85] F. Ferroni et al., *High temperature annealing of ion irradiated tungsten*, Acta Materialia **90**, 380 (2015).

[86] R. Sakamoto, T. Muroga and N. Yoshida, *Microstructural evolution induced by low energy hydrogen ion irradiation in tungsten*, Journal of Nuclear Materials **220-222**, 819 (1995).

[87] H. Eleveld and A. van Veen, *Void growth and thermal desorption of deuterium from voids in tungsten*, Journal of Nuclear Materials **212-215**, 1421 (1994).

[88] A. Debelle, M. Barthe and T. Sauvage, *First temperature stage evolution of irradiation-induced defects in tungsten studied by positron annihilation spectroscopy*, Journal of Nuclear Materials **376**, 216 (2008).

[89] J. de Vries, *Positron lifetime technique with applications in materials science*, Ph.D. thesis, Technische Universiteit Delft, The Netherlands (1987).

[90] M. Balden, A. Manhard and S. Elgeti, *Deuterium retention and morphological modifications of the surface in five grades of tungsten after deuterium plasma exposure*, Journal of Nuclear Materials **452**, 248 (2014).

[91] L. Gao et al., *Suppression of hydrogen-induced blistering of tungsten by pre-irradiation at low temperature*, Nuclear Fusion **54**, 122003 (2014).

[92] Y. Zayachuk et al., *Combined effects of crystallography, heat treatment and surface polishing on blistering in tungsten exposed to high-flux deuterium plasma*, Nuclear Fusion **56**, 086007 (2016).

[93] A. Manhard, M. Balden and U. von Toussaint, *Blister formation on rough and technical tungsten surfaces exposed to deuterium plasma*, Nuclear Fusion **57**, 126012 (2017).

[94] L. Gao et al., *Deuterium supersaturation in low-energy plasma-loaded tungsten surfaces*, Nuclear Fusion **57**, 016026 (2017).

[95] J. Bauer et al., *Influence of near-surface blisters on deuterium transport in tungsten*, Nuclear Fusion **57**, 086015 (2017).

[96] O. Ogorodnikova and V. Gann, *Simulation of neutron-induced damage in tungsten by irradiation with energetic self-ions*, Journal of Nuclear Materials **460**, 60 (2015).

[97] T. Schwarz-Selinger, *Deuterium retention in MeV self-implanted tungsten: Influence of damaging dose rate*, Nuclear Materials and Energy **12**, 683 (2017).

[98] O. Ogorodnikova, *Fundamental aspects of deuterium retention in tungsten at high flux plasma exposure*, Journal of Applied Physics **118**, 074902 (2015).

[99] S. Markelj et al., *Deuterium retention in tungsten simultaneously damaged by high energy W ions and loaded by D atoms*, Nuclear Materials and Energy **12**, 169 (2017).

[100] A. Manhard, T. Schwarz-Selinger and W. Jacob, *Quantification of the deuterium ion fluxes from a plasma source*, Plasma Sources Science and Technology **20**, 015010 (2011).

[101] G. J. van Rooij et al., *Extreme hydrogen plasma densities achieved in a linear plasma generator*, Applied Physics Letters **90**, 121501 (2007).

[102] Z. Ahmad and W. J. Goedheer, *Optimization and characterization of a Pilot-PSI cascaded arc with non-LTE numerical simulation of Ar, H_2 gases*, Plasma Sources Science and Technology **18**, 015008 (2009).

[103] H. J. van der Meiden et al., *High sensitivity imaging Thomson scattering for low temperature plasma*, Review of Scientific Instruments **79**, 013505 (2008).

[104] P. Stangeby, *The Plasma Boundary of Magnetic Fusion Devices* (IOP Publishing Ltd., Bristol and Philadelphia, 2000).

[105] A. Rusinov et al., *A setup for thermodesorption measurements*, Instruments and Experimental Techniques **52**, 871 (2009).

[106] M. Nastasi, J. Mayer and Y. Wang, *Ion Beam Analysis: Fundamentals and Applications* (CRC Press, 2014).

[107] G. Wright, D. Whyte and B. Lipschultz, *Measurement of hydrogenic retention and release in molybdenum with the DIONISOS experiment*, Journal of Nuclear Materials **390-391**, 544 (2009).

[108] M. Mayer et al., *Quantitative depth profiling of deuterium up to very large depths*, Nuclear Instruments and Methods in Physics Research Section B **267**, 506 (2009).

[109] B. Wielunska, M. Mayer and T. Schwarz-Selinger, *Optimization of the depth resolution for deuterium depth profiling up to large depths*, Nuclear Instruments and Methods in Physics Research Section B **387**, 103 (2016).

[110] B. Wielunska et al., *Cross section data for the $D(^3He,p)^4He$ nuclear reaction from 0.25 to 6 MeV*, Nuclear Instruments and Methods in Physics Research Section B **371**, 41 (2016).

[111] R. Langley, S. Picraux and F. Vook, *Depth distribution profiling of deuterium and ^3He*, Journal of Nuclear Materials **53**, 257 (1974).

[112] K. Schmid and U. von Toussaint, *Statistically sound evaluation of trace element depth profiles by ion beam analysis*, Nuclear Instruments and Methods in Physics Research Section B **281**, 64 (2012).

[113] M. Mayer, *SIMNRA User's Guide*, Tech. Rep. IPP 9/113 (Max-Planck-Institut für Plasmaphysik, Garching, Germany, 1997).

[114] M. Mayer, *RESOLNRA: A new program for optimizing the achievable depth resolution of ion beam analysis methods*, Nuclear Instruments and Methods in Physics Research Section B **266**, 1852 (2008).

[115] A. van Gorkum and E. Kornelsen, *Quantitative thermal desorption spectrometry of ionically implanted inert gases. I. Fundamental aspects*, Vacuum **31**, 89 (1981).

[116] E. Kornelsen and A. van Gorkum, *Quantitative thermal desorption spectrometry of ionically implanted inert gases. II. Technical requirements*, Vacuum **31**, 99 (1981).

[117] P. Wang et al., *Comparing deuterium retention in tungsten films measured by temperature programmed desorption and nuclear reaction analysis*, Nuclear Instruments and Methods in Physics Research Section B **300**, 54 (2013).

[118] R. Bisson et al., *Dynamic fuel retention in tokamak wall materials: An in situ laboratory study of deuterium release from polycrystalline tungsten at room temperature*, Journal of Nuclear Materials **467**, 432 (2015).

[119] A. Pisarev et al., *Formation of HD molecules during desorption of deuterium from solids*, Journal of Nuclear Materials **258-263**, 1138 (1998).

[120] K. Moshkunov et al., *Air exposure and sample storage time influence on hydrogen release from tungsten*, Journal of Nuclear Materials **404**, 174 (2010).

[121] E. Salançon et al., *Redeposition of amorphous hydrogenated carbon films during thermal decomposition*, Journal of Nuclear Materials **376**, 160 (2008).

[122] *Relative Sensitivity Measurements of Gases, Gas Analysis Application Note 282, Hiden Analytical Ltd.*

[123] P. J. Schultz and K. G. Lynn, *Interaction of positron beams with surfaces, thin films, and interfaces*, Reviews of Modern Physics **60**, 701 (1988).

[124] M. J. Puska and R. M. Nieminen, *Theory of positrons in solids and on solid surfaces*, Reviews of Modern Physics **66**, 841 (1994).

[125] J. Čížek, *Characterization of lattice defects in metallic materials by positron annihilation spectroscopy: A review*, Journal of Materials Science and Technology **34**, 577 (2018).

[126] T. Troev et al., *Positron simulations of defects in tungsten containing hydrogen and helium*, Nuclear Instruments and Methods in Physics Research Section B **267**, 535 (2009).

[127] G. Kögel, *Positron diffusion in solids and the reconstruction of inhomogeneous defect distributions from lifetime measurements*, Applied Physics A **63**, 227 (1996).

[128] P. Sperr et al., *Status of the pulsed low energy positron beam system (PLEPS) at the Munich Research Reactor FRM-II*, Applied Surface Science **255**, 35 (2008).

[129] W. Egger, *Pulsed low energy positron beams in materials sciences*, in *Physics with many positrons: Proceedings of the International School of Physics "Enrico Fermi" Course CLXXIV*, edited by R. Brusa, A. Dupasquier and A. Mills (IOS Press, Amsterdam, 2010) p. 419.

[130] C. Hugenschmidt et al., *The NEPOMUC upgrade and advanced positron beam experiments*, New Journal of Physics **14**, 055027 (2012).

[131] P. Kirkegaard, J. Olsen and M. Eldrup, *PALSfit3: A software package for analysing positron lifetime spectra*, Tech. Rep. (Technical University of Denmark (DTU), 2017).

[132] A. Manhard, G. Matern and M. Balden, *A Step-By-Step Analysis of the Polishing Process for Tungsten Specimens*, Practical Metallography **50**, 5 (2013).

[133] T. Matsui, S. Muto and T. Tanabe, *TEM study on deuterium-irradiation-induced defects in tungsten and molybdenum*, Journal of Nuclear Materials **283-287**, 1139 (2000).

[134] J. F. Ziegler, J. P. Biersack and M. D. Ziegler, *SRIM - The Stopping and Range of Ions in Matter, www.srim.org* (SRIM co., Chester, Maryland, USA, 2008).

[135] S. Ryabtsev et al., *Deuterium thermal desorption from vacancy clusters in tungsten*, Nuclear Instruments and Methods in Physics Research Section B **382**, 101 (2016).

[136] M. Zibrov et al., *On the possibility of determination of the hydrogen binding energies with defects from thermal desorption measurements with different heating rates*, Problems of Atomic Science and Technology, ser. Thermonuclear Fusion (in Russian) **38**, 32 (2015).

[137] V. Glebovsky, V. Semenov and V. Lomeyko, *Influence of the crystallization conditions on the structural perfection of molybdenum and tungsten single crystals*, Journal of Crystal Growth **87**, 142 (1988).

[138] V. Glebovsky, *Crystal Growth: Substructure and Recrystallization*, in *Recrystallization*, edited by K. Sztwiertnia (InTech, 2012) p. 59.

[139] S. Yih and C. Wang, *Tungsten: sources, metallurgy, properties, and applications* (Plenum Press, New York, 1979).

[140] A. A. Istratov and O. F. Vyvenko, *Exponential analysis in physical phenomena*, Review of Scientific Instruments **70**, 1233 (1999).

[141] R. Steindl et al., *Positron Lifetimes on Clean Metallic Surfaces*, Materials Science Forum **105**, 1455 (1992).

[142] T. E. M. Staab et al., *The influence of microstructure on the sintering process in crystalline metal powders investigated by positron lifetime spectroscopy: II. Tungsten powders with different powder-particle sizes*, Journal of Physics: Condensed Matter **11**, 1787 (1999).

[143] R. Ziegler and H. E. Schaefer, *Vacancy Formation in Molybdenum and Tungsten Investigated by Positron Lifetime Measurements*, Materials Science Forum **15**, 145 (1987).

[144] P. Staikov and N. Djourelov, *Simulations of* $\langle 100 \rangle$ *edge and* $1/2\langle 111 \rangle$ *screw dislocations in* α*-iron and tungsten and positron lifetime calculations*, Physica B: Condensed Matter **413**, 59 (2013).

[145] M. Hasegawa et al., *Effect of interstitial impurities on positronium formed in voids of vanadium*, Hyperfine Interactions **84**, 389 (1994).

[146] X. Hu et al., *Defect evolution in single crystalline tungsten following low temperature and low dose neutron irradiation*, Journal of Nuclear Materials **470**, 278 (2016).

[147] W. Setyawan et al., *Displacement cascades and defects annealing in tungsten, Part I: Defect database from molecular dynamics simulations*, Journal of Nuclear Materials **462**, 329 (2015).

[148] E. Marenkov et al., *Deuterium release from pores in tungsten created by 10 keV beam*, Nuclear Instruments and Methods in Physics Research Section B **269**, 876 (2011).

[149] A. van Veen, *Thermal Helium Desorption Spectrometry (THDS) as a Tool for the Study of Vacancies and Self-Interstitials*, Materials Science Forum **15**, 3 (1987).

[150] T. Ahlgren et al., *Bond-order potential for point and extended defect simulations in tungsten*, Journal of Applied Physics **107**, 033516 (2010).

[151] C. Becquart et al., *Microstructural evolution of irradiated tungsten: Ab initio parameterisation of an OKMC model*, Journal of Nuclear Materials **403**, 75 (2010).

[152] M. Muzyk et al., *Phase stability, point defects, and elastic properties of W-V and W-Ta alloys*, Physical Review B **84**, 104115 (2011).

[153] G.-Y. Huang, N. Juslin and B. D. Wirth, *First-principles study of vacancy, interstitial, noble gas atom interstitial and vacancy clusters in bcc-W*, Computational Materials Science **123**, 121 (2016).

[154] K. Heinola, F. Djurabekova and T. Ahlgren, *On the stability and mobility of di-vacancies in tungsten*, Nuclear Fusion **58**, 026004 (2018).

[155] K.-D. Rasch, R. W. Siegel and H. Schultz, *Quenching and recovery investigations of vacancies in tungsten*, Philosophical Magazine A **41**, 91 (1980).

[156] J. Evans, *Mechanisms of void coarsening in helium implanted silicon*, Nuclear Instruments and Methods in Physics Research Section B **196**, 125 (2002).

[157] M. Hasanuzzaman, Y. M. Haddara and A. P. Knights, *A mathematical model for void evolution in silicon by helium implantation and subsequent annealing process*, Journal of Applied Physics **112**, 064302 (2012).

[158] D. R. Mason, D. Nguyen-Manh and C. S. Becquart, *An empirical potential for simulating vacancy clusters in tungsten*, Journal of Physics: Condensed Matter **29**, 505501 (2017).

[159] M. I. Zakharova, V. A. Solov'ev and V. N. Bykov, *High-temperature stages of the annealing of radiation defects in refractory BCC metals*, Soviet Atomic Energy **38**, 101 (1975).

[160] A. Dubinko, *Plastic Deformation of Tungsten under Fusion-Plasma Exposure Conditions*, Ph.D. thesis, Ghent University (Belgium) and Complutense University of Madrid (Spain) (2018).

[161] R. K. Ham, *The determination of dislocation densities in thin films*, Philosophical Magazine **6**, 1183 (1961).

[162] J. Grzonka et al., *Electron microscopy observations of radiation damage in irradiated and annealed tungsten*, Nuclear Instruments and Methods in Physics Research Section B **340**, 27 (2014).

[163] D. Terentyev et al., *Dislocation-mediated strain hardening in tungsten: Thermo-mechanical plasticity theory and experimental validation*, Journal of the Mechanics and Physics of Solids **85**, 1 (2015).

[164] J. Čížek et al., *Vacancy clusters in ultra fine grained metals prepared by severe plastic deformation*, Journal of Physics: Conference Series **443**, 012008 (2013).

[165] T. Wider et al., *Sensitivity of positron annihilation to plastic deformation*, Physical Review B **57**, 5126 (1998).

[166] J. del Río, C. Gómez and M. Ruano, *Positron trapping mechanism in plastically deformed magnesium*, Philosophical Magazine **92**, 535 (2012).

[167] R. Stoller et al., *On the use of SRIM for computing radiation damage exposure*, Nuclear Instruments and Methods in Physics Research Section B **310**, 75 (2013).

[168] O. Oen, *Cross sections for atomic displacements in solids by fast electrons*, Tech. Rep. ORNL 4897 (Oak Ridge National Laboratory, Oak Ridge, Tennessee, USA, 1973).

[169] L. Messina, *Monte Carlo simulation for the prediction of gamma-induced damage in metals*, Master's thesis, Politecnico di Torino / Kungliga Tekniska Högskolan (2010).

[170] Y. Gasparyan et al., *Thermal desorption from self-damaged tungsten exposed to deuterium atoms*, Journal of Nuclear Materials **463**, 1013 (2015).

[171] A. Založnik et al., *The influence of the annealing temperature on deuterium retention in self-damaged tungsten*, Physica Scripta **T167**, 014031 (2016).

[172] P. Gumbsch, *Brittle fracture and the brittle-to-ductile transition of tungsten*, Journal of Nuclear Materials **323**, 304 (2003).

[173] F. Borgognoni et al., *X-ray sterilization of insects and microorganisms for cultural heritage applications*, Nuclear Instruments and Methods in Physics Research Section B **406**, 309 (2017).

List of publications

Publications on this topic:

1. **M.S. Zibrov**, A.S. Shubina, Yu.M. Gasparyan, A.A. Pisarev, *On the possibility of determination of the hydrogen binding energies with defects from thermal desorption measurements with different heating rates*, Problems of Atomic Science and Technology, series Thermonuclear Fusion (Voprosy Atomnoy Nauki i Tekhniki, seriya Termoyadernyi Sintez) **38(1)**, 32 (2015). (in Russian)

2. **M. Zibrov**, Yu. Gasparyan, S. Ryabtsev, A. Pisarev, *Isolation of peaks in TDS spectra of deuterium from ion irradiated tungsten*, Physics Procedia **71**, 83 (2015).

3. O.V. Ogorodnikova, V.V. Gann, **M.S. Zibrov**, Yu.M. Gasparyan, *Comparison of deuterium retention in tungsten pre-damaged with energetic electrons, self-ions and neutrons*, Physics Procedia **71**, 41 (2015).

4. J. Guterl, R.D. Smirnov, S.I. Krasheninnikov, **M. Zibrov**, A.A. Pisarev, *Theoretical analysis of deuterium retention in tungsten plasma-facing components induced by various traps via thermal desorption spectroscopy*, Nuclear Fusion **55**, 093017 (2015).

5. **M. Zibrov**, S. Ryabtsev, Yu. Gasparyan, A. Pisarev, *Experimental determination of the deuterium binding energy with vacancies in tungsten*, Journal of Nuclear Materials **477**, 292 (2016).

6. S. Ryabtsev, Yu. Gasparyan, **M. Zibrov**, A. Shubina, A. Pisarev, *Deuterium thermal desorption from vacancy clusters in tungsten*, Nuclear Instruments and Methods in Physics Research B **382**, 101 (2016).

7. S.A. Ryabtsev, Yu.M. Gasparyan, **M.S. Zibrov**, A.A. Pisarev, *On the annealing of radiation-induced point defects in tungsten*, Journal of Surface Investigation. X-ray, Synchrotron and Neutron Techniques **10(3)**, 658 (2016).

8. **M. Zibrov**, M. Balden, T.W. Morgan, M. Mayer, *Deuterium trapping and surface modification of polycrystalline tungsten exposed to a high-flux plasma at high fluences*, Nuclear Fusion **57**, 046004 (2017).

9. A. Dubinko, D. Terentyev, A. Bakaeva, T. Pardoen, **M. Zibrov**, T.W. Morgan, *Effect of high flux plasma exposure on the micro-structural and -mechanical properties of ITER specification tungsten*, Nuclear Instruments and Methods in Physics Research B **393**, 155 (2017).

Publications on other topics:

1. S. Krat, Yu. Gasparyan, V. Efimov, A. Mednikov, **M. Zibrov**, A. Pisarev, *Deuterium retention in mixed C-W-D films co-deposited in magnetron discharge in deuterium*, Journal of Nuclear Materials **438**, 204 (2013).

2. **M.S. Zibrov**, A.A. Pisarev, G.V. Khodachenko, D.V. Mozgrin, *Development of thin protective carbon-based coatings on aluminum*, Advances in Applied Physics (Uspekhi Prikladnoi Fiziki) **1(2)**, 167 (2013). (in Russian)

3. **M.S. Zibrov**, G.V. Khodachenko, A.V. Tumarkin, A.V. Kaziev, T.V. Stepanova, A.A. Pisarev, M.V. Atamanov, *Development of protective metal coatings on aluminum by magnetron sputtering*, Journal of Surface Investigation. X-ray, Synchrotron and Neutron Techniques **7(6)**, 1156 (2013).

4. **M. Zibrov**, M. Mayer, E. Markina, K. Sugiyama, M. Betzenbichler, H. Kurishita, Yu. Gasparyan, O.V. Ogorodnikova, A. Manhard, A. Pisarev, *Deuterium retention in TiC and TaC doped tungsten under low-energy ion irradiation*, Physica Scripta **T159**, 014050 (2014).

5. **M. Zibrov**, M. Mayer, L. Gao, S. Elgeti, H. Kurishita, Yu. Gasparyan, A. Pisarev, *Deuterium retention in TiC and TaC doped tungsten at high temperatures*, Journal of Nuclear Materials **463**, 1045 (2015).

6. E. Meshcheryakova, **M. Zibrov**, A. Kaziev, G. Khodachenko, A. Pisarev, *Langmuir probe diagnostics of low-pressure inductively coupled argon plasmas in a magnetic field*, Physics Procedia **71**, 121 (2015).

7. E.A. Meshcheryakova, A.V. Kaziev, **M.S. Zibrov**, T.V. Stepanova, M.M. Berdnikova, M.M. Kharkov, A.A. Pisarev, *Investigation of parameters of inductively coupled plasma and its use in steel nitriding*, Bulletin of the Russian Academy of Sciences: Physics **80(2)**, 175 (2016).

8. A. Tumarkin, **M. Zibrov**, G. Khodachenko, D. Tumarkina, *High-rate deposition of silicon films in a magnetron discharge with liquid target*, Journal of Physics: Conference Series **768**, 012015 (2016).

9. **M. Zibrov**, K. Bystrov, M. Mayer, T.W. Morgan, H. Kurishita, *The high-flux effect on deuterium retention in TiC and TaC doped tungsten at high temperatures*, Journal of Nuclear Materials **494**, 211 (2017).

10. M. Balden, S. Elgeti, **M. Zibrov**, K. Bystrov, T.W. Morgan, *Effect of the surface temperature on surface morphology, deuterium retention and erosion of EUROFER steel exposed to low-energy, high-flux deuterium plasma*, Nuclear Materials and Energy **12**, 289 (2017).

11. V.Kh. Alimov, Y. Hatano, K. Sugiyama, **M. Zibrov**, T. Schwarz-Selinger, W. Jacob, *Deuterium absorption in reduced activation ferritic/martensitic steel F82H under exposure to* D_2O *vapor/water at room temperature*, Journal of Nuclear Materials **507**, 54 (2018).

Acknowledgements

The work presented in this thesis would not have been possible without the help and support of many people. I would like to express my gratitude to all of them.

First of all, I would like to thank my promoters Prof. Jean-Marie Noterdaeme from Ghent University and Prof. Ulrich Stroth from Technical University of Munich for giving me the opportunity to carry out this joint PhD project. Despite a busy schedule, they regularly found time to monitor the progress of my work and helped me to look at my research from various perspectives.

A large part of this work was performed at Max Planck Institute for Plasma Physics and I would like to express my appreciation to all members of the E2M division. First and foremost, I want to thank my supervisor Matej Mayer for helping me to resolve many practical and theoretical issues and for encouraging me in difficult times. Thank you also for helping me to express my ideas clearly and to sharpen my arguments in the papers and in the thesis. Many thanks to the leader of the Plasma-Material Interaction group Wolfgang Jacob for organizing a very effective working process in the group, for the careful reading of this thesis and for giving me helpful feedback. I am grateful to Martin Balden, Stefan Elgeti, Katja Hunger, and Gabriele Matern for performing SEM investigations of my samples and for helping me to interpret the results. Thanks to Armin Manhard and Thomas Schwarz-Selinger for showing me how to operate PlaQ and for sharing their expertise in many fields. I acknowledge Thomas Dürbeck and Kazuyoshi Sugiyama for the help with operating TESS, Till Höschen for performing XPS measurements, and Joachim Dorner and Michael Fußeder for operating the accelerator. I am also grateful to Johannes Bauer, Vassily Burwitz, Liang Gao, Stefan Kapser, Elena Markina, Klaus Schmid, Karsten Schlüter, and Barbara Wielunska for helping me to perform some of the experiments, as well as for many fruitful scientific discussions. I also deeply appreciate the technical support from the staff of AUG and E2M workshops.

A part of my work was carried out at Dutch Institute for Fundamental Energy Research and I would like to thank all members of the PSI group. First of all, I am grateful to my supervisor Thomas Morgan for regular discussions of my plans and results and for valuable pieces of advice. My special thanks to

Kirill Bystrov for teaching me to operate Pilot-PSI and for helping me to carry out the experiments. I am thankful to Richard Al, Hennie van der Meiden, and Jordy Vernimmen for their help with solving many technical problems. Many thanks to Damien Aussems, Sébastien Bardin, Stein Van Eden, Karol Ješko, and Vladimir Kvon for helping me with the experiments and for many stimulating discussions.

I would also like to acknowledge my Alma Mater, Moscow Engineering Physics Institute, and especially all members of the Plasma Physics Department where I did my diploma and started doing my PhD. My special thanks to the department head Prof. Valery Kurnaev for giving me the opportunity to carry out my research at the department, for his constant support and encouragement. I am very thankful to my supervisors Prof. Alexander Pisarev, Yury Gasparyan, and Georgy Khodachenko (deceased) for sharing their vast knowledge in the fields of vacuum technology, plasma physics, plasma-material interactions, and hydrogen behaviour in metals. Their constant support enabled me to acquire many essential practical skills and a strong theoretical background. I am grateful to Vitaly Efimov, Sergey Ryabtsev, and Ivan Timofeev for showing me how to operate MEDION and for helping me to perform the measurements. It was a pleasure to work with Andrey Kaziev and Alexander Tumarkin because of their enthusiasm, chivalry, and the strong team spirit. I would also like to thank Dobrynya Kolodko, Stepan Krat, Ekaterina Mescheryakova, Alena Shubina, Dmitry Sinelnikov, and Ivan Sorokin for always finding time to help me and to share the knowledge.

I also deeply appreciate the contributions of my collaborators from other institutions. First of all, I am grateful to Werner Egger from Bundeswehr University Munich for performing the positron annihilation measurements of my samples, for the data evaluation, and for numerous discussions regarding the interpretation of the results. I express my gratitude to Anastasiia Bakaeva, Andrii Dubinko, and Dmitry Terentyev from SCK • CEN for performing tensile deformations of my tungsten samples, their TEM analysis, and for helping me to understand the properties of dislocations in tungsten. Many thanks to Marius Wirtz from Forschungszentrum Jülich for recrystallizing the tensile specimens, to Fabio Borgognoni from ENEA for damaging my samples with electrons, and to Hidde Brongersma and Vadim Glebovsky for providing me with the excellent quality tungsten single crystals. I would also like to thank Dmitry Matveev for many fruitful discussions about hydrogen behaviour in metals.

I express my appreciation to Eveline Indemans, Kathleen Van Oost, and Biggy Perey for their professional help with solving many administrative issues. Many thanks to Vassily Burwitz and Niek Den Harder for translating the abstract of this thesis into German and Dutch, respectively.

Finally, I am deeply grateful to my family and my friends for the continuous support and for encouraging me to go forward.